SCT Hybrid Testing and the Production of Direct Photons in the ATLAS Experiment at the LHC

Thomas Ivan Hollins

Thesis submitted for a degree of Doctor of Philosophy

Particle Physics Group,
School of Physics and Astronomy,
University of Birmingham.

November, 2006.

To little baby Hollins, who's impending arrival has been a constant source of inspiration.

"I do not feel obliged to believe that the same God who has endowed us with sense, reason and intellect has intended us to forgo their use."

Galileo Galilei (1564 - 1642)

Synopsis

Reported in this thesis are the results of production tests of barrel hybrids, photon identification and an analysis of Monte Carlo direct photons.

The testing of barrel hybrids assembled at Birmingham is now complete. Hybrids were mounted with chips, bonded and tested to meet the ATLAS acceptance criteria. They have had sensors subsequently attached, been placed on the semiconductor tracker barrels and are preparing to start their operational life.

Photon identification has been studied over the E_T range 20 - 450 GeV. Calorimeter identification has been optimised to an efficiency of $\approx 90\%$ for single photons, giving a rejection factor against QCD jets, increasing with E_T, from 2,600 at 20 GeV to 12,700 at > 300 GeV. The addition of an isolation cut increases this rejection by a factor 2-4 (20-300 GeV); although the high energy region suffers from a lack of statistics.

The feasibility of performing a direct photon cross section measurement has been shown. Significant numbers of events are expected over a large range of E_T, with the signal to background increasing from unity at 20 GeV, to around 30 at 300 GeV. Methods for quantifying the remaining background have been presented and show it should be possible to recover accurately the direct photon signal.

Direct photons have been shown to be sensitive to the various parameterisations of the gluon parton density function (PDF). Variations of $4\% - 10\%$ in η_γ are visible across the p_T and η ranges accessible by ATLAS. This corresponds to a sensitivity at low p_T, to the low-x behaviour of the gluon and at high p_T, to the high-x behaviour of the gluon. As a result, the measurement of η_γ can be used to help constrain the gluon PDF.

Author's Contribution

All the work presented in this thesis is my own, however, due to collaborative nature of high energy physics a great debt is owed to the many people involved with the ATLAS experiment and the LHC.

Needless to say, the construction of the ATLAS SCT was the product of many institutes and individuals hard work. My small part, carried out at Birmingham, involved testing and analysing the barrel module hybrids assembled here. Both the production test system and the analysis software were the result of other's work. I did, however, make a significant contribution to the testing program at Birmingham and to the results displayed in chapter 3. An ATLAS note summarising the tests and the barrel modules in general, is currently under preparation.

The data sets used in the work presented on photon identification, jet rejection and the gluon PDF were generated mainly by myself, but also with the help of the ATLAS Monte Carlo Team. Events that I generated, used the computer resources of institutions scattered around the world, but in all cases were defined, run and validated by myself. I wrote all the analysis code used to obtain the results of chapters 5, 6 and 7, but again, a great debt is owed to others, specifically to the developers of 'ROOT' and the 'Analysis Skeleton', without which, my work would not have been possible.

Acknowledgements

Over the past 3 years I have been the recipient of a great deal of support. I would like to take this opportunity to say thank you to all my friends, family and colleagues who have help me through this time.

Firstly, a big thank you to my wife, Zena a.k.a. auxiliary funding. Thank you for all your patience and encouragement. Those gentle words, that on the bad days persuaded me not to throw the monitor out of the window and on the good, well, just made me happy. You have made these three years, and the seven before them, an absolute pleasure. Thank you.

Thanks also to my supervisor John Wilson, I don't think I have ever been turned away from your office and you have been exceptionally generous with your time and wisdom. Thank you for sowing the seed of a PhD all those years ago with your passion and eloquence as a lecturer. Further thanks to Pete Watkins and Dave Charlton for giving me a place at Birmingham despite my time away from Physics and to the members of Birmingham's Particle Physics Group in general, who have made it such a warm and welcoming place. The people of ATLAS' standard model working group have also been generous with advice and encouragement, suggesting more interesting areas of research than I had time to study. Thank you to you all!

The itinerant occupants of 316 have made my PhD a stimulating and enjoyable experience. Thank you for always being willing to be distracted by my questions and providing countless distractions to me.

And finally, to epat48, my trusted desktop PC. You have complained incessantly at my poor coding and quite unreasonably refused to compile on more occasions than I can remember; your trauma is now at an end.

Ivan Hollins, Nov 2006.

Contents

List of Figures

List of Tables

Chapter 1

Theory

1.1 Introduction

The ancient Greeks recognised just four elements, earth, wind, fire and water. These elements formed the building blocks of matter, of all they could see and of all they could touch. This concept lay dormant for almost two thousand years, until the middle ages and the allure of alchemy brought people to the systematic study of matter. In the nineteenth century, Mendeleev categorised 63 elements before his death and this number has continued to grow to the 117 accepted today. These elements are, however, not now considered quite so elemental, although in some sense of course they remain so. Rutherford opened Pandora's box and what is now considered elemental, is smaller than the Greeks, or indeed anyone else, could have possibly imagined.

1.2 The Standard Model

The framework within which our understanding of elementary particles sits is called the Standard Model. In this model, the matter we observe in the universe is com-

posed of point-like particles having half-integer values of spin. These so called *fermions* can be further divided into *families* of leptons and quarks. There exist three *generations* of these *families*, each consisting of a lepton and quark doublet, as shown in figure 1.1. There are therefore a total of six leptons and six quarks in the Standard Model. The first lepton doublet consists of the electron and electron-neutrino, the first quark doublet the up and the down quarks. The second and third generations of leptons and quarks have similar properties but, as can be seen from table 1.1, have increasingly large mass. It is an observed fact that all the visible matter in the universe appears to be made up of such particles. However, for each of the particles discussed above a corresponding antiparticle also exists. These antiparticles possess properties opposite to those of the corresponding particle with the exception that they possess the same mass. Although these antiparticles are routinely created and manipulated in the laboratory they have not been observed in large scale formations in the universe.

$$Leptons \begin{pmatrix} e \\ \nu_e \end{pmatrix} \begin{pmatrix} \mu \\ \nu_\mu \end{pmatrix} \begin{pmatrix} \tau \\ \nu_\tau \end{pmatrix}$$

$$Quarks \begin{pmatrix} u \\ d \end{pmatrix} \begin{pmatrix} c \\ s \end{pmatrix} \begin{pmatrix} t \\ b \end{pmatrix}$$

Figure 1.1: The three generations of fermions within the Standard Model.

These fundamental particles interact with four fundamental forces: electromagnetism, the weak force, the strong force and gravity. A quantum description exists for only the first three of these forces and consequently gravity has yet to be included within the Standard Model. This absence is a strong indicator that the model is unlikely to be a complete theory and is, in all probability, a low energy approximation of some as yet unformulated or unconceived theory.

The forces described by the Standard Model are mediated by the fundamen-

Generation 1	Generation 2	Generation 3	Charge
$m_e = 0.511\ MeV$	$m_\mu = 105.66\ MeV$	$m_\tau = 1,777\ MeV$	-1
$m_{\nu_e} \leq 10eV$	$m_{\nu_\mu} \leq 0.16MeV$	$m_{\nu_\tau} \leq 18MeV$	0
$m_u \simeq 0.31\ GeV$	$m_c \simeq 1.6\ GeV$	$m_t \simeq 180\ GeV$	$+2/3$
$m_d \simeq 0.31\ GeV$	$m_s \simeq 0.5\ GeV$	$m_b \simeq 4.6\ GeV$	$-1/3$

Table 1.1: Fermion generations and their respective properties.

tal particles, shown in table 1.2. In contrast with fermions, these point-like particles have integer values of spin and are named *bosons*. Leptons interact solely with the electromagnetic and weak forces. At high energies, the masses of the W and Z become sufficiently negligible that these two forces are reunited into one common force; the electroweak force. This unification is described by electroweak theory with the masses of the force carrying *bosons* the γ, W and Z being fixed parameters in the model. It is the different masses of these particles which, at low energies, cause the separation of the electromagnetic and weak forces. This *electroweak symmetry breaking* is currently a topic of intense study, and indeed one of the primary goals of some of the most recent particle accelerators. It is believed that the process by which the W and the Z acquire their mass, but through which the photon remains massless, is through their interaction with the Higgs field. This mechanism, although included as part of the Standard Model, is at present unproven. A complete description of the Higgs mechanism is not relevant for this thesis, but nonetheless, its discovery would be a major achievement in particle physics. This brief description of the Standard Model is completed with the inclusion of the strong nuclear force and its interactions with quarks and gluons. Since this force is of particular interest here it will be explained in more detail; however, its full description is beyond the scope of this work.

Boson	Symbol	Force	Charge	Mass (GeV/c^2)
photon	γ	Electromagnetic	0	0
W^+/W^-	W^+/W^-	Weak Force	± 1	80.3
Z	Z	Weak Force	0	91.2
gluon	g	Strong Force	0	0

Table 1.2: Vector bosons and the forces they mediate.

1.3 Quantum Chromodynamics (QCD)

Quarks interact not only with the electromagnetic and weak forces, but also though the strong force, as described by Quantum Chromodynamics (QCD). An overview of the development of this theory will be presented, along with some important results as they relate to proton proton scattering.

1.3.1 The Parton Model

The Quark Parton Model (QPM), developed by Feynman and Bjorken in the late 1960s, explains features shown in deep inelastic scattering (DIS) experiments. Leptons were scattered off a nucleon and it was observed that the cross section from such events was only weakly dependent on the magnitude of the squared four-momentum transfer (Q^2). This situation was contrasted by the strong dependence on Q^2 shown by the elastic cross section. The interpretation of this dependence was that, rather than scattering coherently off a proton as a whole, the electron scatters incoherently off point-like particles inside the proton. These were generically labelled partons and were subsequently identified by Feynman [1] as the quarks and gluons familiar to us today.

The constituent quarks of a proton are described as free particles in the QPM

and, in the absence of any strong force, the model is clearly a first attempt at explaining the behaviour of quarks inside the proton. Nevertheless, the model has met with some success and can explain many of the observed features of the earlier scattering experiments. The proton is assumed to consist of a set of partons moving parallel to the direction of the proton. Each parton, subsequently identified as a quark, is ascribed a factional electric charge. From this simple description and using parallels with QED, some remarkable predictions are made. The structure of the proton can be described by two independent structure functions F_1 and F_2. These functions, initially dependent on two scalars Q^2 and x, were postulated by Bjorken to be independent of Q^2 at large Q. Here x is defined to be $x = Q^2/2P \cdot q$ where P is the four momentum of the initial proton and q is the four vector of the photon mediating the scatter. It is then identified as the fraction of the initial proton's momentum carried by the struck quark. This so called *Bjorken scaling* was first observed at the Stanford Linear Accelerator (SLAC) in 1969 and was the first direct evidence for quarks.

That quarks can be thought of as free particles, is of course a simplification. The first and most obvious evidence is that they are bound inside protons. Additionally, it was observed that only about half of the proton's momentum was accounted for by the quarks. A large faction of the proton's momentum appeared to be missing, or more precisely, was carried by something not seen in the DIS experiments. The carrier of this missing momentum was identified to be the gluon.

1.3.2 The Strong Force and Asymptotic Freedom

The strong force is mediated through the exchange of eight coloured gluons. There exist three colour charges in QCD, red, blue and green. These colour charges are analogous to the (single) electric charge in QED, with one very important exception. In QED the electromagnetic force is mediated by the photon, which itself carries no electromagnetic charge; in QCD the force is mediated by the gluon, which does pos-

sess a colour charge. The fact that the gluon can self-couple and the photon cannot gives rise to the contrasting behaviours of the two forces as a function of Q. Whilst the electromagnetic force ($\alpha(Q)$) increases with Q, the strong force ($\alpha_s(Q)$) actually decreases. This behaviour of the strong force, known as asymptotic freedom, continues until at sufficiently high Q, quarks and gluons inside a proton can be treated as effectively free particles. As will be explained in section 1.3.3, this has important consequences for QCD and in particular for its ability to provide calculable results.

A more immediate consequence, however, is that quarks and gluons are confined to exist only inside colourless objects known collectively as hadrons. To demonstrate this process, consider the creation of a quark anti-quark pair. As the pair moves apart the strong force between the two particles increases. As the force increases, so too does the potential energy stored in the colour field. This continues until such an energy-density whereby a new quark-anti-quark pair is able to be formed. The process is then repeated until only stable states with no net colour charge remain. As a result the bare quarks or gluons are said to hadronise into sets of outgoing particles, commonly referred to as jets. Each of these hadrons contains such numbers of quarks so as to possess no overall colour charge. Two such types of matter are currently known to exist; baryons and mesons. Baryons consist of three quarks, each with a different unit of colour charge, ($q_R q_B q_G$ or $\bar{q}_R \bar{q}_B \bar{q}_G$). Mesons possess a quark anti-quark pair ($q_R \bar{q_R}$ or $q_B \bar{q_B}$ or $q_G \bar{q_G}$), again having no overall net charge.

1.3.3 Hadron-Hadron Scattering

Calculations in QCD can be made using perturbation theory. This makes the assumption that the strong force is small and as a result is only valid in regions where α_s is much less than 1. That these regions exist at all is due to the asymptotic nature of the strong force, as discussed is section 1.3.2 above. Perturbative techniques generally become possible for values of $Q^2 \gtrsim 1$ GeV^2.

In any scattering experiment two incoming particles are collided together and the remnant of the collision observed. Consider the scattering of two initial hadrons into a final state particle given by

$$A(p_A) + B(p_B) \rightarrow C(p_C) + X \tag{1.1}$$

where A, B and C are the initial and final hadrons of momentum p_A, p_B and p_C and X represents all unobserved particles. The underlying scattering will be that of two partons, one from each proton. A full calculation of this involves the determination of the hadron's initial state wave function in regions where perturbation theory cannot be applied - i.e. in regions where α_s is necessarily large. Inspiration is therefore taken from the parton model where the problem can be separated into a hard scatter convoluted with a parton distribution and a fragmentation function. This is possible, within the parton model, due to the absence of any quark interactions. The fragmentation of the struck quark into hadrons takes place over a larger time scale and can essentially be treated as a separate process. Accordingly, the invariant production cross section can be written as an incoherent sum of all contributing processes,

$$E_C \frac{d\sigma^3}{d^3 p_C}(A + B \rightarrow C + X) = \sum_{abcd} \int dx_a dx_b dz_c f_A^a(x_a) f_B^b(x_b) D_c^C(z_c) \frac{\hat{s}}{z_c \pi^2} \frac{d\sigma}{d\hat{t}}(ab \rightarrow cd) \delta(\hat{s} + \hat{t} + \hat{u}) \tag{1.2}$$

Here $f_A^a(x_a)$ is the so called parton distribution and describes the probability of finding a parton a with a momentum fraction between x_a and $x_a + dx_a$ within hadron species A. A similar description applies to $f_B^b(x_b)$. In dealing with the observed final state, we describe the chance that the scattered parton c, fragments into a hadron of species C, with momentum fraction of between z and $z + dz$, by the *fragmentation function* $D_c^C(z_c)$. $\hat{s}, \hat{t}$ and $\hat{u}$ are the Mandelstam variables defined

by $\hat{s} = (p_a + p_b)^2, \hat{t} = (p_a - p_c)^2$ and $\hat{u} = (p_b - p_c)^2$, where p_a, p_b, p_c and p_d are the four momentum of the interacting partons. The delta function is appropriate for the two body scattering of massless partons and enforces energy and momentum conversation.

This simple picture, in the absence of quark interactions and at lowest order, clearly needs to be improved. Perturbative quantum chromodynamics (pQCD) introduces the strong force and the problem is again separated into a hard scatter convoluted with a parton distribution and a fragmentation function. This process, described by QCD's *factorisation theorem* [2], is schematically shown in figure 1.2. The generic scatter of two protons is shown at its lowest order, with the struck partons directly interacting before fragmenting into some final state.

There are many possible modifications to this simple picture, where either the initial or final state partons radiate particles, or where the partons themselves form virtual loops. However, the inclusion of certain types of these higher order diagrams leads to mass singularities within the calculation. One such example is the emission of a soft gluon from an initial state quark. If the gluon is emitted collinearly with the quark, then the internal quark line will be "on-shell" i.e. the invariant mass corresponding to the internal quark line will become zero [3]. Such configurations attract corrections proportional to $ln(s/m^2_{quark})$, however, since quarks are massless in this theory, the logarithm becomes infinite. These singularities appear in all subprocesses involving a given species of partons. In this sense they can be considered universal and as a result can be included, or *factorised*, into the parton distributions. The scale at which these soft gluon effects are absorbed into the parton distribution is known as the factorisation scale, (μ_F). Processes above this scale are considered part of the hard scatter and so need to be calculated perturbatively. These singularities are thus removed from the calculation and included in the parton distributions. However, the result of this is that the parton distributions themselves now become dependent upon the factorisation scale. Similar considerations are made for the *fragmentation function* ($D^C_c(z_c)$) and as a result this too becomes dependent upon a fragmentation

scale, (M). What the factorisation theorem has effectively done is to separate the problem into a perturbative hard scatter and two non-perturbative parts, the parton distributions and the fragmentation functions. The non-perturbative parts are currently incalculable and so must be obtained from experiment.

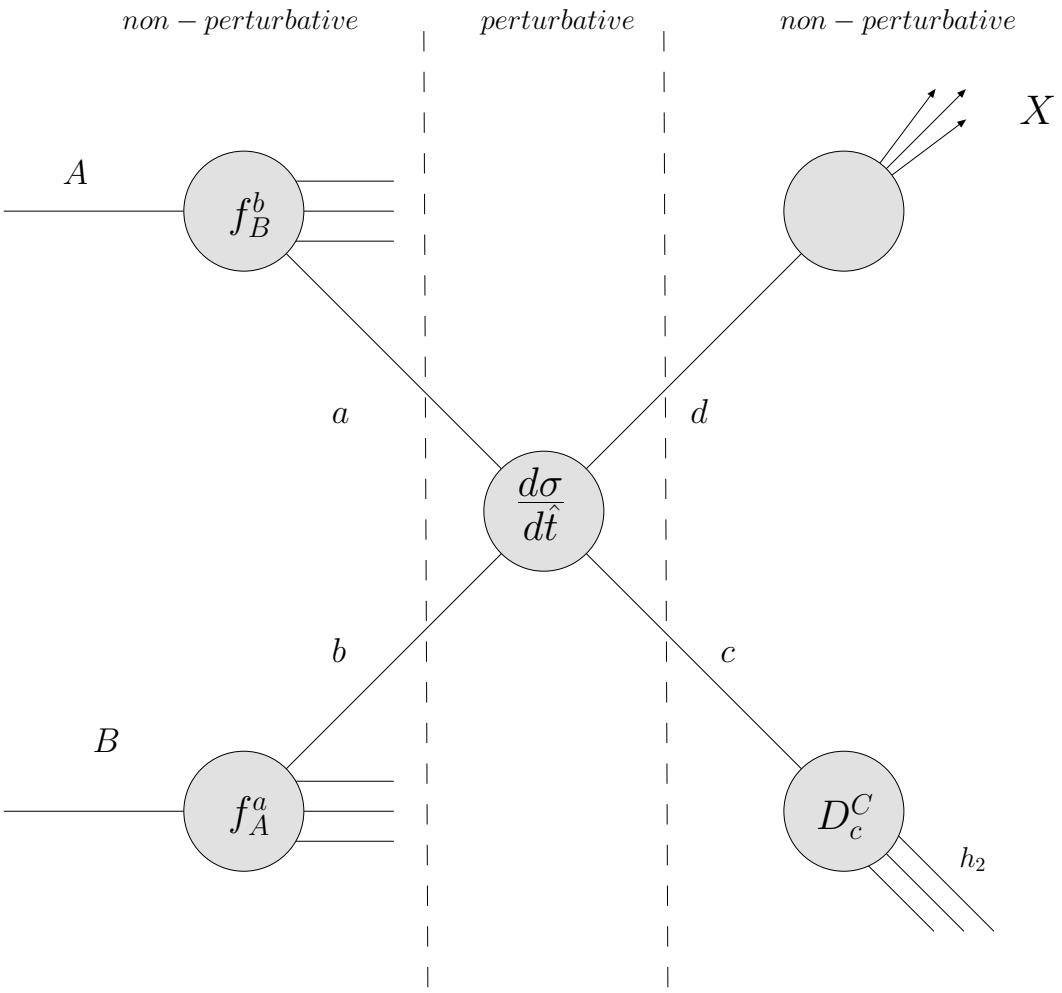

Figure 1.2: Factorisation of a high p_T reaction into parton distribution functions (f_A^a and f_B^b), parton fragmentation function (D_c^C) and a hard scattering subprocess $\frac{d\sigma}{dt}$.

The perturbative hard scatter has so far been considered only at the leading order. Whereas higher order effects below the fragmentation scale and those causing mass singularities were included in the parton distribution, those above this scale

must be calculated. Again, consider the case where a gluon is emitted from one of the initial or final state legs, this time though at a large angle. Such processes involve an additional strong interaction and hence another factor of α_s. For a full calculation, all such higher order terms must be included, all quark/gluon species summed over and an integral taken over all the possible parton momenta. Unfortunately, due to the complexity of these calculations, it is not possible to perform these to all orders. As a result, only a finite number of orders are calculated, typically one, two or three and the calculation is artificially truncated. Infinities that were present in the integration of parton momenta, specifically those present in quark and gluon loops, no longer cancel. The calculated process now yields unphysical results and must be regulated through a process called *renormalisation*. The effect of this is to introduce yet another artificial scale μ_R into which these infinities are removed. This results in a calculation yielding finite results, but which has a residual dependency upon the renormalisation scale used.

In a full calculation of the process (1.1) we now have three different scales to choose. Since these scales have different origins, there is no real reason why they should be chosen to be equal to one another. However, in practise, to avoid introducing an unphysical hierarchy into the problem, these scales are often chosen to be the same and are commonly set to the P_T of one of the final state particles.

Combining these aspects, the modified form of equation 1.2 is now

$$E_C \frac{d\sigma^3}{d^3p_C}(AB \to C + X) = \sum_{abcd} \int dx_a dx_b dz_c f_A^a(x_a, \mu_F) f_B^b(x_b, \mu_F) D_c^C(z_c, M) \frac{\hat{s}}{z_c^2 \pi} \frac{d\sigma(\mu_R, \mu_F)}{d\hat{t}}(ab \to cd)\delta(\hat{s}+\hat{t}+\hat{u}) \tag{1.3}$$

As described above it is a feature of the strong force that the coupling constant α_s evolves with Q^2. This evolution is described by:

$$\frac{d\alpha_s(t)}{dt} = \beta(\alpha_s(t)) \tag{1.4}$$

where $t = ln(Q^2/\mu^2)$ [3] and β is a function of $\alpha_s(t)$. β must be calculated in pQCD with the result to two loop order given by [4]:

$$\beta(\alpha_s) = -b_0\alpha_s^2(Q^2) - b_1\alpha_s^3(Q^2) \tag{1.5}$$

where

$$b_0 = \frac{33 - 2f}{12\pi} \text{ and } b_1 = \frac{153 - 19f}{24\pi^2} \tag{1.6}$$

and f is the number of active quark flavours. If only the leading order result is considered ($b_1 = 0$) and equation 1.4 integrated then,

$$\alpha_s(Q^2) = \frac{1}{b_0 ln(Q^2/\Lambda^2_{QCD})} \tag{1.7}$$

where Λ^2_{QCD} sets the scale for renormalisation and is experimentally found to be approximately 200 MeV. It can be seen from equation 1.7, that by considering large values of Q^2, the size of α_s decreases to such a point where perturbative techniques can be used.

1.3.4 The DGLAP Evolution Equations

As we have seen, parton distributions are non perturbative in nature and cannot currently be calculated. They must instead be determined empirically from experiment and then evolved up to a desired Q^2. The parton model, in the form of Bjorken scaling, states that these functions should be dependent only upon x for

large values of Q^2; that is they should independent of Q^2. Gluon interactions, included within pQCD, modify this picture and introduce a $log(Q)$ dependency to the parton distributions. This evolution is described by the Dokshitzer-Gribov-Lipatov-Altarelli-Parisi (DGLAP) [5] equations

$$\frac{dq(x,Q^2)}{dlogQ^2} = \frac{\alpha_s(Q^2)}{2\pi}\int_x^1 \frac{dy}{y}\left[q(y,Q^2)P_{qq}\left(\frac{x}{y}\right) + g(y,Q^2)P_{qg}\left(\frac{x}{y}\right)\right] \tag{1.8}$$

$$\frac{dg(x,Q^2)}{dlogQ^2} = \frac{\alpha_s(Q^2)}{2\pi}\int_x^1 \frac{dy}{y}\left[q(y,Q^2)P_{gq}\left(\frac{x}{y}\right) + g(y,Q^2)P_{gg}\left(\frac{x}{y}\right)\right] \tag{1.9}$$

The splitting functions $P_{ab}(x/y)$ are interpreted as the probability of parton a with momentum y producing a parton b with momentum x. There are four different splitting functions arising from the two species of partons, quarks and gluons, as shown in figure 1.3.

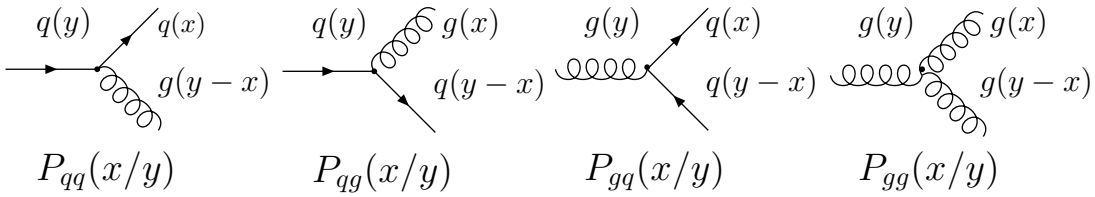

Figure 1.3: Feynman diagrams for the four splitting functions of the DGLAP equation.

These DGLAP equations allow data at different values of Q^2 to be used to extract the parton distributions. The basic procedure is to parametrise the parton distributions, $f_i(x,Q^2)$, with a polynomial at some initial scale Q_0^2, typically chosen to be ≈ 1 (GeV)^2. Using the DGLAP equations, this is then evolved up to the relevant Q^2 and an NLO QCD fit done for data with $Q > Q_1$ and where, $Q_1 > Q_0$. Since parton distributions are universal, data from different experimental processes may be used in this fit. All that is required is that the processes of interest are

accurately described by the relevant NLO calculations. Typical parton distribution fits use data from many different experiments over a range of Q^2. Such a parton distribution set, CTEQ 6M [6], is shown in figure 1.4. The experiments used to extract $f_i(x, Q^2)$ are listed in table 1.3 and span data taken over a period of over ten years. At the value of $Q^2 = 10^4$ GeV shown in figure 1.4, the gluon distribution is dominant at values of $x \lesssim 10^{-1}$. At larger values of x, contributions from the valence quarks in the proton (uud) form the majority of struck partons; as x reduces contributions from sea quarks increase and at low x are the most likely source of quarks in the proton.

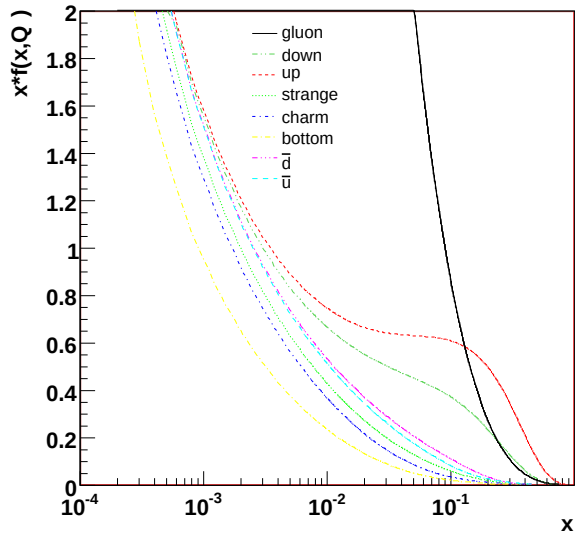

Figure 1.4: Quark and gluon distributions, as obtained through a NLO fit by the CTEQ group.

1.4 Conclusion

A brief outline of the standard model has been presented. This theory has for many years been highly successfully in describing fundamental particles and their interactions. Many calculations involved in modern particle physics can now be fully calculated, however, for certain classes and types of interactions perturbative techniques must be used. These approximations introduce a number of unphysical

Process	Experiment	Q^2 range	ref
DIS	BCDMS	$7 \leq Q^2 \leq 260$	[7, 8]
	H1a	$150 \leq Q^2 \leq 30,000$	[9]
	H1b	$1.5 \leq Q^2 \leq 150$	[10]
	ZEUS	$2.7 \leq Q^2 \leq 30,000$	[11]
	NMC	$0.1 \leq Q^2 \leq 145$	[12]
	CCFR	$1 \leq Q^2 \leq 50$	[13]
Drell-Yan	E605	$49 \leq Q^2 \leq 289$	[14]
	E866	$4 \leq Q^2 \leq 166$	[15]
Inclusive Jets	CDF	$1,600 \leq Q^2 \leq 220,000$	[16]
	D0	$2,500 \leq Q^2 \leq 230,000$	[17, 18]
W asymmetry	CDF	$Q^2 \approx M_W^2 \approx 6,400$	[19]

Table 1.3: A list of experiments and processes used in the global parton distribution fit of CTEQ 6M.

dependencies into the calculations and must be used with care if experimental data are to be interpreted correctly. Through the use of the DGLAP evolution equations, results from one energy scale may be evolved up to higher energy scales and can make useful predictions about kinematic regions never before explored. Such predictions and expectations form the backdrop against which the experimental data from the LHC will be measured.

Chapter 2

The Large Hadron Collider and the ATLAS Detector

2.1 Introduction

In this chapter a brief overview of the LHC is presented along with the principal physics programmes of ATLAS and the key design features of this detector. A summary of Monte Carlo generators is given before a discussion on event simulation and reconstruction at ATLAS.

2.2 An Introduction to the LHC

The Large Hadron Collider (LHC) is currently under construction by the European Organisation for Nuclear Research, CERN. The machine will accelerate two counter rotating beams of protons each of energy 7 TeV and collide them together giving a total centre of mass energy of 14 TeV. The machine has a design luminosity of 10 $\mathrm{nb}^{-1}\mathrm{s}^{-1}$ and is expected to provide energy and luminosity greater than any previous hadron collider. The LHC's high luminosity and centre of mass energy will

greatly advance our understanding of fundamental particles and the forces that act upon them.

2.2.1 The LHC Machine

A schematic diagram of the LHC machine is shown in figure 2.1. It is installed in a 27 km tunnel, approximately circular in nature and situated between Lake Geneva and the Jura mountains, straddling the Swiss-French border. It consists of 8 straight sections, each of approximately 538 m in length. Within these regions are the various services needed to run the machine and the four interaction points containing the principal LHC experiments. Points 1 and 5 contain the ATLAS and CMS detectors respectively, together with injection points from the SPS (point 1). The ALICE and LHC-b experiments are located at points 2 and 8. Located at points 3 and 7 are normal magnets responsible for collimating and thereby cleaning the beam. The RF system is located at point 4 (one system for each beam) and the beam dump is situated at 6.

The LHC will use existing particle sources and pre-accelerators, as shown in the accelerator chain of figure 2.2. Protons are obtained by heating hydrogen to form a plasma, thereby removing the orbiting electron. These protons are accelerated in CERN's LINAC2 up to energies of 50 MeV and then transferred to the Proton Synchrotron Booster (PSB) reaching 1 GeV. Acceleration is achieved through the use of RF cavities; electromagnetic waves of appropriate frequency are used to accelerate the protons though these sections. From the PSB, the protons move into the Proton Synchrotron (PS) and are accelerated up to 26 GeV, injected into the Super Proton Synchrotron (SPS) and reach 450 GeV. Finally they are transferred into the LHC and are accelerated up to the required 7 TeV.

Protons are steered around the LHC by superconducting dipole magnets which accelerate the bunches of particles in the required circular orbit. The maximum beam energy is limited by the magnetic field available to bend these protons and as

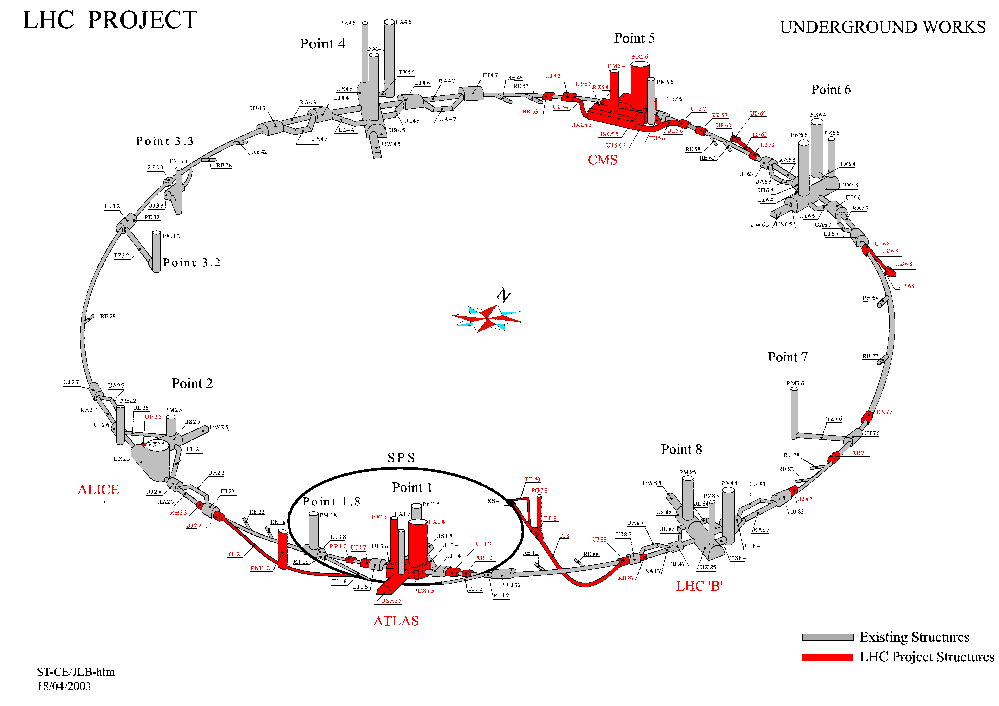

Figure 2.1: Underground works at the LHC.

a result the LHC uses the most powerful superconducting magnets ever used in an accelerator. These produce a maximum field of 8.37 T. Since the two proton beams counter rotate, they must circulate in opposite magnetic fields and therefore require separate beam pipes. Using an innovative design, the two pipes are housed within the same cryostat and mechanical structure, as shown in figure 2.3. The twin dipole magnets are arranged so the return field from one ring provides the field to the other, as shown in figure 2.4. This not only saves space, but also gives a significant cost saving on the alternative two device design.

Cooling the superconducting magnets is provided by superfluid helium at $\approx$ 1.9 K. The properties of superfluid helium, its high heat transfer capacity and zero viscosity, mean cooling can be performed more efficiently than if it were in its normal liquid state. Refrigeration power is provided by 8 cryoplants distributed around the 27 km ring. Four existing cryoplants will be upgraded providing half this need, whilst the remainder will be provided by purpose built plants.

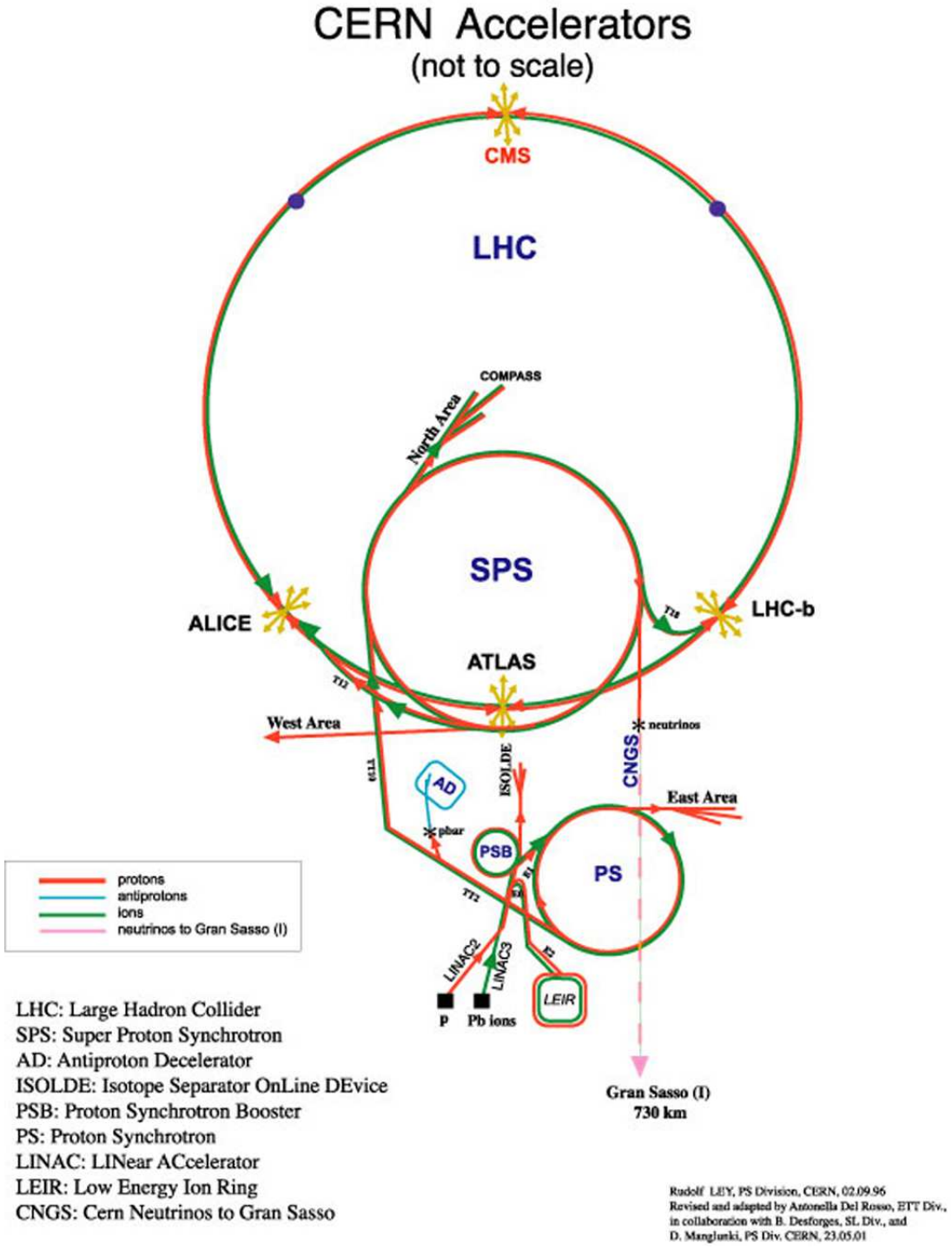

Figure 2.2: The LHC accelerator chain.

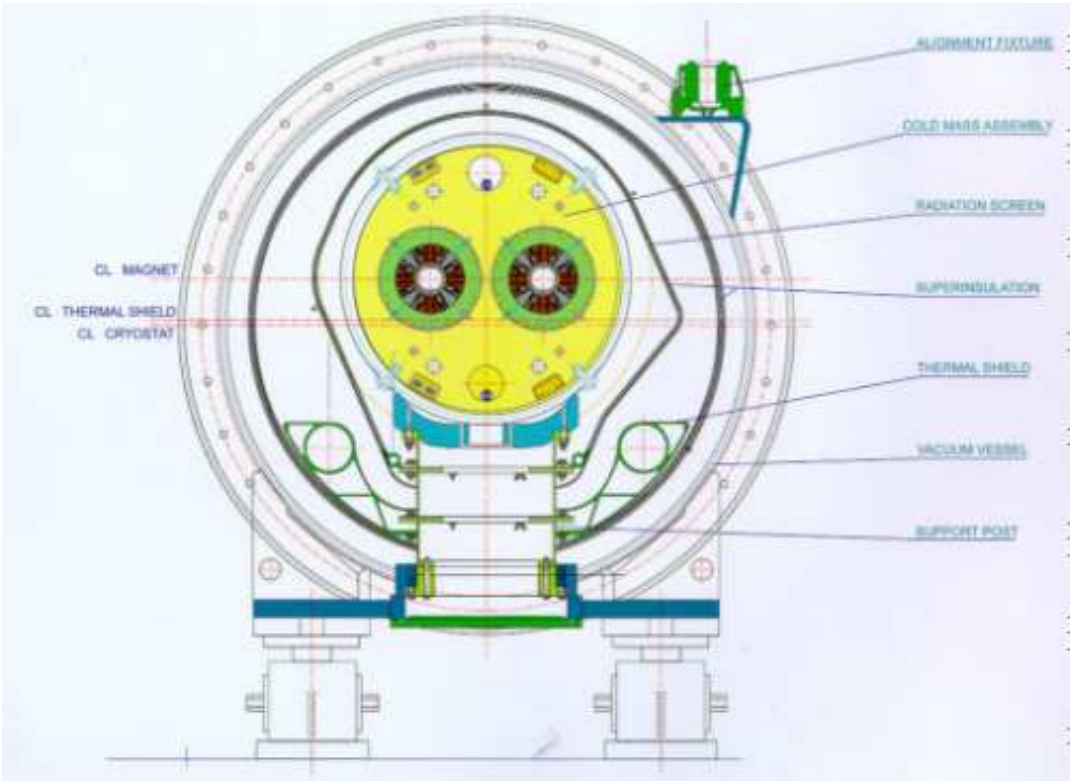

Figure 2.3: LHC dipole magnet.

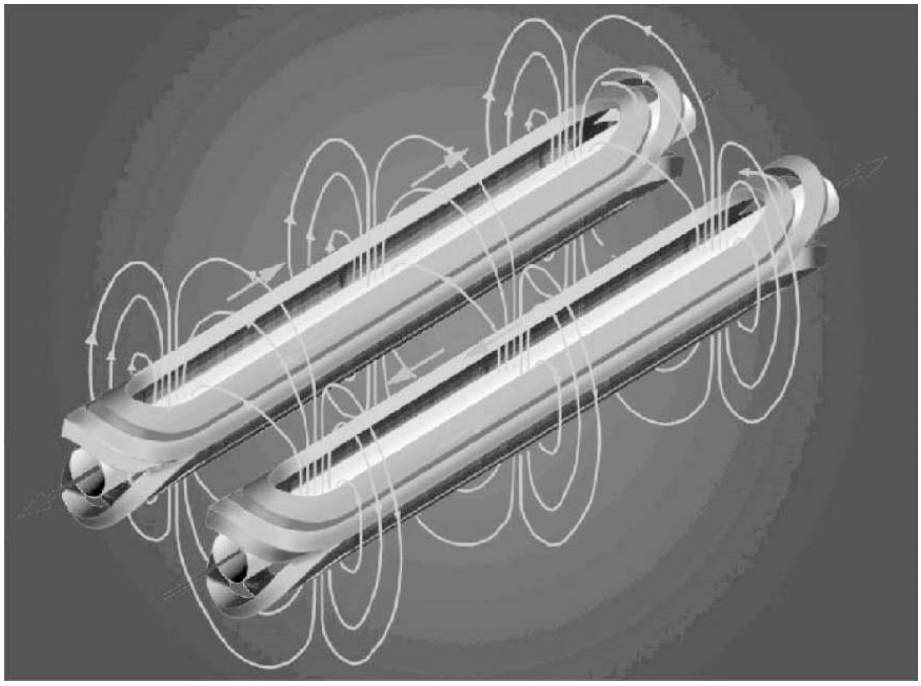

Figure 2.4: The LHC's dipole magnet field.

2.2.2 LHC Performance

The main parameters that determine the performance of the LHC, and therefore its access to potentially new and interesting physics, are its Luminosity (L) and its centre-of-mass energy ($\sqrt{s}$). The centre-of mass energy determines the amount of energy available for the creation of new particles. It should be noted that, due to the composite nature of the accelerated protons, only a fraction of the 14 TeV will be available to a given process. Nevertheless, the energies available will be almost a order of magnitude higher that the best currently available. The rate R (the number of events per second) of any given particle interaction is governed by the luminosity, such that

$$R = L\sigma_{int} \tag{2.1}$$

where σ_{int} is the interaction cross section. The total luminosity of any two

colliding beams is given by

$$L = f\frac{n_1 n_2}{4\pi\sigma_x\sigma_y} \tag{2.2}$$

where n_1 and n_2 are the number of particles in the two colliding beams, f is the frequency of collision and σ_x and σ_y are the transverse emittances of the beams. The average number of events produced per second is then given by,

$$< n >= \frac{L\sigma_{int}t}{F} \tag{2.3}$$

where t is the time interval between bunches and F is the fraction of bunches containing protons (in order to inject and extract protons a certain fraction of these bunches, around 20%, will be empty). Assuming a proton-proton cross-section of 70 mb and a bunch interval of 25 ns, 23 events per crossing are expected at the design luminosity of 10^{34} cm^{-2}s^{-1}. Once operating at this luminosity, the machine will be 2 orders of magnitude more luminous than the Tevatron; to date the most luminous hadron collider. A total of 2,808 bunches each containing 10^{11} particles are circulated around the two rings. The resulting high beam current ($I_b = 0.53$ A) and radiation environment will be a particular challenge to operating so close to the precision experiments at the LHC.

2.3 The ATLAS Physics Programmes

The principal physics programmes at ATLAS are detailed below. These cover a range of experimental interests, but by no means make up an exhaustive list.

• Higgs : The Higgs mechanism is the postulated process by which particles acquire mass. Associated with this, is the Higgs particle, or family of Higgs particles. To date this is the only unobserved particle in the standard model.

• SUSY : There exists a wide variety of extensions to the standard model motivated by the requirement of additional symmetries. These models predict a myriad of new particles, many of which, if present, may be detected in ATLAS.

• Top : Recently discovered, the top quark's mass is only weakly constrained and many of its properties have yet to be measured. The LHC's high luminosity should yield large numbers of top events with which to make such measurements.

• Electroweak : Precision measurements of the W and Z bosons and searches for anomalous couplings provide important tests of the standard model. These measurements will further our understanding of the theory and add to the body of data supporting it.

• B physics : Large amounts of b-quarks are expected at the LHC and will be used to study the flavour sector and constrain the Cabibbo-Kobayashi-Maskawa mixing matrix [20].

• Strong interactions : Measurements of parton density functions, the strong coupling constant (α_s) and QCD physics are important since they underlie all of the physics at the LHC. They represent interesting physics in their own right, but since they govern the initial states of all processes and form many of the sources of backgrounds, understanding them will be critical.

2.4 An Outline of ATLAS Detector

ATLAS (A Toroidal LHC Apparatus) is a multi-purpose detector designed to explore the new physics possibilities opened up by the LHC. Its goal is to provide accurate measurements for the wide range of physics processes occurring in the high luminosity environment.

Due to its cylindrical shape, ATLAS has adopted a polar co-ordinate system. The z direction is defined to be along the beam pipe, with the $x-y$ plane perpendicular

to the beam direction. The positive x direction is that pointing from the interaction point to the centre of the LHC ring, the positive y direction points upward and the azimuthal angle ϕ, is measured around the beam axis. The polar angle θ, is the angle to the beam pipe and pseudorapidity is defined as $\eta = -ln\ tan(\theta/2)$.

The design of ATLAS has been primarily driven by the standard model's predictions for new physics as well as other more exotic possibilities. The basic design criteria, as laid out in the ATLAS Technical Design Review [21] are;

• Very good electromagnetic calorimetry for electron / photon identification and measurements, complemented by full-coverage hadronic calorimetry for accurate jet and missing transverse energy (E_T^{miss}) measurements;

• High-precision muon momentum measurements, with the capability to guarantee accurate measurements at the highest luminosity using the external muon spectrometer alone;

• Efficient tracking at high luminosity for high-p_T lepton-momentum measurements, electron and photon identification, τ-lepton and heavy-flavour identification, and full event reconstruction capability at lower luminosity;

• Large acceptance in pseudorapidity (η) with almost full azimuthal angle (ϕ) coverage everywhere.

• Triggering and measurements of particles at low-p_T thresholds, providing high efficiencies for most physics processes of interest at LHC

The ATLAS detector measures 44 m in length by 22 m in diameter and weighs approximately 7000 tons. The design is shown in figure 2.5 and follows the familiar tracking, calorimeter, muon chamber configuration present in many multi-purpose detectors. ATLAS large size is driven primarily by its magnet systems. These comprise a superconducting solenoid magnet surrounding the Inner Detector and superconducting air-core toroids, providing a field for the muon system. Included below is a brief summary of the principal detector components, a fuller description

of which can be found in [21, 22].

2.4.1 The Inner Detector

The Inner Detector is contained within a cylinder 7.0 m in length, with radius 1.15 m. It consists of three subsystems; the pixel detector closest to the beam line, a silicon strip detector called the Semi-Conductor Tracker (SCT) and furthest from the beam line, a transition radiation tracker (TRT). These are placed inside a superconducting magnet, producing a field of ≈ 2 T in the central region. Since the solenoid is shorter than both the SCT and the TRT, this field deviates significantly from uniformity toward the ends of Inner Detector, dropping to around 0.5 T there. Charged particles are bent by this field and are detected as they pass through the three sets of detectors. The pixel, SCT and TRT, all provide space points from which the particle trajectory can be reconstructed. The TRT additionally provides information via transition radiation on the nature of the particles present.

The power dissipated by the various subsystems of the Inner Detector must be removed by suitable cooling systems. The pixel and SCT detectors use a coolant circulating through a series of aluminium pipes, reducing their temperature to $\approx -7^{o}$C. To prevent condensation forming on the detectors, they are also enclosed in a cold dry nitrogen environment. The TRT operates at ambient temperature and pressure and sits outside this enclosure. Since its cooling need is less this may be achieved through the circulation of CO_2 in the end-caps and by water cooled pipes running through the barrel.

Pixel Detectors

The pixel detector is the innermost detector and aims to provide high granularity precision tracking as close to the interaction point as possible. Its three precision measurements help to determine the impact parameter and enable the identification

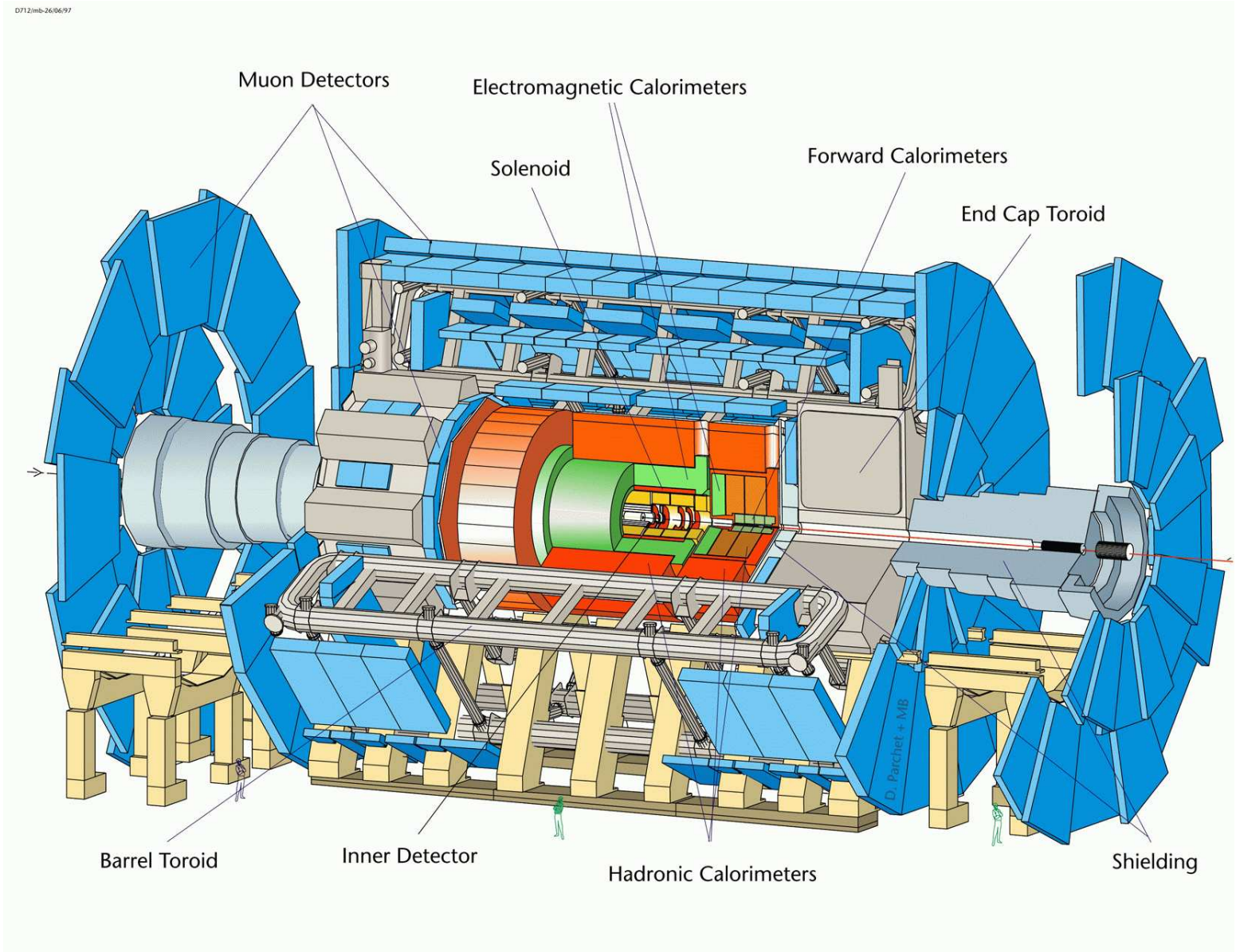

Figure 2.5: The ATLAS Detector.

of short lived particles such as B hadrons and τ leptons. The detector is made up of three barrels at $R = 4$, 10 and 13 cm from the beam line, together with 5 end-cap disks of radii between 11 cm and 20 cm. This gives an angular coverage of $|\eta| < 2.5$ for the innermost barrel layer, the so called B layer and coverage of $|\eta| < 1.7$ and $1.7 < |\eta| < 2.5$ for the other barrel layers and end-caps respectively. A total of 140 million detector elements, each of 50 μm in $(R - \phi)$ and 300 μm in z make up the detector. These are spread over 1,500 barrel and 700 disk modules giving a resolution of 12 μm in $R - \phi$ and $66 - 77$ μm in z.

Semiconductor Tracker (SCT)

The SCT system consists of silicon microstrip detectors providing four precision measurements per track. The detector is arranged into four barrels and nine end-cap wheels. The barrels have radii of 29.9, 37.1, 44.3 and 51.4 cm with the radii of each end-cap wheel being varied to ensure coverage in the range $|\eta| < 2.5$ is maintained. In total the detector contains 61 m^2 of silicon and 6.2 million readout channels. Each of the 4,088 barrel and end-cap modules is made up of four p-in-n microstrip detectors. Barrel detectors are 6.36×6.40 cm^2 and contain 768 readout strips of 80 μm pitch. These are wire bonded together in pairs to form a 12.8 cm long section and glued back to back, at a stereo angle of 40 mrad. The end-cap modules are similar; the main difference being that the silicon strips are tapered. This gives the detector a spatial resolution of 16 μm in R-ϕ and 580 μm in z/R, for the barrel/end-cap respectively.

Transition Radiation Tracker (TRT)

The outermost of the ATLAS tracking detectors, the TRT, is a combination straw tracker and transition radiation detector. It is made up of a barrel and four end-caps. There are 52,544 axial straws in the barrel, aligned parallel to the beam pipe. Each straw is 148 cm in length and covers radii of between 56 cm and 107 cm.

End-cap straws, 319,488 in all, lie at radii between 64-103 cm (inner end-caps), and 48-103 cm (outer end-caps). These are arranged in a fan shape, projecting outwardly from the beam pipe. Each channel gives a drift time measurement, enabling a spatial resolution of 170 μm to be calculated. This may be improved further by the use of a large number of tracks, giving a combination measurement better than 50 μm [21]. The transition radiation (TR) is provided by radiator foils between the straws and two independent thresholds enable the distinction between tracking hits (the lower threshold) and TR hits (the higher threshold) to be made.

2.4.2 The Electromagnetic Calorimeter

The electromagnetic (EM) calorimeter is a lead / liquid-argon (LAr) detector covering the pseudorapidity region $|\eta| < 3.2$. It is divided into three sections, a barrel $|\eta| < 1.475$ and two end-caps $1.375 < |\eta| < 3.2$, as shown in figure 2.6. Energy measurements for non-hadronic matter, principally electrons and photons are provided in the energy range 2 GeV to 5 TeV. Neutrinos, that pass through undetected, are identified though an imbalance of total energy in the event.

The calorimeter comprises three samplings over its entire η range, with a separate presampler in the range $|\eta| < 1.8$. A summary of the sampling granularity and coverage can be seen in table 2.1. The barrel region displays the highest level of granularity and it is this section of the detector, together with the outer end-cap wheels and the corresponding section of the Inner Detector, that is devoted to precision physics.

The three samplings in the EM calorimeter can be seen in figure 2.7. The first sampling comprises of a series of strips of $\Delta\eta \times \Delta\phi = 0.003 \times 0.1$, which translates into a pitch of 4 mm at $\eta = 0$. This high granularity enhances particle identification, in particular the rejection of light mesons (π^0, η, ω) against photons and electrons. The second and third samplings share a common cell structure, however, in the third sampling, to reduce the total number of channels, the neighbouring cells in η are

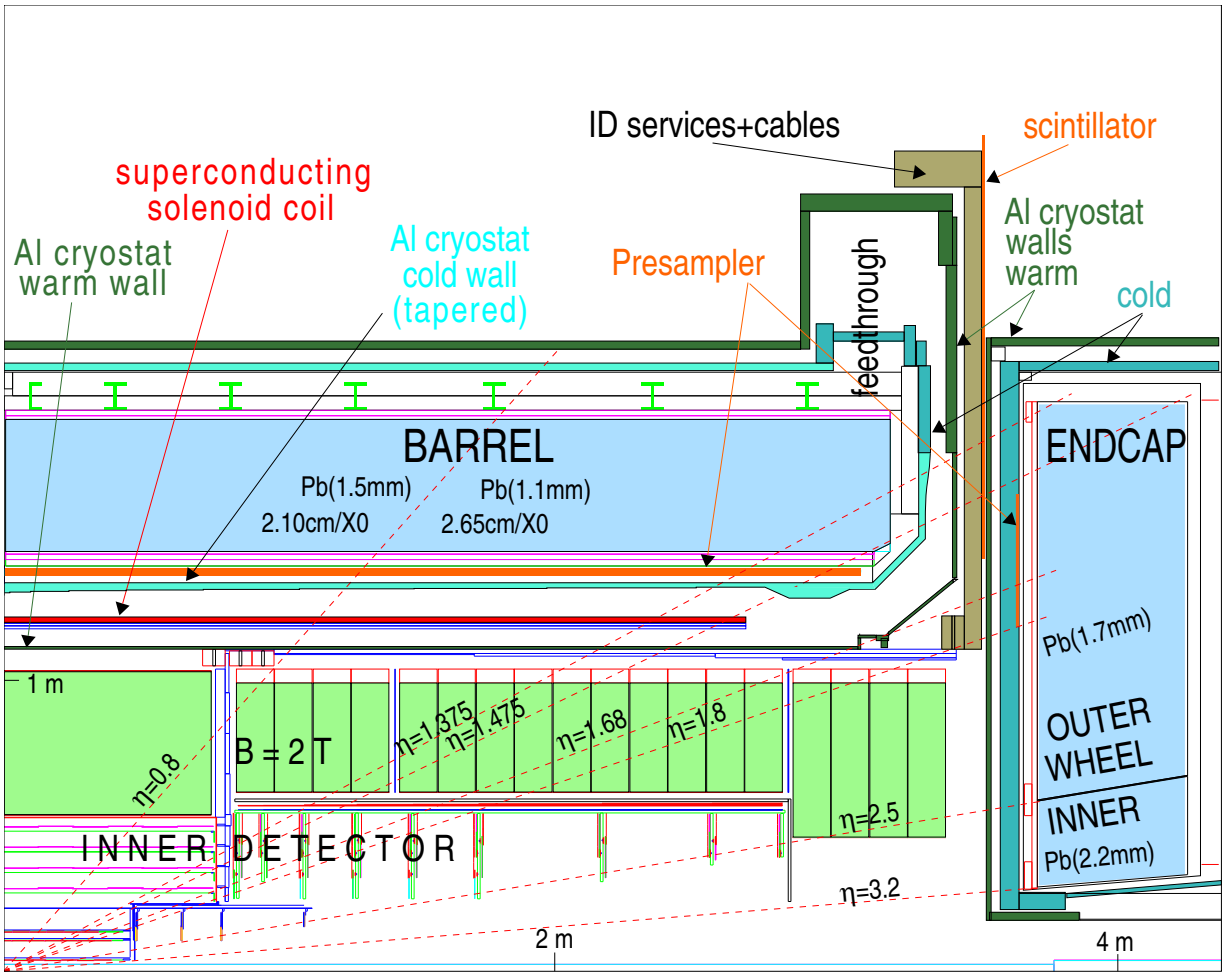

Figure 2.6: The ATLAS detector EM quadrant.

EM Calorimeter	**Barrel**	**End Cap**	
Coverage	$\|\eta\| < 1.475$	$1.375 < \|\eta\| < 3.2$	
Longitudinal segmentation	3 samplings	3 sampling	$1.5 < \|\eta\| < 2.5$
		2 sampling	$1.375 < \|\eta\| < 1.5$
			$2.5 < \|\eta\| < 3.2$
Granularity ($\Delta\eta \times \Delta\phi$)			
Sampling 1	0.003×0.1	0.025×0.1	$1.375 < \|\eta\| < 1.5$
		0.003×0.1	$1.5 < \|\eta\| < 1.8$
		0.004×0.1	$1.8 < \|\eta\| < 2.0$
		0.006×0.1	$2.0 < \|\eta\| < 2.5$
		0.1×0.1	$2.5 < \|\eta\| < 3.2$
Sampling 2	0.025×0.025	0.025×0.025	$1.375 < \|\eta\| < 2.5$
		0.1×0.1	$2.5 < \|\eta\| < 3.2$
Sampling 3	0.05×0.025	0.05×0.025	$1.5 < \|\eta\| < 2.5$
Presampler	**Barrel**	**End Cap**	
Coverage	$\|\eta\| < 1.52$	$1.5 < \|\eta\| < 1.8$	
Longitudinal segmentation	1 samplings	1 sampling	
Granularity ($\Delta\eta \times \Delta\phi$)	0.025×0.1	0.025×0.1	

Table 2.1: Electromagnetic calorimeter coverage, granularity and longitudinal segmentation.

combined.

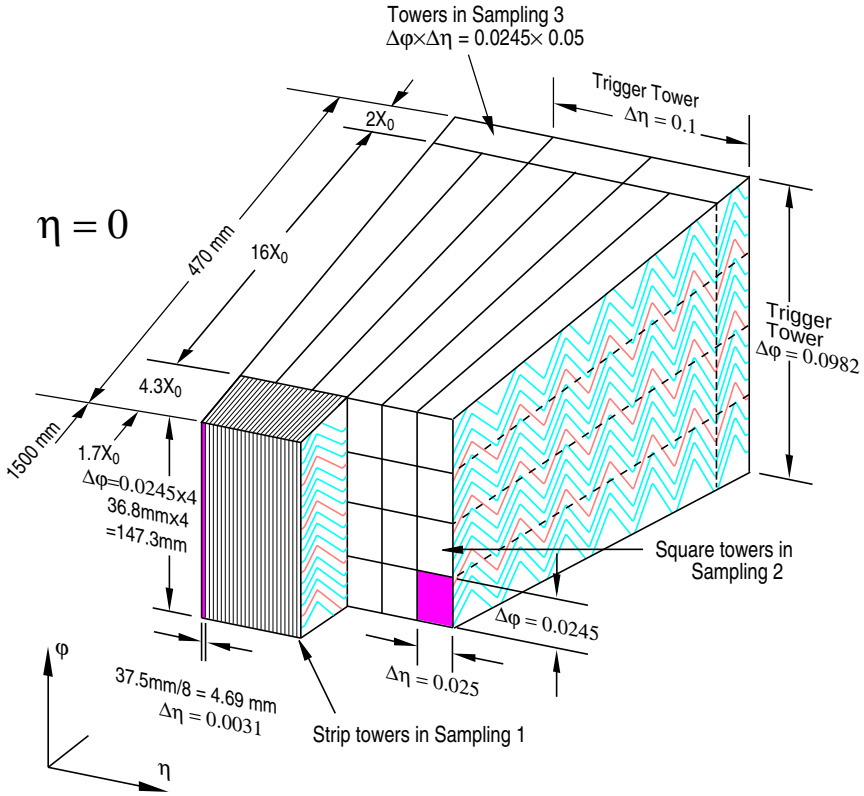

Figure 2.7: The ATLAS electromagnetic calorimeter, showing the three samplings and the accordion structure.

All the samplings in the EM calorimeters have an accordion shaped geometry providing complete ϕ coverage without any azimuthal cracks. This accordion wave is shown in figure 2.7 for the barrel, moving outward from the beam pipe. A diagram of the basic cell structure is shown in figure 2.8. It consists of a lead converter plate, a liquid argon gap, a readout electrode and a second liquid argon gap. Shower production is stimulated by the lead plates and as the charged particles produced travel through the argon they cause ionisation. This signal is collected at the electrode amplified by the electronics and read out. The structure of the end-cap is similar, but has the accordion wave parallel to the beam line, as shown in figure 2.9. The geometry is complicated by the fact that the wave amplitude must increase in proportion to the radius R and due to fabrication considerations must be split between

an inner and an outer wheel.

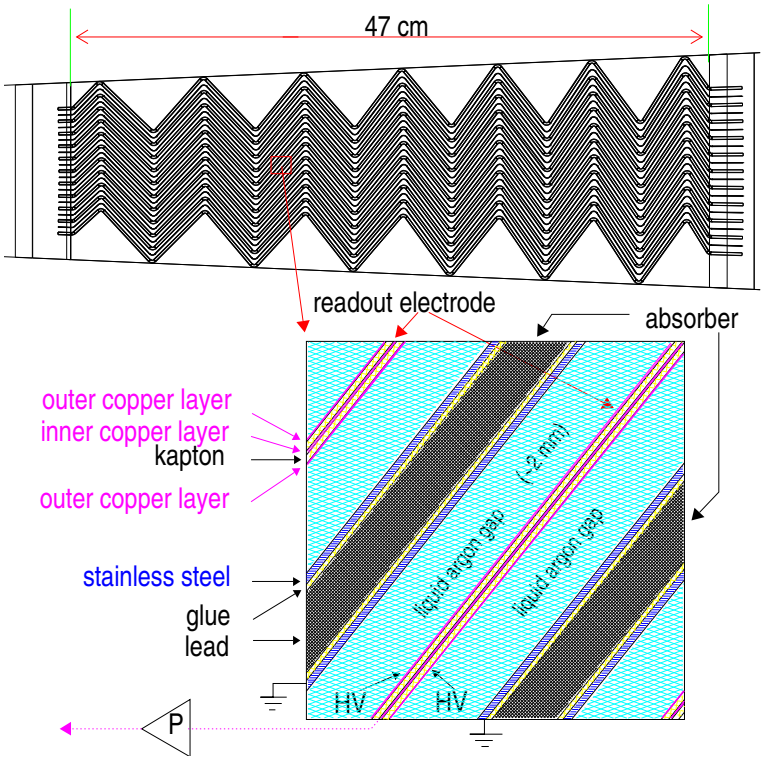

Figure 2.8: Barrel electrodes in the electromagnetic calorimeter.

Key changes in the calorimeter construction occur at $|\eta| \approx 0.8$, 1.4 and 2.5, and mainly mark the separation between the various parts of the calorimeter. These changes come from the physical constraints of the detector and a desire to maintain a total radiation thickness of at least 24 X_0 in the barrel region and 26 X_0 in the end-cap region [23]. At $|\eta| = 0.8$ the thickness of the lead converter plates decreases from 1.5 mm ($|\eta| > 0.8$) to 1.1 mm. This is to facilitate an increase in the sampling fraction with η as more space becomes available and should as a result increase the detector's resolution. The lead thickness in the end-caps increases from 1.7 mm between $1.4 < |\eta| < 2.5$ to 2.2 mm between $2.5 < |\eta| < 3.2$. This change compensates for the reduction in the number of plates and the increased angle of attack as you move from the outer to the inner end-cap wheels, as shown in figure 2.9. These changes to the calorimeter have an important impact on the performance of particle identification, as will be seen in section 5.4.

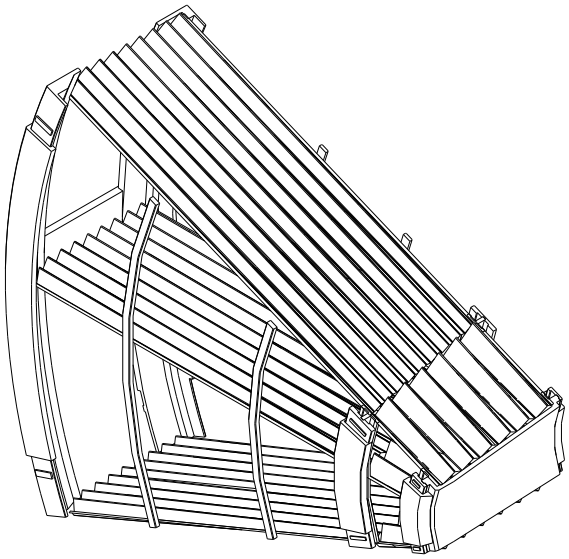

Figure 2.9: Electromagnetic converter plates for the outer and inner end-cap wheels. Only three plates out of a total of 96 in the outer wheel and 32 in the inner wheel are shown.

2.4.3 The Hadronic Calorimeter

The hadronic calorimeter covers the range $|\eta| < 4.9$ and is made from three differing technologies, depending on the varying requirements and the radiation environment across the detector. The hadronic barrel calorimeter or hadronic tile calorimeter is based on a cylindrical design using plastic scintillator plates embedded into an iron absorber. It covers the region $|\eta| < 1.7$ and is divided into a central barrel and two identical extended barrels. Due to the high radiation environment existing at high η, liquid-argon is used as the active material in the other two calorimeters types, the liquid-argon end-caps (HECs) and the forward calorimeter (FCAL). The HECs consist of two independent wheels covering a range $1.5 < |\eta| < 3.2$ and uses copper absorber plates. The FCAL is made from 3 sections covering the range $3.1 < |\eta| < 4.9$, with the first section using copper absorbers and the other two using tungsten.

2.4.4 Muon Detectors

Muon detection is based on the deflection of the particle in a large magnetic field. Over most of the η range the tracking is provided by Monitored Drift Tubes (MDT), however, in a region where the radiation will be highest, $2 < |\eta| < 2.7$ cathode strip chambers are used for the innermost plane. The magnetic field is provided by large superconducting air-core magnets. In the range $|\eta| < 1.0$ this is a large barrel toroid magnet whilst in the region $1.4 < |\eta| < 2.7$ the tracks are bent by two smaller end-cap magnets. The transition region $1.0 < |\eta| < 1.4$ uses a combination of barrel and end-cap fields and these fields are deigned so as to be mostly orthogonal for the muon trajectories over the entire η range.

2.5 Monte Carlos

A Monte Carlo (MC) event generator specialises in modelling the interaction of colliding particles. Processes of interest are selected along with parameters such as beam particles, centre of mass energy, particle masses, lifetimes, branching ratios, decay channels and kinematic constraints. These are used to calculate a matrix element and the experimental cross section for the process of interest. Random events are generated according to the probability of obtaining certain final states. Output is given in the form of an event listing containing the four-vectors and type of each final state particle. Many particle generators also present their output in the HEP-MC [24] event format, allowing for different stages of the event generation to be handled by different programs.

For the case of proton-proton collisions, the colliding particles are the partons of the protons and these are selected with probability determined by the parton density functions. The remaining proton remnants form the underlying event, with various general and standalone Monte Carlos existing for its simulation. Partons, that are present in the final state, fragment into stable colourless particles and

again many models and implementations exist for their simulation. Ultimately the success for any Monte Carlo lies with the comparison to data and to this end a great deal of effort will be devoted to understanding differences between the two. Many Monte Carlo parameters can be adjusted and by tuning these, good agreement with experimental data should ultimately be obtained.

2.6 Detector Simulation

Event simulation in the ATLAS experiment is summarised in figure 2.10. It comprises four basic parts; Monte Carlo event generation (discussed above), detector simulation, digitisation and finally event reconstruction. The ATLAS detector is simulated using the Geant4 software package [25, 26]. It contains ATLAS specific information such as geometry, material make up and magnetic fields and then uses these to model the passage of particles through the detector. It simulates both the interaction of particles with the detector, including the possible production of new particles and the anticipated detector's response. Output from the Geant4 simulation is in the form of the expected signals from the various detector subsystems. These signals are then passed to a digitisation simulation which mimics the readout electronics and introduces effects such as noise and, where necessary, pileup. The final stage in the chain is event reconstruction; this takes the digitised detector output and forms data objects (ESDs and AODs) from which the final analysis is performed. Tracking algorithms, cluster finders and loose particle identification are all performed during this reconstruction stage. Final particle identification and event selection is performed by the user as part of their analysis.

A fast detector response ATLFAST [27] is also available. This takes the Monte Carlo truth particles from the generator and directly outputs events in the AOD format. The program essentially works by smearing the energy and momentum of stable Monte Carlo particles, producing an anticipated detector response without performing any detailed simulations. As a consequence, no particle misidentification

or detector efficiencies are included within the default version of the program.

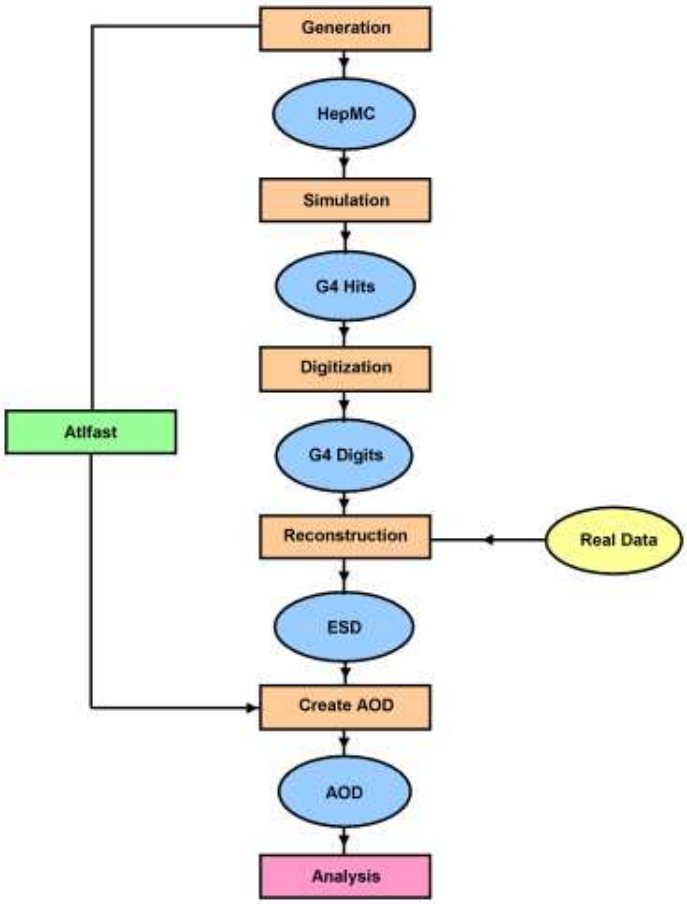

Figure 2.10: The ATLAS simulation chain.

2.7 Conclusion

An overview of the LHC experiment and physics goals has been presented together with the principal components of the ATLAS experiment. Both the LHC and ATLAS are currently still under construction, but are expected to enter the commissioning phase shortly. Monte Carlo event generators and detector simulations have been developed to model anticipated physics processes at ATLAS. The successful operation of both of these will be required to understand the results produced by

the experiment.

Chapter 3

The ATLAS SCT Barrel

3.1 Introduction

This chapter details work carried out to evaluate the performance of the semiconductor tracker (SCT) barrel hybrids. The chapter begins with a short introduction to the SCT, giving the context within which these devices are expected to perform. This is followed by a brief overview of the physics behind the ATLAS silicon detector, before a more detailed introduction to the chips tested as part of this work. A summary of the tests and results obtained are presented together with explanations of the most common types of failures.

3.2 Physical Structure

The SCT barrel forms part of the ATLAS Inner Detector, as shown in figure 3.1. It consists of four concentric barrels each 1.5m in length and covering radii from 299 to 514 mm from the beam pipe. The basic component of the system is the module, figure 3.2, with a total of 2,112 of these identical units being mounted around the four barrels parallel to the beam line. Mounting these with a small

angle, allows neighbouring modules to overlap by 1-2 mm in the $R - \phi$ direction, as shown in figure 3.3. Modules comprise four single sided silicon sensors, a base board and a hybrid containing twelve chips. The silicon sensors are the active part of the detector, registering the passage of charged particles. Mechanical rigidity and thermal transfer is provided by the baseboard, whilst the hybrid contains all of the read out and calibration functionality.

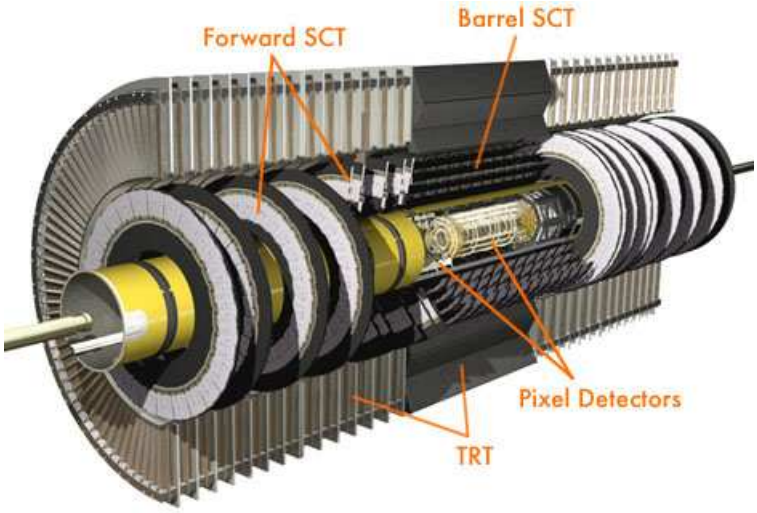

Figure 3.1: The ATLAS Inner Detector.

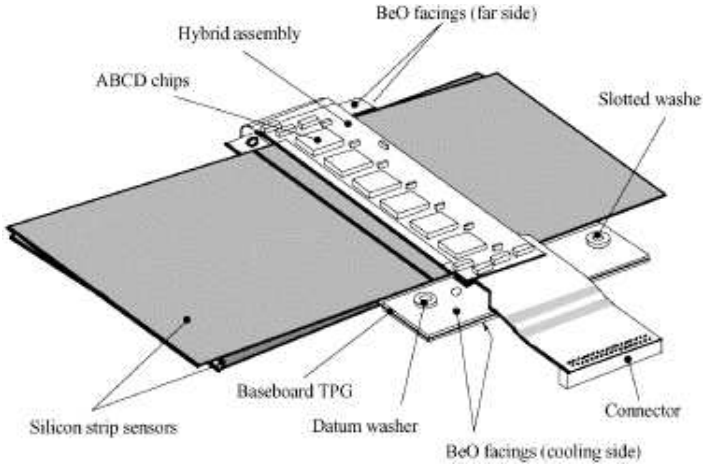

Figure 3.2: Diagram of a SCT barrel module.

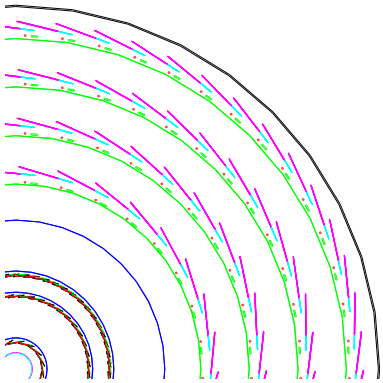

Figure 3.3: An end on view of an SCT and pixel barrel quadrant. The SCT modules are mounted on the four outer barrels with a small angle allowing neighbouring modules to overlap. Also shown are the three pixel layers - the innermost rings.

3.3 The ATLAS Silicon Detectors

The detectors used in the SCT consist of an n-type substrate with p-type detector strips. Between the two material types, a p-n junction is formed. The majority carriers in each type are free to diffuse into the neighbouring region, leaving a region almost completely devoid of free charge carriers. With the application of an applied voltage, it is possible to extend this region across the entire n type material. Charge, created by the passage of an ionising particle, will then be accelerated by this voltage and can be collected and read out.

3.3.1 ATLAS Chosen Detector Design

The p-in-n solution chosen by the collaboration [28] consists of 768 AC coupled readout strips of pitch 80 μm and width 22 μm. The substrate is 285 μm thick and has an un-irradiated depletion voltage of 150 V. A schematic diagram of the substrate is shown in figure 3.4; table 3.1 shows the acceptance criteria as detailed in [29].

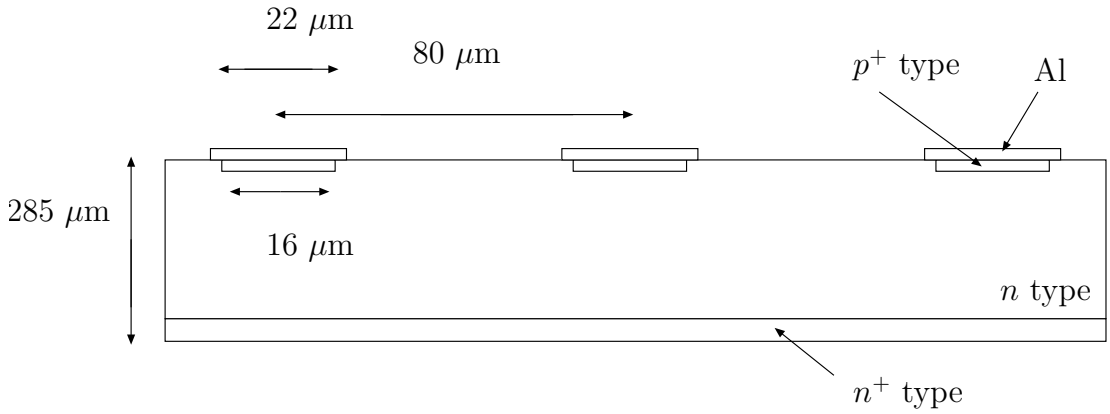

Figure 3.4: Schematic diagram of the silicon sensor.

Leakage current at 20^{o}C	<6 μA at 150 V, <29 μA at 350 V,
Current stability at 20^{o}C	ΔI <2μA during 24hrs at 150 V
Depletion voltage	< 150 V
Bias Resistance	1.25 $\pm$0.75 MΩ
Coupling capacitance	$\geq$ 20 pF cm^{-1} at 1 kHz
Inter-strip capacitance	< 1.1 pF cm^{-1} at 100 kHz
Strip metal resistance	< 15 Ω cm^{-1}
No. of good strips	> 98% per detector, mean of > 99% in a batch

Table 3.1: Acceptance criteria for the SCT silicon sensors, as detailed in [29].

Signal Creation

The energy deposited by an ionising particle passing through silicon, can be described by the Bethe-Bloch equation, taking ≈ 3.6 eV to create an electron-hole pair [30]. Given the most probable amount of charge deposited is 85 keV, around 24,000 electron-hole pairs should be created by a single track. Once created, these charge carriers are then accelerated in the presence of the applied electric field and are collected at the electrodes. Holes are accelerated toward the p^+ implants, electrons toward the backplane. Aluminium readout strips, coupled to the p^+ implants, take the induced signal to the readout electronics. Due to the very short pulse time characteristic of silicon, these charge signals are collected in times typically < 10 ns.

3.3.2 The ABCD3TA Chip

Chip Requirements

Before being read out by the Data Acquisition System (DAQ), the analogue signal created by a track is digitised by the ABCD3TA [31,32] chip. A total of twelve chips are used on each barrel module, with each chip being required to process and read out the output from 128 channels. This should be achieved with less than 1% data loss, at an average trigger rate of 100 kHz. The main functions performed by the chip are [32]

- charge integration
- pulse shaping
- amplitude discrimination
- data latching
- storage for first level trigger latency

- derandomisation and data compression
- data transmission

Design Overview

ABCD3TA chips are constructed using a radiation resistant BiCMOS process (DMILL technology). It uses CMOS devices with 0.8 μm minimum gate lengths and bipolar transistors. A block diagram of the chip can be seen in figure 3.5.

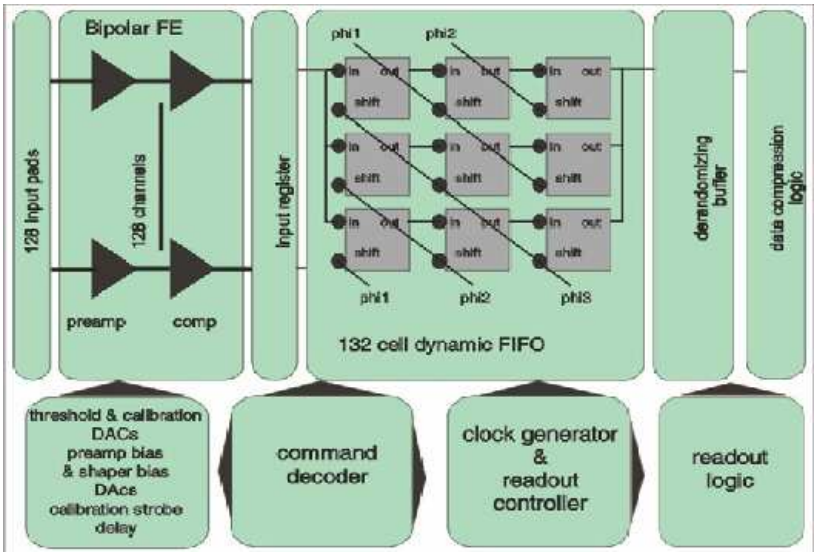

Figure 3.5: Block diagram of the ABCD3TA chip, taken from [32]

Input and the Front End

The 'front-end' of the chip consists of a preamplifier, shaper and discriminator, together they form the analogue part of the chip. The preamplifier takes the charge signal received from the silicon sensors and amplifies it by an amount specified by shaper currents. The gain expected at the discriminator input, for a shaper current of 20 μA, is 50 mV per fC of charge created.

The discriminator is a comparator in the Schmitt trigger configuration; that is it has a feedback loop to one if its discriminator inputs. As a result the discriminator has the ability to "remember" its most recent output, ensuring that for each event once the hit is registered the signal is maintained for that event, until reset. The discriminator threshold is controlled by a differential voltage applied to one of its input pins. When the signal is below this threshold, the discriminator returns its most negative value "0", when above, its most positive value, "1". This threshold voltage is common for all 128 channels and is generated by an internal 8-bit DAC. It can cover the range from 0 mV to 640 mV in steps of 2.5 mV. Given the front-end gain of 50 mV per fC, this equates to an available range from 0 fC to 12.8 fC. It has a nominal setting of 1 fC.

The actual threshold value for each of the 128 channels depends not only on the gain in the front-end, but also on the discriminator's offset. In fact it can be seen that the dominant effect on the threshold variation is the discriminator offset, as will be shown in figure 3.9. Not only do these offsets vary on a channel to channel basis, but it was found that the spread increased considerably after irradiation [33]. Since a critical performance criterion is the homogeneity of all of the silicon strip channels, a threshold correction mechanism was introduced [33]. These so called trim settings are controlled by two registers, a 2-bit TrimRange register and a 4-bit TrimDAC. The TrimRange sets the size of the voltage steps to be added to the discriminator threshold and has 4 scales (4 mV, 8 mV, 12 mV and 16 mV). The number of voltage steps of this range is determined by the TrimDAC. There are 16 different settings and as a result a total range 0 - 240mV is available. The process by which the optimal settings for the TrimDAC and the TrimRange are determined, is known as trimming.

Should a channel be untrimmable, or defective in another way, a mechanism exists by which these channels may be masked. The mask register sits in between the discriminator and the pipeline and can be configured to remove the signal from any channel.

Calibration

An important feature of the ABCD3TA chip is that its various internal settings can be periodically tested and optimised. To this end, there exists internal calibration capacitors, one for each channel, allowing for the injection of test charges. Every fourth channel can be tested simultaneously and injected charges range from 0 - 16 fC in 0.0625 fC steps.

The calibration strobe sets the timing of the injected test charge. This ensures that the discriminators, firing at the clock frequency, will be synchronous with the calibration signal. However, due to the design implementation, the actual delay is dependent upon process variation and as a result needs to be calibrated. The delay of the strobe, with respect to the clock phase, is controlled by the strobe delay register and can be tuned within a range of 50 ns.

Pipeline

The pipeline is a dynamic memory array, a mechanism by which, for a particular beam crossing, the data associated with that crossing can be temporarily held until the trigger has been received. Once the level 1 (LVL1) trigger has been received, data are either read out, or discarded. This is achieved through the use of a FIFO circuit, an array of 12x12 dynamic memory cells. The output for a channel is multiplexed into twelve rows and as the pipeline clock increments (which has 1/12 the frequency of the beam crossing frequency) the data progress through the memory cells. The delay provided by the device is 12x(12-1) clock cycles long, after which time, the data are overwritten. On receipt of an LVL1 trigger the last three bins emerging from the pipeline are copied into the readout buffer.

Readout and Compression

The readout buffer temporarily stores the three bits of data copied from the pipeline. These three bits correspond to the three beam crossings centred on the LVL1 trigger. The buffer is 128 channels wide and 24 locations deep. It allows data from eight LVL1 triggers to be held, and ensures that whilst LVL1 triggers may come randomly, the readout may be performed at the average rate of LVL1 triggers. This reduces the specifications, and therefore the cost and size of the transmission system.

Since for any given event an average hit rate of 1% is expected, few channels will contain relevant data. This is then used to reduce the volume of data needed for read out. Data compression logic rearranges the three 128-bit words representing an LVL1 trigger event into one hundred and twenty eight 3-bit words. Depending on the level of output required, it then compresses data and the readout chain can be initiated.

3.3.3 Hybrid Design

The hybrid is a multilayer design made from copper/polyimide, with a carbon-carbon bridge material for strength. A total of four active layers contain connections for signal circuits, digital / analogue grounds and the power plane. The copper/polyimide provides a flexible base 279 μm thick in the body and 149 μm in the wrap-around region, as shown in figure 3.6. The carbon-carbon bridge is required to have good thermal conductivity, high Young's modulus and low radiation length. It is 0.3 mm thick, with legs at both ends of 0.5 mm. Since the microstrip detector's pitch is larger than the chip's input pads (80 μm vs 48 μm) a pitch adaptor is required. Wire bonds are made firstly from the chip to the pitch adaptor and then later, from the pitch adaptor to the sensor.

Each hybrid is divided into two sides which are designed to operate independently; Link0 and Link1. Chips on these Links sit in horizontal rows with the chip

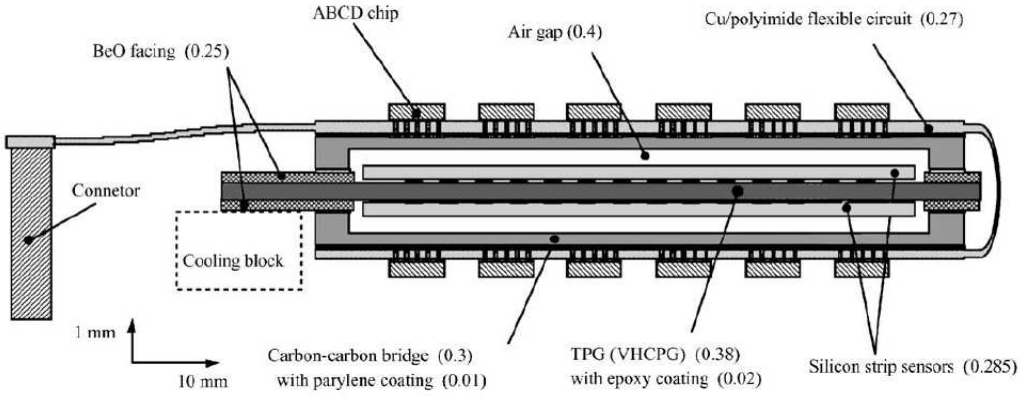

Figure 3.6: Cross-section of the SCT barrel module. The vertical direction has been magnified by 5 and the component thicknesses are given in mm. Figure taken from [34].

in the first position being designated the 'master' and all other chips designated as 'slaves'. 'Masters' are responsible for receiving commands from the DAQ and initiating readout; 'slaves' relay commands up and down the line.

3.4 Fabrication and Assembly of Hybrids for Barrel Modules

Barrel module assembly was carried out in the four 'clusters' of Japan, UK, Scandinavia and US. The UK cluster is split between Birmingham, Rutherford Appleton Laboratory (RAL) and Cambridge. At Birmingham chips were mounted, bonded onto hybrids and a series of electrical tests were conducted to ensure satisfactory performance. The remaining work was performed at RAL, where sensors, tested initially at Cambridge University, were mounted upon base-boards and then connected to completed hybrids.

An outline of the production steps performed at Birmingham is shown table 3.2.

Hybrids were first visually inspected to ensure no damage was sustained during transit. Next an IV test was performed; the Hybrid being required to have a leakage current < 0.03 mA at 500 V. Test bonds were then made and were required to withstand a force of 0.06 N, ensuring acceptable bonds could be formed. Once these initial steps had been done, ABCD3TA chips were then selected and attached to the hybrid.

	Production step
1.	Hybrid initial visual inspection
2.	Hybrid IV Test
3.	Hybrid bond pull test
4.	Selection of ABCD3TA chips for hybrid
5.	Gluing of ABCD3TA chips to hybrid
6.	Curing of chip-hybrid glue
7.	Wire-bonding of chips to hybrid
8.	Visual inspection after wire-bonding chips
9.	Hybrid main electrical test
10.	Hybrid long-term test
11.	Hybrid cold test
12.	Wire-bonding of chips to pitch adaptor
13.	Visual inspection after wire-bonding pitch adaptor
14.	Hybrid final electrical test
15.	Rework needed
16.	Packing

Table 3.2: Hybrid assembly steps carried out at Birmingham.

An electrically conductive epoxy, Eotite p-102 dispensed by an automatic machine, was used to glue the chips to the hybrid. The glue was then cured at 50^oC for 2 hours and electric contacts were made from the chip to the hybrid using 25 μm, 99% Al 1% Si wire. Bonds were formed using an automated ultrasonic bonder

operating at 60 kHz with power being applied for between 18-22 ms. After the chip's performance has been successfully tested and evaluated, see section 3.5 below, the first stage of the pitch adaptor bonding was performed. Using the 0.25 μm wire a connection was made from the chip input pad to one side of the pitch adaptor. The remaining pitch adaptor bond, from the pitch adaptor to the sensor was completed at RAL. In total there are around 5200 wire-bonds per module.

3.5 Hybrid Electrical Tests

During assembly, hybrids undergo a variety of electric tests to ensure that their characteristics are within acceptable bounds. These tests are performed at room temperature ($\approx 27^o$C), warm ($\approx 38^o$C) and cold ($\approx 0^o$C) as measured by the thermistors on the hybrids. Whilst the conditions present in the cold test are closest to those in the actual experiment, the other tests are used as preliminary assessments and checks against chip infant mortality. Test lengths depended upon the number of hybrids being tested. Typical times for the main electrical test were 4-5 hours, the cold test $\approx$ 12 hours and the final test $\approx$ 1 hour. The length of the warm test was reduced from 90 hours to 12 hours as possible mortality rates in chips did not materialise.

3.5.1 System Set-up

Facilities at Birmingham allowed the simultaneous testing of three batches of hybrids. There was a six channel test system used to test hybrids at temperatures of 27-38^oC, a single test system for room temperature tests and a dedicated six channel cold test system. Hybrids were mounted on aluminium jigs, as shown in figure 3.7. These secured and protected the hybrid, as well as providing a good thermal contact for cooling. Hybrids generate up to 6 W of heating power and it is therefore necessary to cool them to maintain the desired operating temperature. For room

temperature and warm tests this was achieved by securing the jigs to metal plates cooled by chilled water. Cold tests were conducted in a commercial freezer set to an appropriate temperature with a continuous flow of dry nitrogen being used to prevent the formation of condensation. Hybrids were electrically isolated from the freezer by placing them on a piece of electrical insulating material.

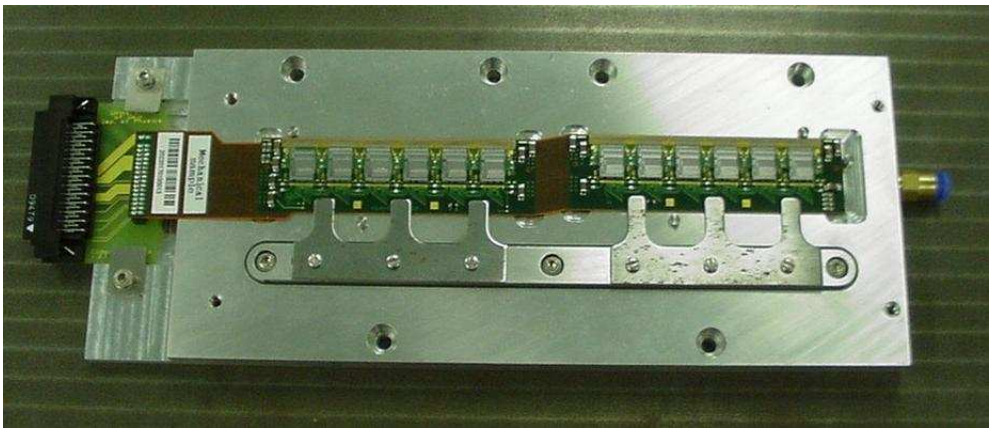

Figure 3.7: A completed hybrid with chips and components mounted. The Aluminium jig can be secured to a cooling system providing good thermal contact. When the lid is fastened the delicate structure is protected and dry nitrogen can be flushed over the surface.

A set of custom VME cards was used to read out and control the hybrids. Each test system had a SLOG (SLow cOmmand Generator), MuSTARD (MUlti-channel Semiconductor TrAcker Readout Device), SCT low voltage card (SCTLV) and a SCT high voltage card (SCTHV). The SLOG provided the 40 MHz clock signal and was used to send commands and triggers to a maximum of 6 barrel hybrids. Readout functionality was provided by the MuSTARD which did a limited amount of signal decoding and histograming. Power for the hybrids was provided by the low voltage card, giving the 3.5 V and 4.0 V needed for the analogue and digital parts of the chip. Earlier tests also used a CLOAC (CLock And signal Card) to generate high rates of pseudo-random trigger bursts, however these were removed due to reliability issues and the triggering performed solely by the SLOG. Control and analysis of the system was provided via a ROOT-based DAQ system called SCTDAQ [35].

3.5.2 Digital Tests

HardReset

Together with the full-bypass, redundancy and the pipeline tests, this forms one of the digital tests. Its aim is to ensure that the clock, command and hard reset signals are received correctly. Firstly each master chip outputs, via its data-link, the clock frequency divided by two, confirming that the clock signal has been received. Configuration commands are then issued to the chip, which amongst other things stops its clock. Finally the hard reset command is sent resetting the chip, which again outputs the clock frequency divided by two. Clock signals are verified by the user using an oscilloscope; currents and voltages are recorded by SCTDAQ.

Full Bypass Test

Since chips are connected together in a daisy chain arrangement, data from each chip must pass through all the chips upstream of it in order to reach the master and be read out. Failure of one of these chips could then incapacitate an entire side of a module. To avoid this, a redundancy feature is build in; dead chips can be bypassed using an alternative path. Each of these bypass configurations is tested over a range of supply voltages (V_{dd}) to ensure the chip has the required redundancy. A burst of triggers is sent for each configuration, and in order to have a predicted response which can be checked, the chips are instructed to return their mask files. Chips are required to pass this test at voltages at and above 3.8 V.

Redundancy Test

Should the link to a module fail, it is possible to send clock and command signals to the module from its neighbour. The redundancy test ensures that this functionality operates correctly. Chips are instructed to return their mask files for each of the

primary and redundant clock and command options.

Pipeline Test

The pipeline is cleared by a soft reset command and a number of clock cycles later, a known pattern is inserted into a given location. By varying the delay between the soft reset and the pattern injection, differing paths within the pipeline can be selected. The test is performed twice, once with all channels on, to detect dead cells in the pipeline and once with all channels off, to detect stuck cells in the pipeline. Defects such as these will have differing effects in the experiment. A dead cell will mean that 1/12 of the true hits to the channel will go undetected, since they will pass though a dead (unresponsive) pipeline cell. A stuck cell on the other hand will continuously give a hit because no matter what the input to the pipeline is, a hit will emerge due to one of the cells being stuck "on". Since the mask register is before the pipeline, this effect cannot be removed on the detector and must be corrected after readout. As a result valuable readout bandwidth is taken up with invalid data and the number stuck-cells is therefore be kept to a minimum.

3.5.3 Analogue Tests

These tests are designed to assess the front-end performance of the ABCD3TA chip. There is only one basic type of test for the front-end: the threshold scan. The number of different ways it can be performed make up the remaining tests.

For the threshold scan, the output of a channel (for a given input of charge) is measured systematically as the threshold is varied. The channel's response to an injected charge is to record a "1" (hit) or a "0". This is sampled over a large number of events building up a statistical picture of how the channel behaves. The occupancy of the channel is then measured for differing charges over the possible range of thresholds settings. Plotting the occupancy as a function of threshold yields

an s-curve, characterising the behaviour of that channel, as shown in figure 3.8. From s-curve plots it is possible to see that at low thresholds all the events return a hit since the input signal at the discriminator is likely to be above this value. As the threshold is increased, at some point the occupancy of the channel is reduced and continues to fall until it reaches zero. The shape of this plot resembles a back to front S and is a characteristic of the noise present in the system.

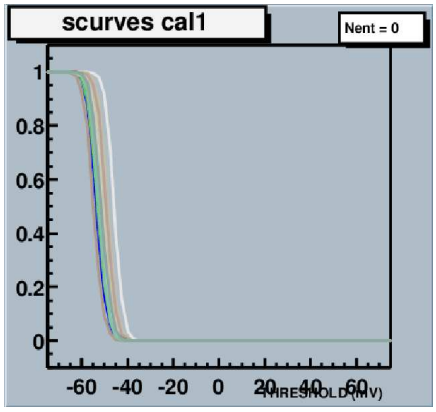

Figure 3.8: Typical plot of a hybrid's 's' curve showing all 128 channels from one chip. Plotted is each channel's occupancy as a function of threshold. The threshold values shown are relative to the threshold needed to obtain an occupancy of 50% for 1 fC of injected charge. Since for this scan no charge has been injected, at low thresholds the channel fires on background noise. The shape and width of the curve characterises the noise. The channel to channel spread is because the channels have been trimmed at 1 fC and therefore are designed to operate uniformly for this level of injected charge. Since they are firing on noise and not 1fC they do not operate uniformly and exhibit the observed spread.

Noise

The level of noise in the system is a critical parameter since it determines the threshold needed to record a hit. This then in turn influences the number of noise

hits read out and also the efficiency of particle space-point detection. Both of these factors feed into the overall tracking efficiency of the Inner Detector.

The random noise of any given detector channel can be assumed to be a Gaussian with the form

$$P(x) = \frac{1}{q_{rnd}\sqrt{2\pi}} \exp\left(- \frac{x^2}{2q_{rnd}^2} \right) \tag{3.1}$$

where x is the size of random noise and q_{rnd} is the variance characterising the Gaussian. x and q_{rnd} are in units of electron charge. Noise above a given threshold q_{thr} will contribute to the observed occupancy O of a channel which is given by

$$Occupancy = \int_{q_{thr}}^{\infty} P(x)dx \tag{3.2}$$

This is the complementary error function (erfc), or s-curve.

$$Occupancy = \frac{1}{2}\mathrm{erfc}\left(\frac{q_{thr}}{\sqrt{2q_{rnd}^2}} \right) \tag{3.3}$$

The width of the s-curve, measured in threshold mV, is directly related to the input noise of the system. The output noise may be found by fitting a complementary error function to the measured s-curve, obtaining q_{rnd}. Dividing this by the measured gain, the input noise can be calculated.

Since the threshold scan and s-curve form the basic test, a convenient measure of a channel's performance is the threshold value needed to obtain an efficiency of 50% i.e. for an injected charge of x fC the probability of the channel returning a "1" is 50%. This threshold value is known as the Vt50 point.

Three Point Gain

Here threshold scans are performed for three levels of injected charge, 1.5 fC, 2.0 fC and 2.5 fC. To obtain the Vt50 point for each of the injected charges, an s-curve is measured using 1000 triggers per threshold point. These Vt50 points are then plotted against injected charge. Since the amplification is a linear process (to better than 5% from 0 to 4.0 fC), a fit may be made giving the gain (slope), and the offset (intercept) of the channel. Individual channel measurements of these quantities for an input charge of 2.0 fC can be seen in figure 3.9, left hand plot. Chip averaged values of Vt50, gain, output and input noise as a function of charge can be seen in figure 3.9, right hand plot. The channel to channel variations shown in these plots are typical.

Strobe Delay

The strobe delay scan optimises the timing of the injected calibration charge. The charge is delayed so that it arrives at the discriminator input as it fires at the correct phase relative to the clock frequency. If the delay in injecting the test charge is too short, then the discriminator will fire too late. If it is too long, the discriminator fires too early. The scan uses a 4.0 fC injected charge for a discriminator threshold of 2.0 fC. The strobe delay is recorded in an 8-bit register; only the first 6 bits of this are used giving the delay a range of 0 to 63. For each strobe delay value 1000 triggers are sent and the number of responsive channels is recorded.

The region where the strobe delay ensures that the charge pulse is caught, is usually $\sim$25 strobe delay units wide. It can be seen in figure 3.10 that there exists significant channel to channel variation in the delay within certain chips. The strobe delay is set to be a certain fraction into this active region, see the shaded area of figure 3.10. Since this fraction can only be set for the entire chip, in extreme cases it can lead to problems in the calibration performance of channels. It was especially noticeable that on some chip lots using a strobe delay fraction of 25% led to regions

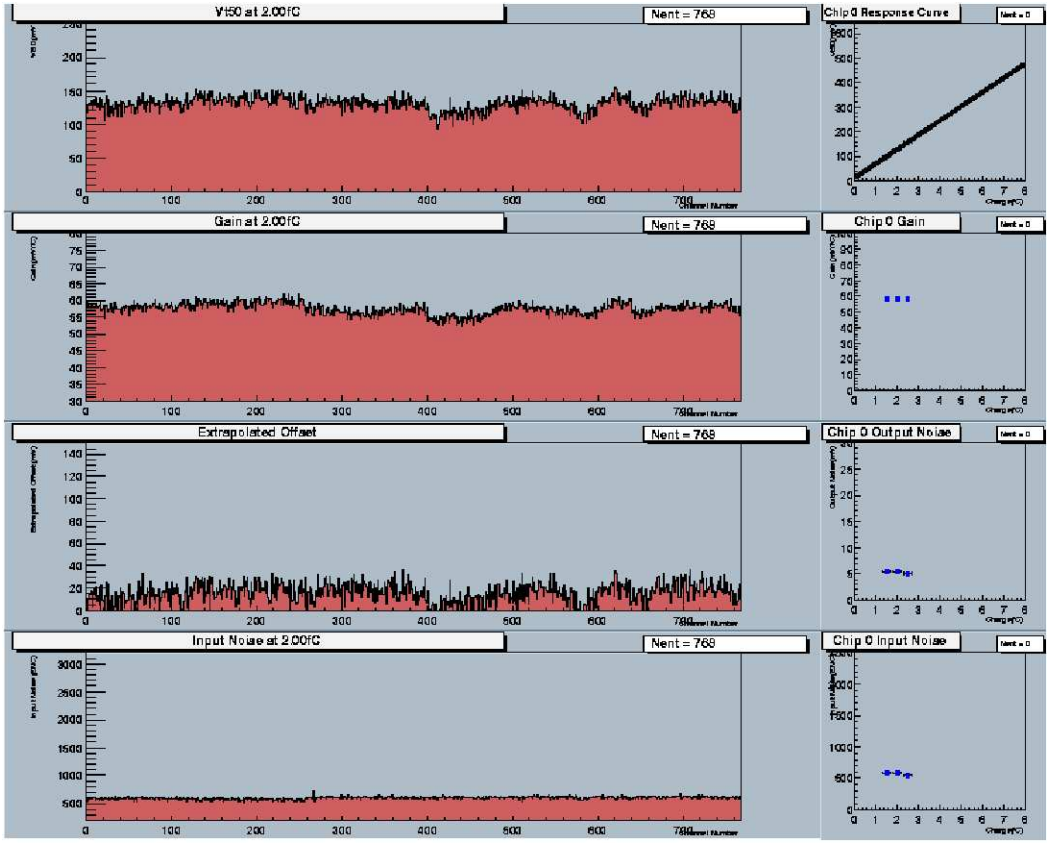

Figure 3.9: Typical plots from a hybrids three point gain. Plots on the left hand side show Vt50, gain, offset and calculated input noise for each channel on the hybrid. Plots on the right hand side show chip averaged values for these quantities as a function of injected charge. The plots are before trimming and the channel to channel variation in the discriminator offset may be seen (left hand side, second from bottom plot). This variation then produces a correlated structure in the Vt50 threshold (top plot).

of increased noise, as shown in figure 3.11. However, this noise can be almost entirely removed by setting the strobe delay fraction to 40%. There does not appear to be any significant change in chip performance as a result of this change.

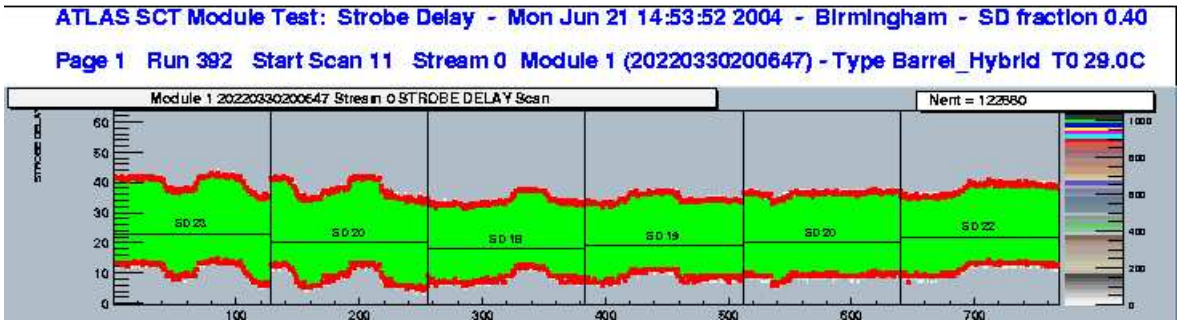

Figure 3.10: Strobe delay scan vs channel number: variation in the working region of the strobe delay. By increasing the strobe delay fraction from 25% to the 40% shown here, all channels can be shown to perform well. The printed values are each chip's strobe delay expressed in strobe delay units; in all cases this is 40% into the working region (shaded).

TrimRange Scan

As detailed in section 3.3.2, trimming is necessary to correct the channel to channel variation in the discriminator offsets. Since this spread is expected to get worse as the detectors accumulate radiation damage, it is therefore necessary to check the initial TrimDAC characteristics, confirming that these are both linear and uniform. The TrimRange scan, plots the TrimDAC setting needed to obtain the Vt50 point of each channel, as a function of threshold . This is done with an injected test charge of 1.0 fC, for each of the four TrimRanges; see figure 3.12, left hand plot. Although not necessary in the actual experiment, the current SCTDAQ software [35] requires each of the channels on a particular hybrid to have their Vt50 points set to the same threshold. Since the variation in channel offsets may be large, it is sometimes not possible to reach this Vt50 point on certain TrimRanges within this fixed threshold.

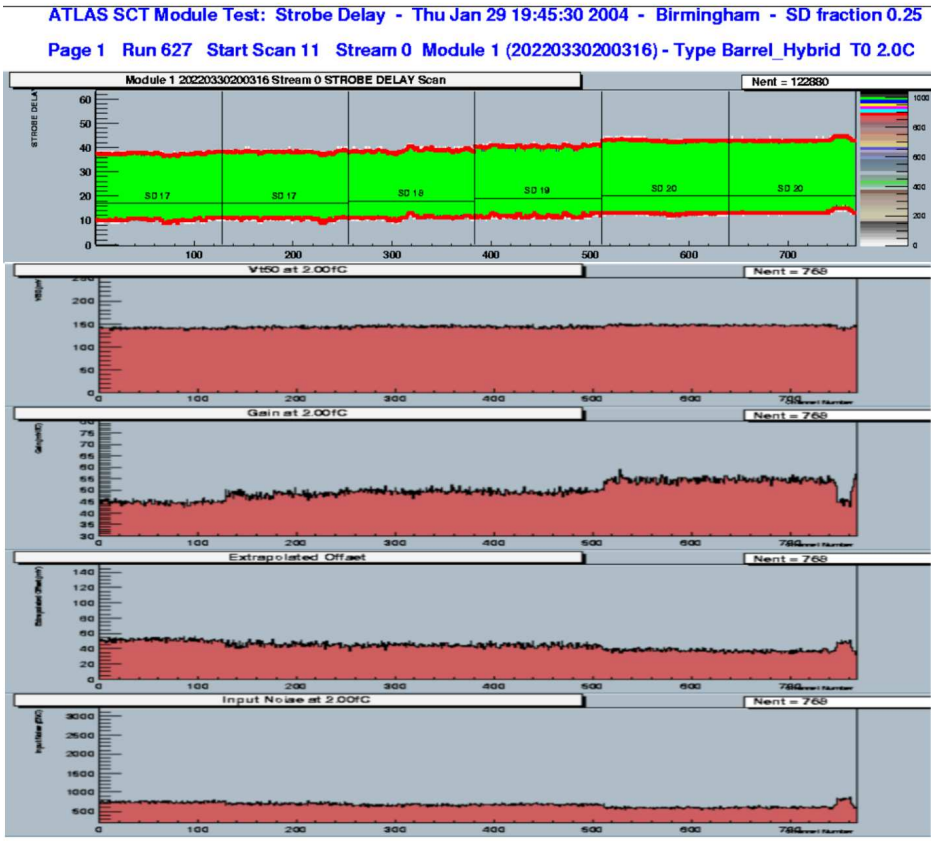

Figure 3.11: Variation of the strobe delay region around channel 750 (far right). Shown is each channel's strobe delay scan (top plot), Vt50, gain, offset and calculated input noise (bottom plot). With the strobe delay fraction set to 25% (black horizontal lines in the top plot) interference effects can be seen leading to a region of high noise (bottom plot). These effects can be removed by setting the strobe delay fraction to 40%.

The number of channels able to adjust their trim sufficiently to obtain their Vt50 point is shown in figure 3.12, right hand plot.

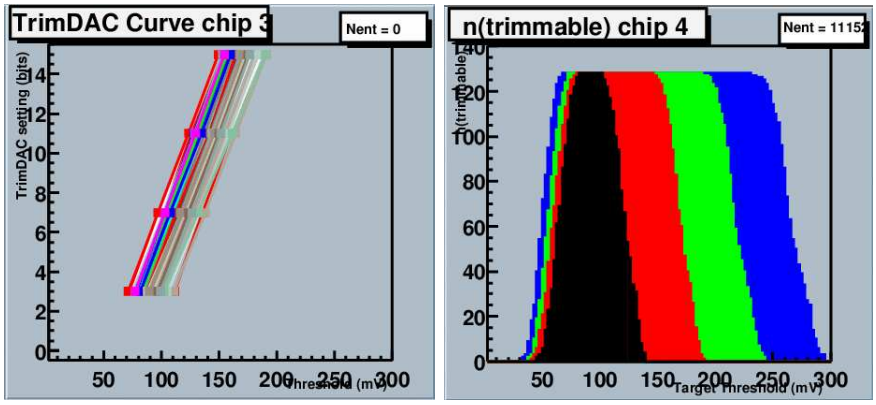

Figure 3.12: On the left, a TrimDAC curve for TrimRange 1. Plotted, for each channel, is the threshold needed to obtain a channel's Vt50 point for four different TrimDAC settings. On the right, the number of channels that can be trimmed at a particular threshold. The narrowest plateau is for TrimRange 0, with the distributions broadening as the range is increased.

Response Curve

This test is similar to a three-point gain; however, it is performed for a larger number of injected charges and done after the channels have been trimmed. Charges injected are 0.5, 0.75, 1.0, 1.25, 1.5, 2.0, 3.0, 4.0, 6.0 and 8.0 fC. Similar plots to the three-point gain are made and due to the large spread in charges used, the non-linearity of the Vt50 and gain can be seen, figure 3.13.

Certain chips display a large spread in their gain characteristics, as shown in the top plot of figure 3.14. This behaviour appears most noticeable when the chips are cold, but is not exclusive to this temperature. Although the exact nature of this feature is not well understood it is suspected that it is indicative of faulty amplification circuitry. The vast majority of such chips can be recovered by reducing the shaper current from 30 to 20 μA. The only effect of such a change, is to reduce

the gain on the affected chip, as shown in the bottom plot of figure 3.14. Since this can be compensated for during the trimming process, the chip is fully able to meet all the acceptance criteria.

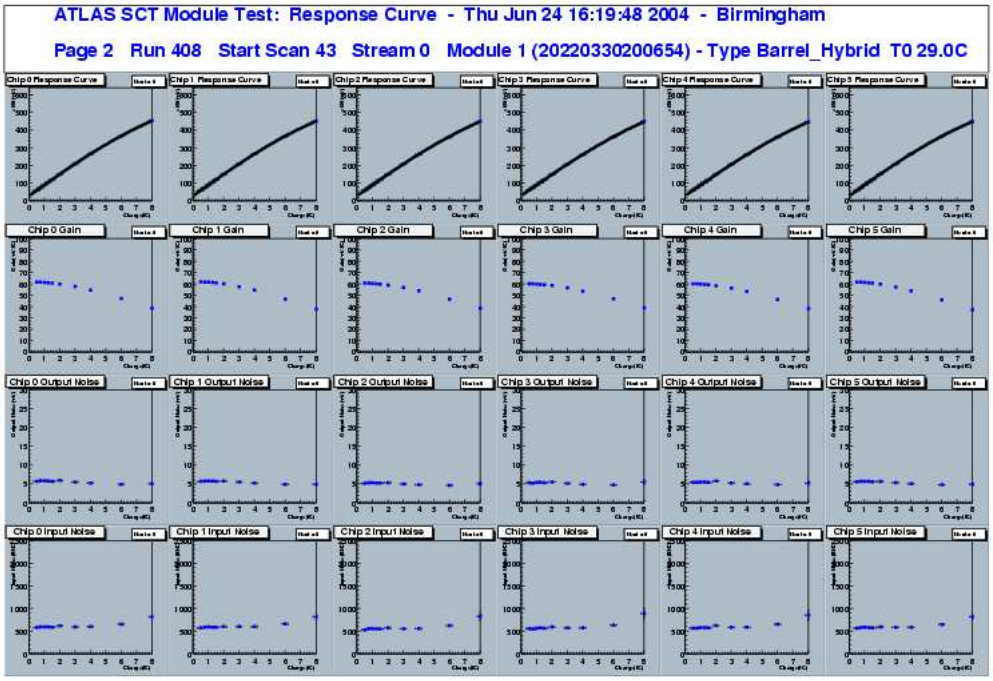

Figure 3.13: Response curves for 6 chips over 10 values of injected charge. The four lines of plots, shows each chip's Vt50, gain, output noise and input noise as a function of injected charge.

Noise Occupancy

This provides a direct measure of the noise present in a channel. No charge is injected for this test and, with the channels trimmed to 1 fC, the threshold is increased from 75 mV below to 75 mV above the 1 fC point. Thresholds well below the 1.0 fC level return occupancies of 1, with the channel recording the background noise. As the threshold increases the number of noise hits reduces and to compensate the number

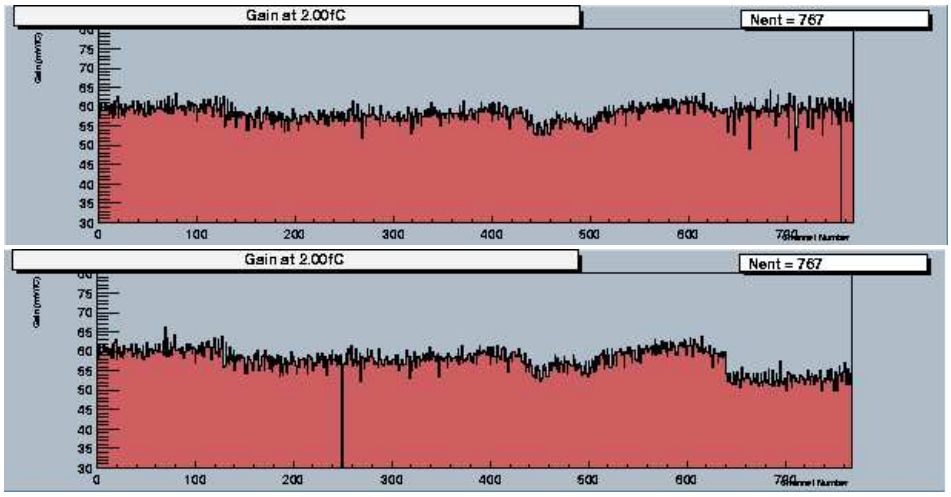

Figure 3.14: A Large gain spread chip: top plot shows chips with a shaper current of 30 μA; the spread in the gain on the end chip can clearly be seen, far right (channels 639 - 767). The bottom plot shows the same chip with the shaper current set to 20 μA leading to a systematically lower gain. Since this can be corrected by the trimming process the chip is deemed to operate satisfactorily.

of triggers sent is increased from 2000 to 10^6.

Equation 3.3 may be approximated in the limit $q_{thr} \ll q_{rnd}$ to;

$$ln(Occupancy) \approx -\frac{1}{2}\frac{q_{thr}^2}{q_{rnd}^2} \tag{3.4}$$

This then provides a complementary method to the three point gain for measuring a channel's noise. Figure 3.15, left hand plot, shows noise measurements for one side of a hybrid as a function of threshold; the right hand plot shows the fit described above for one particular chip.

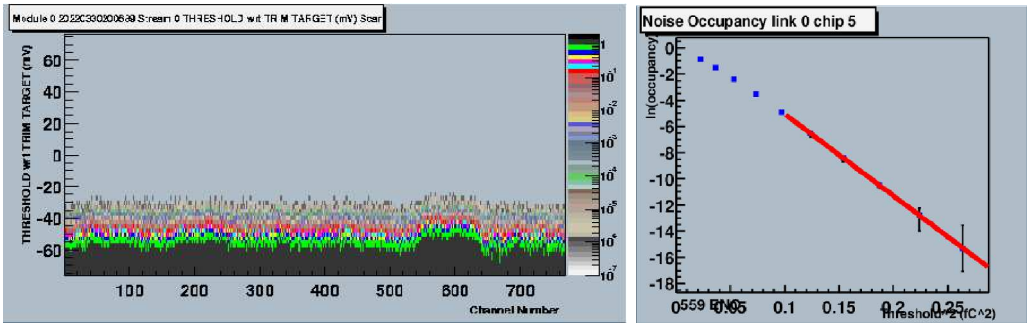

Figure 3.15: Noise Occupancy plots : on the left a plot of the occupancy variation for each channel against relative threshold. The plot shows six chips (768 channels) on one side of the hybrid with the occupancy for each threshold value indicated by colour. A single chip's log occupancy is plotted against (relative threshold)^2 (on the right). The plot shows a linear dependence as outlined by equation 3.4. The average channel (q_{rnd}) noise can be calculated from this slope.

Timewalk

A series of strobe delay scans are performed with the threshold set to 1 fC. Test charges of between 1.25 to 10.0 fC are injected and a fit made to the rising and falling edges, determining the two possible values of the strobe delay such that the Vt50 point is obtained. The time between these two is the region where the chip will function, and this distance (or time) is called the timewalk, as shown in figure 3.16.

3.6 Test Results

3.6.1 Summary of Production Statistics

At the Birmingham hybrid assembly site a total of 730 hybrids were fitted with the ABCD3TA chip. Of these 715 were tested satisfactorily, 12 were returned to Japan for further rework and 3 were deemed damaged beyond reasonable repair.

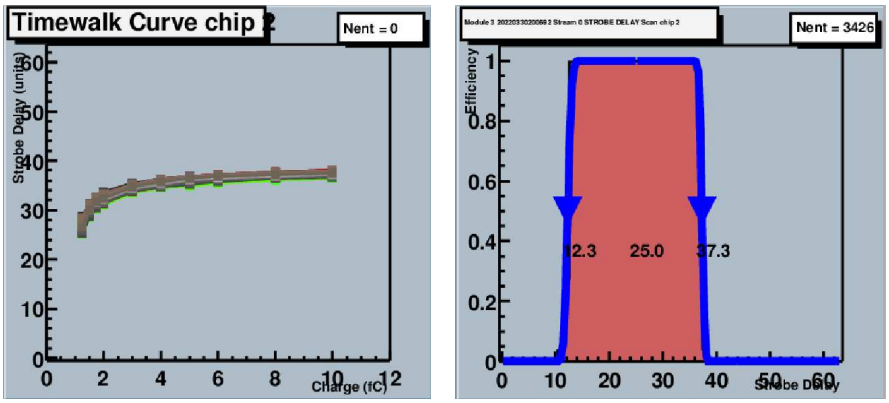

Figure 3.16: On the left the change in the falling edge of the timewalk as a function of charge is shown. The chip average timewalk plot for an injected charge of 10.0 fC can be seen right.

Design specifications state that in an operating module > 98% of channels should be functional [29]; a single bad channel represents 0.065% of the channels on a module and as such 30 bad channels would theoretically be acceptable. The average number of bad channels per hybrid, after assembly and testing at Birmingham, was 1.9 (0.12%). Within this, however, are two classes of hybrids; those with 12 'perfect' chips (624) and those that used 12 class 'AA1' chips (106). Due to the limited production of the ABCD3TA chip, it was necessary to use chips that during wafer testing were identified as having a single potentially bad channel. These chips were grouped on separate hybrids and will be used on barrel 4, the outermost barrel. Since the radiation fluence will be least on barrel 4, it is expected that these hybrids / modules will develop fewer additional bad channels and hence continue to meet the design specification.

A number of hybrids required some element of rework after their initial build either due to the failure of a chip at the electric test stage or a mechanical problem such as bond damage. An analysis of the 123 hybrids that needed rework is given in table 3.3. Explanations for a selection of the most significant electrical rework categories are given below.

Category	Total
Abnormal calibration line	24
S-curve discontinuity	13
Negative discriminator offset	9
Strobe delay failure	6
TrimDAC loading failure	6
Dead chip	6
Full bypass failure	5
Block low gain	5
Miscellaneous	5
Noisy chip	4
Irrecoverable large gain spread	4
Low gain chip	3
Stuck chip	3
Redundancy failure	2
Mask register failure	1
Total electrical failure	96
Total mechanical failure	27
	123

Table 3.3: Summary of hybrids needing rework.

3.6.2 Description of Principal Faults

Abnormal Calibration Lines

Here one of the four calibration lines has anomalous behaviour, as shown in figure 3.17. The manifestation of this problem is that channels either have high gains or offsets in their noise occupancy s-curves. If charges laid down by the calibration line increase proportionally more than expected, then since the gain is calculated from the slope of the response curve, such a line will show a high gain. The converse is also true and would give channels with lower gain than those using other calibration lines. Figure 3.17, top left plot, shows the case of a high gain calibration line; every fourth channel from 383 to 512.

The second class of abnormal calibration lines is caused by an offset in the charge laid down. The gain appears unaffected since the slope of the response curve will stay the same; however, the problem will manifest itself in the s-curve and noise occupancy plots. Although these tests are run with the calibration circuitry turned off, the trimming information used in the tests has been calculated using the defective calibration line. An offset in the calibration lines means that the actual point a set of channels is trimmed to, may be greater than, or less than, the stated 1 fC point. The result will be offsets in the s curves and noise occupancy plots of these channels, (see figure 3.17, bottom left and right plots).

S-curve Discontinuity

This failure is caused by a non-uniform bit in the threshold DAC. As the threshold scan is increased the faulty bit is flipped, but, its actual value is less than the expected uniform increment. The result is that the s-curve has a discontinuity at this value; the threshold is actually reduced by the incremented DAC as shown in figure 3.18. Since it is important for the running experiment to be able to select accurately the threshold, ensuring that noise level can be suppressed, chips displaying

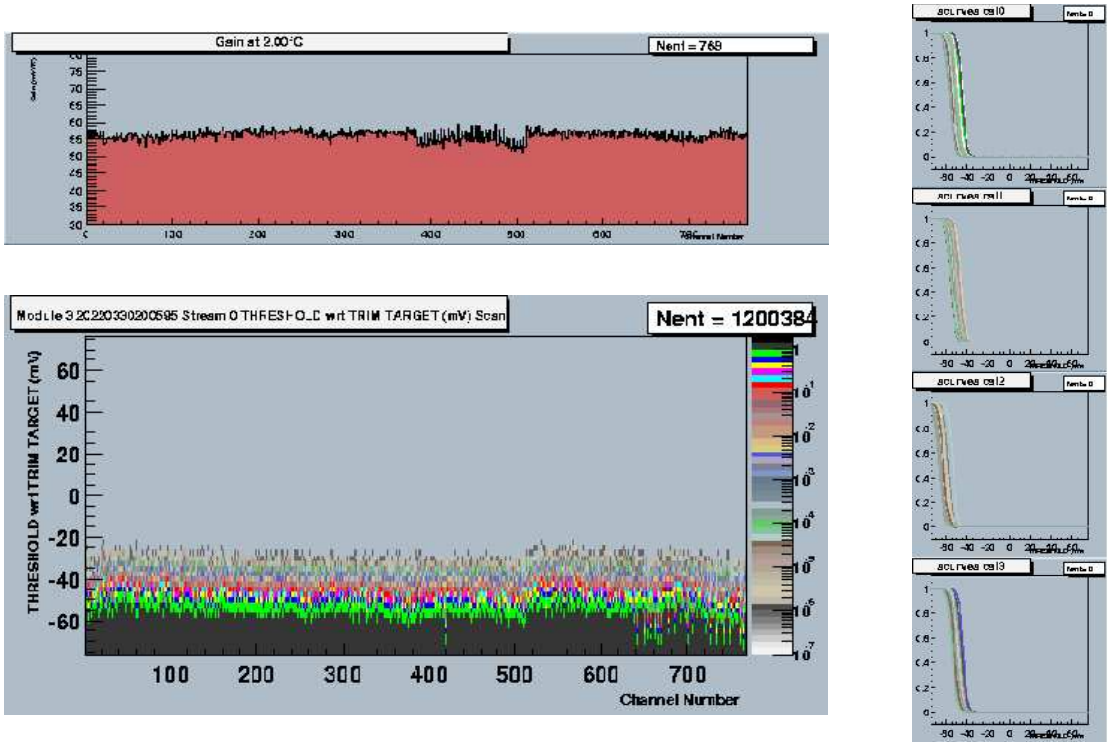

Figure 3.17: The two different types of abnormal calibration line are shown. Top left plot shows each channel's gain, with channels 383 - 511 showing a proportionally higher charge being laid down by a calibration line. Bottom left and right plots show an offset in the calibration setting in the last chip, channels 639-767. The relative offset in the calibration line 2 ('Cal2', right hand plot, third plot down, showing occupancy curves displaced to the left in comparison with the other three plots) leads to high noise in every fourth channel (channels 639-767) in the bottom plot.

such a feature are replaced.

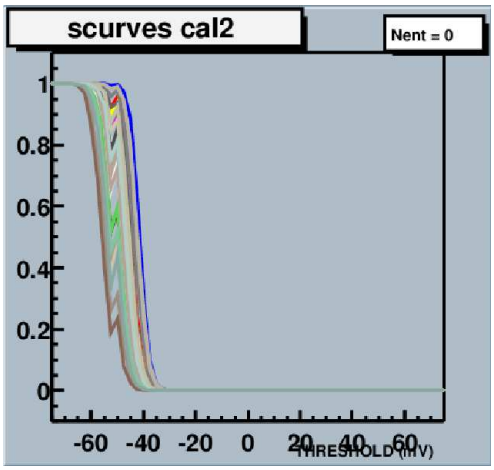

Figure 3.18: Discontinuity in an s-curve: plotted is the average channel occupancy as a function of relative threshold. The cause of the discontinuity is understood to be a non-uniform bit in the threshold DAC. When this bit is activated it actually reduces the threshold creating the jump.

Negative Discriminator Offsets

Negative offset chips show anomalous behaviour in the three point gain scan and noise occupancy plots, as shown in figure 3.19. Whilst the exact cause of the negative offset seen in the three point gain scan is unclear, it is thought to indicate defective discriminator circuitry. Since the byproduct of this behaviour is high recorded noise, as shown in the bottom plot of figure 3.19, chips with this behaviour are rejected and replaced.

Strobe Delay Register Failure

Figure 3.20 shows the failure of the strobe delay register. The most significant bit can be seen quite clearly to fail, with the pattern repeating itself from the mid-point. Since the strobe delay is set to 40% from the rising edge, the failure does not

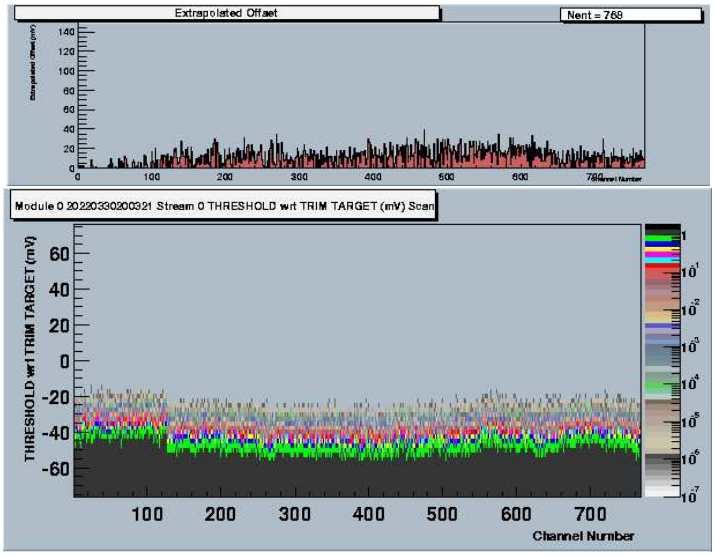

Figure 3.19: Negative offset chips : Top plot, negative offsets (channels 0 to 127) are recorded during the initial three point gain scan. Here channels are untrimmed and the scan calculates a channel's gain and offset. Since this information is then used in subsequent tests, via the trim settings, it leads to further anomalous behaviour. Bottom plot, high levels of noise in the first 128 channels can be seen on the noise occupancy plot.

affect any of the other tests, with the obvious exception of the timewalk. However to ensure the maximum choice of strobe delay settings are available, the chip is replaced.

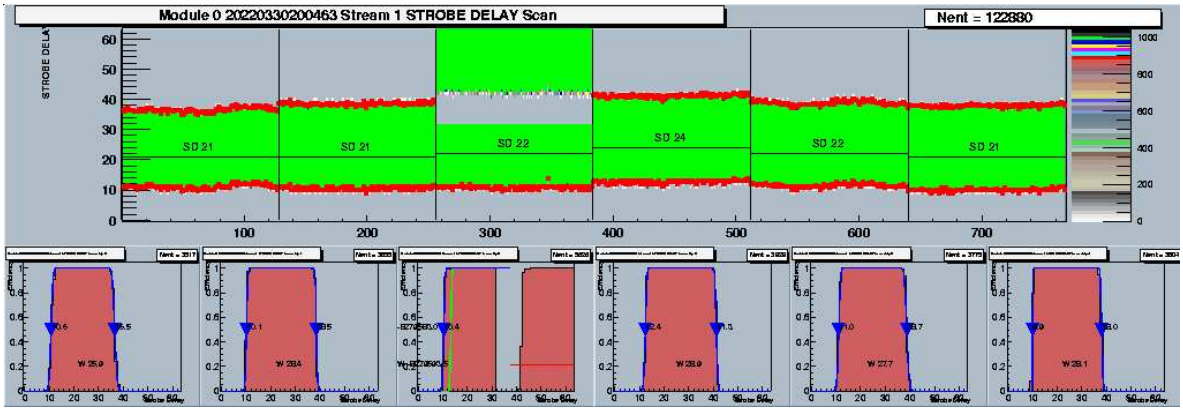

Figure 3.20: Plotted is the strobe delay (top plot) and corresponding timewalk (bottom plot) for six chips. The third chip's strobe delay register can be seen to fail on the most significant bit. Since the bit does not function, the observed pattern is repeated in both the strobe delay and the timewalk.

TrimDAC Loading Failure

On tests not requiring trimming information, these chips appear to function normally. However, once the trimming process is completed and the TrimDAC files loaded, these files appear to become corrupted. Tests reliant on this information therefore produce variable results. Since these files are required to operate efficiently, such chips are replaced. Figure 3.21 shows an example of a chip whose TrimDAC file appears to have become corrupted during the loading process.

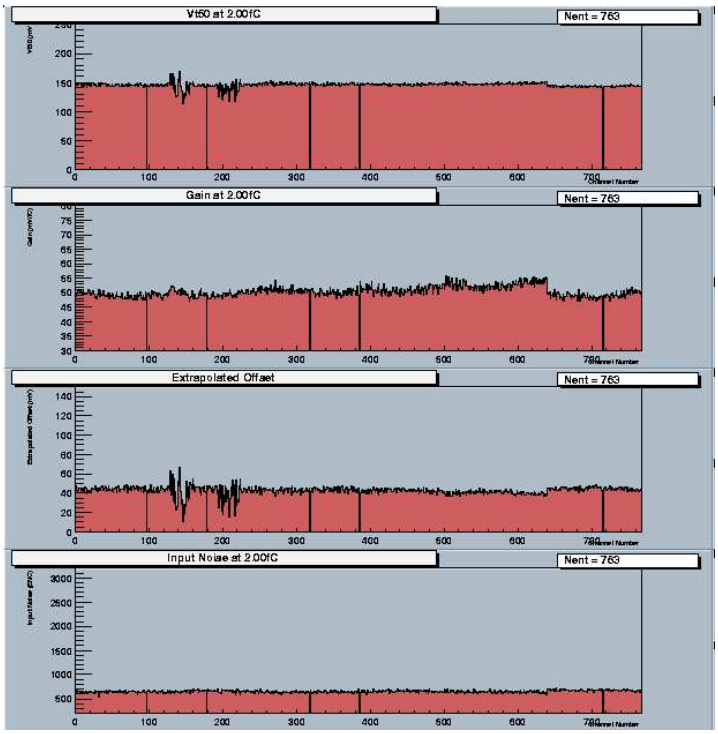

Figure 3.21: Trim DAC loading failure : plotted is the Vt50, gain, offset and calculated input noise for each channel after trimming. Channels 129-255 show a chip that has failed to load its TrimDAC correctly. The vertical lines shown around channels 100, 320, 380 and 720 are masked channels and are unrelated to the above problem.

3.7 Conclusion

Testing and evaluation of hybrids at Birmingham is now complete. A total of 715 hybrids have been successfully mounted with chips and have passed all electrical tests. These tests are performed at various stages of the hybrid assembly and ensure that completed hybrids operate to the acceptance criteria. Of this total, 123 hybrids required some form of rework and have subsequently been accepted. The number of bad channels per hybrid has been kept to just over 0.5 for perfect chip hybrids and 10.3 for 12xAA1 chip hybrids. Both rates are well within design specifications.

Completed hybrids have now been successfully mounted with sensors and placed on the SCT barrels. Within the last few weeks the completed Inner Detector, including the SCT, has been lowered into the ATLAS cavern and is at the time of writing preparing to start its operational life.

Chapter 4

Direct Photon Physics

4.1 Introduction

Direct photons, sometimes referred to as prompt photons, are those photons that are produced in the primary parton-parton interaction. They specifically exclude photons produced from secondary particle decays. There are three main areas of interest surrounding the production of such particles. Firstly their production and associated measurement provides a direct test of perturbative quantum chromodynamics (pQCD). Secondly the link to the interacting partons provided by the photon allows the parton content of the proton to be probed directly. In particular since the dominant contribution to the cross section comes from gluon-quark interactions, measurement of direct photons provides a possible constraint on the relatively ill defined gluon content of the proton [36, 37]. Finally the topology of the process enables the hadronic calorimeter to be calibrated with the electromagnetic calorimeter using energy balance in the event. Since high E_T jets form part of the experimental signature for many "beyond the standard model" processes, this calibration of the hadronic calorimeter into the high E_T region is of great practical value.

The production of photons in hadron colliders comes from two principal sources.

Ignoring photons produced as decay products of intermediate mass states they are either produced directly in the parton-parton interaction (direct photons) or through the fragmentation of a final state quark or gluon. In this chapter these two production mechanisms are discussed along with an introduction to direct photon theory. An overview of previous experimental results is presented before a brief summary and outlook for direct photons at the LHC.

4.2 Direct Photon Production Mechanisms

4.2.1 The Compton and Annihilation Processes

At the leading order (LO) only the Compton and Annihilation processes shown in figures 4.1 and 4.2 contribute to direct photon production. Of these two the dominant one at all LHC energies will be gluon Compton scattering, accounting for $\approx$ 80-90 % of the observed signal. It is through this process that the cross section is sensitive to the gluon content of the proton. The LO cross sections for the two processes can be seen in figure 4.3. The relative importance of the Annihilation process can be seen to increase with P_T. However, due to the pp nature of the initial states at the LHC, the Compton process remains dominant at all values of P_T. This is not the case in $p\bar{p}$ colliders such as the Tevatron where the annihilation contribution continues to grow and dominates the Compton process at $p_T \gtrsim 150$ GeV. The LHC should therefore not only provide superior statistics to other experiments, but also should allow the gluon content of the proton to be probed in regions never before achieved in collider experiments.

The characteristic signal from direct photons is the observance of a well isolated photon recoiling against a jet. At the leading order these events should be back to back in the ϕ plane and display a balance of energy between the jet and the photon. The inclusion of higher order effects will partly spoil these characteristics through the emission of initial or final state radiation and the appearance of multiple jets in

the final state. Figure 4.4 show examples of these higher order contributions to the direct process. Such diagrams consist of the emission of a quark or gluon from one of the initial or final state legs, or through virtual loops whereby a gluon is emitted and then shortly reabsorbed. Due to the dominance of the gluon at values $x \lesssim 10^{-1}$ (as shown in figure 1.4) many LHC collisions will be between two gluons with one or more of these gluons undergoing initial state radiation to form the gq or $q\bar{q}$ state described above.

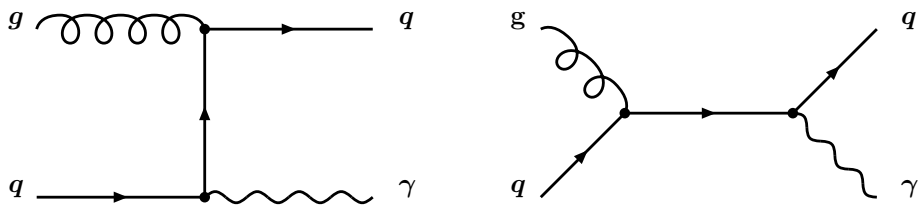

Figure 4.1: Direct photon Compton subprocess.

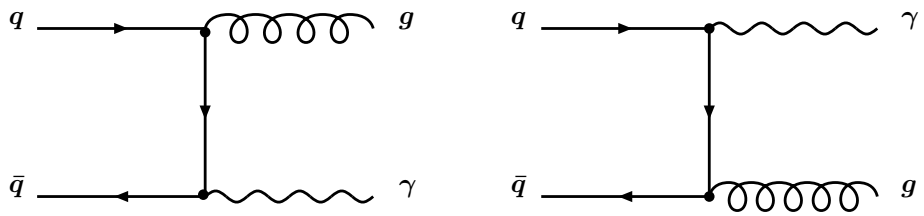

Figure 4.2: Direct photon Annihilation subprocess.

4.2.2 The Bremsstrahlung Process

In addition to the direct production mechanisms, photons can also be produced through the bremsstrahlung diagrams show in figure 4.5. These photons are no longer created in the hard scatter but instead through the fragmentation of a final

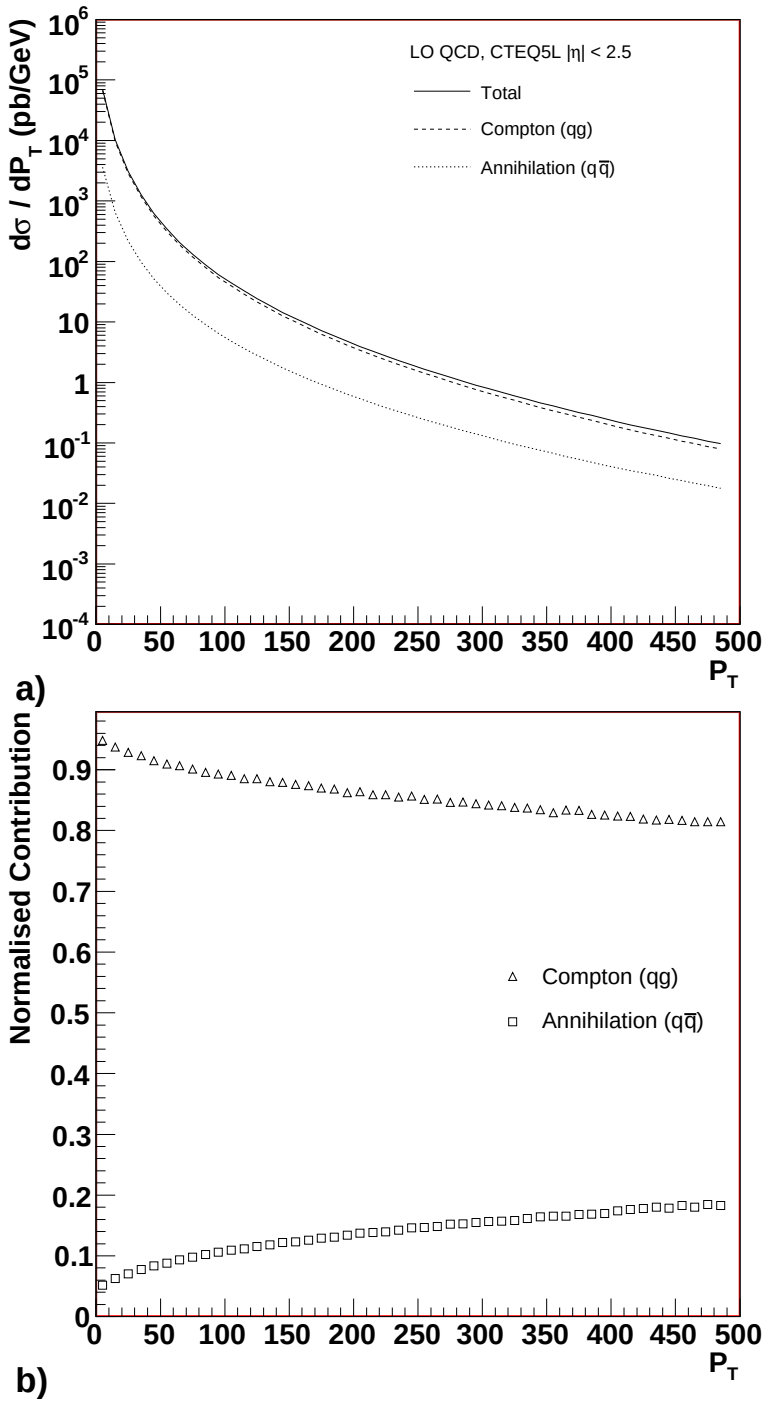

Figure 4.3: a) LO Cross section for the production of inclusive direct photons at the LHC. The plot was generated with Pythia 6.228 in the kinematic regime $|\eta| > 2.5$ b) The relative contributions of the two LO processes to the inclusive photon cross section. The two subprocesses have been normalised to the total LO cross section.

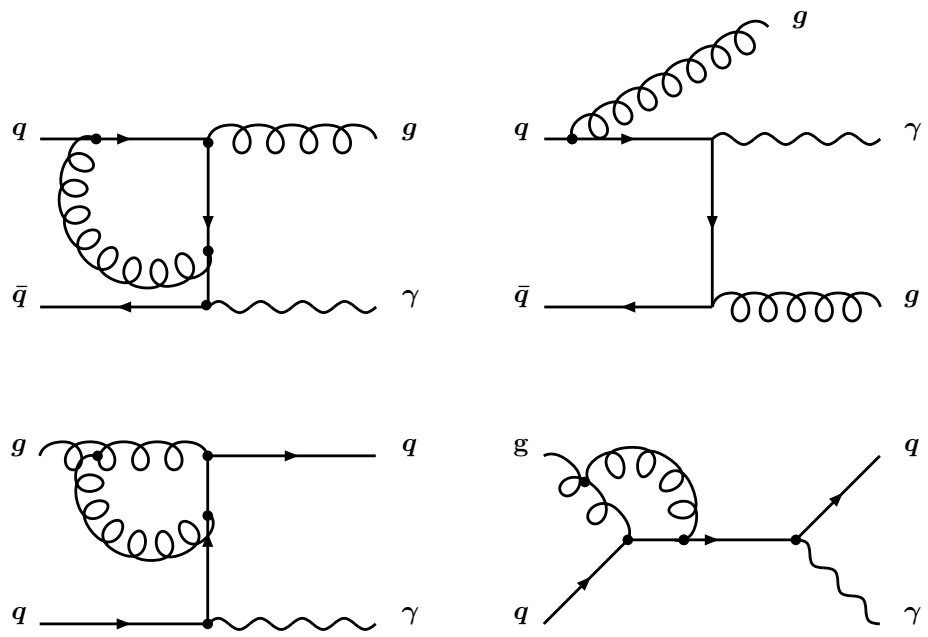

Figure 4.4: Some examples of higher order Feynman diagrams

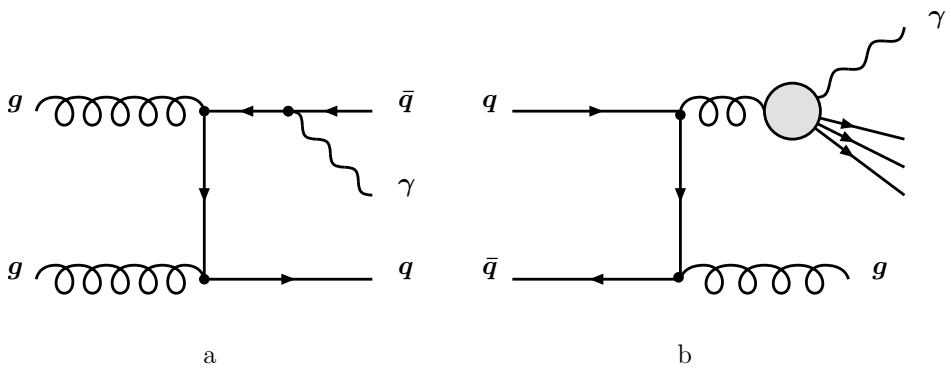

Figure 4.5: Bremsstrahlung diagrams

state parton. Fragmentation functions D_q^γ and D_g^γ are used to describe this process; however, two alternative methods exist for the calculation and implementation of these functions. In both schemes the bremsstrahlung process is split into a perturbative and a non-perturbative part at some fragmentation scale, μ_F. In the first scheme, as outlined in [38] and implemented in the JETPHOX [39,40] Monte Carlo, the perturbative part (such as figure 4.5(a)) is calculated up to the desired order with contributions containing μ_F being resummed. This resummation introduces a dependence on the factorisation scale. Photons produced during the soft QCD hadronisation (such as figure 4.5(b)) are then described using the vector meson dominance (VMD) model [41]. Here the fragmentation of a quark or gluon is described via its fragmentation firstly into a linear combination of vector mesons which then turn into photons. Under the second scheme as outlined in [42,43] the calculation of the perturbative part is not resummed and the calculation is performed to a fixed order in μ_F. The non-perturbative part is obtained through a fit to LEP data. Since the perturbative calculations are not resummed, there exist cancellations of terms involving μ_F factors and therefore, under this scheme, the calculations are not μ_F dependent.

Bremsstrahlung photons can provide a significant source of isolated photons. Clearly where the emission of a photon occurs at a shallow angle, these photons will be associated with the final state quark remnants and may be removed by their failing a suitably chosen isolation cut. However, in instances where photons are radiated at large angles the isolation cuts will not remove such events. These events must therefore be included in the cross-section calculation and somewhat spoil the simplicity of the direct photon theory. A naive expectation of the rate of such events might be $\mathrm{O}(\alpha\alpha_s^2)$, since two strong and one electromagnetic vertices are involved in these processes. If this were the case then they should contribute little to the overall observed signal. However, as shown in [44,45] the bremsstrahlung component in fact scales as $\mathrm{O}(\alpha\alpha_s)$ and is therefore of the same order as the two LO processes. This then leads to the expectation that the cross section for fragmentation, in the absence of isolation, will be similar to that for the direct processes [46].

4.3 Direct Photon Theory

The kinematics of direct photons can be shown by considering the two body scatter of figure 4.6. Using the ATLAS coordinate system, as set out in section 2.4, the initial and final state partons may be written as four momenta (E, P_x, P_y, P_z)

$$p_a = \frac{\sqrt{s}}{2}(x_a, 0, 0, x_a) \tag{4.1}$$

$$p_b = \frac{\sqrt{s}}{2}(x_b, 0, 0, -x_b) \tag{4.2}$$

$$p_c = p_T(cosh(\eta_c), cos(\phi), sin(\phi), sinh(\eta_c)) \tag{4.3}$$

$$p_d = p_T(cosh(\eta_d), -cos(\phi), -sin(\phi), sinh(\eta_d)) \tag{4.4}$$

where x_a and x_b are the fractions of the initial state hadron momentum carried by each initial parton and p_T, ϕ, η_c and η_d are the transverse momentum, azimuthal angle and pseudorapidity of the scattered particles. Conserving energy and longitudinal momentum gives,

$$x_a = \frac{x_T}{2}(e^{\eta_c} + e^{\eta_d}) \tag{4.5}$$

$$x_b = \frac{x_T}{2}(e^{-\eta_c} + e^{-\eta_d}) \tag{4.6}$$

where $x_T = 2p_T/\sqrt{s}$ is the transverse momentum fraction probed by the process. Equations 4.5 and 4.6 relate the struck parton's momentum fraction to the kinematic observables p_T, η_c and η_d. Given these quantities, it is then possible to calculate the momentum fraction of both interacting partons. Since we have assumed these partons possess no transverse momentum, the scattered photon and jet should be back-to-back in the $R - \phi$ plane. Furthermore, if the initial partons have nearly equal momentum then the γ-jet system will also be scattered back-to-back in the η plane. Hence at $\eta = 0$, $x_T = x_a = x_b$ and the measured transverse momentum of the photon (or jet) is directly linked to the momentum fraction of the interacting

gluon and quark. If the gluon and quark possess non equal momentum, the system will be thrown in the direction of the highest momentum parton with the jet and photon both appearing in the same side of detector. Due to the relative densities of the quark and gluon distributions, the majority of events will involve a high x quark and a low x gluon. The effect of this is that the γ-jet system is boosted in the direction of the incoming quark. If an inclusive direct photon measurement is made, that is only the photon is measured, then a minimum x (x_{min}) involved in the scatter may be calculated. The only constraint on the unobserved jet is that in the overall scatter $x_{max} \leq 1$. This then leads to

$$x_{min} = \frac{x_T e^{-\eta}}{2 - x_T e^{\eta}} \tag{4.7}$$

The implications of this are discussed more fully in chapter 7, but x_{min} is the minimum momentum fraction probed in the interaction, and is most likely the x value of the gluon. It will be at its smallest value at low p_T and high η and in this region the LHC will be sensitive to the gluon fraction in the range of $10^{-4} - 10^{-3}$. In the other extreme case, at high energies both partons will have large x values, and will probe distributions in the high x range. Since in this range ($\approx 10^{-1}$) the gluon is relatively unconstrained, direct photons will offer a valuable probe of this high x behaviour.

4.3.1 pQCD Scattering

As seen in chapter 1.3.3 proton-proton scattering is described by pQCD. Restating equation 1.3 the advantages of using direct photons as a test of pQCD can be seen.

$$E_C \frac{d\sigma^3}{d^3 p_C}(AB \to C + X) =$$
$$\sum_{abcd} \int dx_a dx_b dz_c f_A^a(x_a, \mu_F) f_B^b(x_b, \mu_F) D_c^C(z_c, M) \frac{\hat{s}}{z_c^2 \pi} \frac{d\sigma(\mu_R, \mu_F)}{d\hat{t}}(ab \to cd) \delta(\hat{s}+\hat{t}+\hat{u})$$

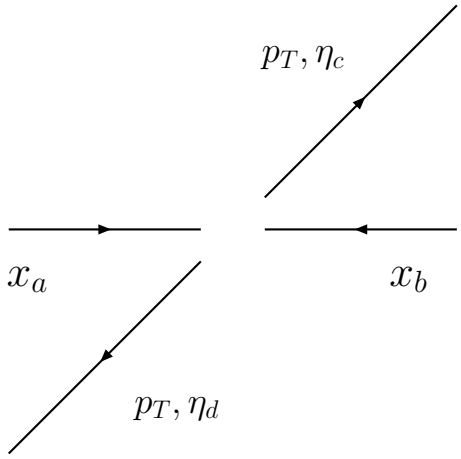

Figure 4.6: Generic 2 body scattering.

In the case where a quark or gluon emerges from the hard-scatter (i.e. a non direct photon) the parton undergoes the poorly understood process of hadronisation. The link between the experimentally observed final state and the parton level is obscured not only with these theoretical uncertainties but also with the experimental difficulties associated with jet definition and measurement. Direct photons on the other hand suffer none of these effects and in the absence of the fragmentation function $D_c^C(z_c)$ the direct link to the parton-parton interaction provides a clean probe to the dynamics of the hard scatter.

The cross section obtained is the incoherent sum of all contributing processes weighted by their parton distributions and any appropriate fragmentation functions. In the case of direct photons there are only two contributing processes, the Compton and Annihilation processes compared to 8 for $2 \rightarrow 2$ jet production. This relatively low number of initial and final states simplifies the theoretical calculations and the presence of the electromagnetic vertex in the photon diagrams ensures the higher order corrections in pQCD are more reliable. Comparing the leading order Compton and Annihilation contributions with the dominant processes for the $2 \rightarrow 2$ jet cross section (equations 4.8 - 4.10 below) it is possible to form an expectation for the magnitude of these competing processes.

$$gq \to \gamma q \ : \quad -\frac{\pi\alpha\alpha_s e_q^2}{3\hat{s}^2}\left[\frac{\hat{t}}{\hat{s}}+\frac{\hat{s}}{\hat{t}}\right] \tag{4.8}$$

$$q\bar{q} \to \gamma g \ : \quad \frac{8\pi\alpha\alpha_s e_q^2}{9\hat{s}^2}\left[\frac{\hat{u}}{\hat{t}}+\frac{\hat{t}}{\hat{u}}\right] \tag{4.9}$$

$$gg \to gg \ : \quad \frac{9\pi\alpha_s^2}{2\hat{s}^2}\left[3-\frac{\hat{t}\hat{u}}{\hat{s}^2}+\frac{\hat{s}\hat{t}}{\hat{u}^2}+\frac{\hat{s}\hat{u}}{\hat{t}^2}\right] \tag{4.10}$$

In the central region ($\eta \approx 0$) the Mandelstam variables $\hat{s}$, $\hat{t}$ and $\hat{u}$ are such that $\hat{s}/2 = -\hat{t} = -\hat{u}$. The ratio of the Compton and Annihilation processes will be simply the ratio of the gluon and antiquark distributions together with the factors present in equations 4.8 and 4.9. It is therefore expected that for $Q = 100$ GeV the Compton processes will be around an order of magnitude larger than the Annihilation. Similarly, it is possible to compare the rates for the Compton and the $gg \to gg$ process. For LHC energies α_s is approximately 17 times larger than α and will significantly increase the rate of gg scattering. Quark charges together with the terms in equations 4.8 and 4.10 add another factor 10 and the relative parton densities of the quark and gluon contribute a further factor 5 to the cross section. This then leads to the expectation that the jet rate will be about three orders of magnitude larger than that for direct photons.

The experimental apparatus must therefore provide good photon identification to extract this signal from this large background. Additionally, it will be important that the contribution from any remaining background be calculable, preferably from experimentally observed quantities. There are, however, many experimental advantages that favour the use of photons. As discussed above their observation is not governed by the problematic hadronisation process and they have the associated advantage that they will be measured in the electromagnetic calorimeter. This offers improved energy and spatial resolution and should in part compensate for the lower cross section.

In the above description the interacting partons have been assumed to be collinear with the colliding hadrons. The partons therefore possess no transverse momentum (k_T) before collision. That this assumption is problematic can be seen by considering the fact that the partons are bound objects inside the nucleus. According to the uncertainty principle this confinement should result in the acquisition of some k_T and is naively estimated to be ≈ 0.3 GeV. As we shall shortly see, the size and nature of this k_T has been the source of some controversy in the interpretation of direct photon data.

4.4 Previous Experiments

Many experiments have in the past made direct photon measurements. These can be divided into fixed target and collider experiments as shown in table 4.1. Fixed target experiments have traditionally provided data in the x range from 0.1 to 0.6. Indeed, data from WA70 and UA6 have been used in some parton distribution fits [47, 48]. However, inconsistencies between direct photon theory and the more recent fixed target experiment carried out at the Tevatron (E706), together with the large theoretical uncertainties present, have meant that such data are now no longer included in the most standard fits. The high x gluon content is instead constrained using the high E_T jet data provided by CDF and D0 and momentum sum constraints from DIS data.

The first hadron collider to measure direct photons was the CERN ISR with the R806 experiment. Together with the UA1 and UA2 experiments at the $Sp\bar{p}S$ they probed the gluon in the region $0.05 < x < 0.3$. These early data gave quantitative agreement with NLO theory and it was not until the high statistics of the Tevatron experiments, with their increased measurement precision, that problems started to appear. The Tevatron's $p\bar{p}$ collider and the D0 and CDF experiments measured the gluon content down to 0.01 whilst its fixed target experiment (E706) made measurements in the region $0.1 < x < 0.7$. Data from these and other direct photon

measurements are plotted in figure 4.7, being taken from [49]. The interpretation of these data and the completeness of current direct photon theory has been the subject of much debate over the past ten years [38,47,50–52]. The data in figure 4.7 appears to show a large discrepancy with theory; the data showing a steeper dependency on x_T than is suggested by theory. The fact that this is the case for fixed target and the ISR experiments points away from a possible fragmentation effect since these experiments are insensitive to this factor. It has therefore been suggested [49, 51, 53] that this could be due the partons possessing a small amount of transverse momentum (k_T) before colliding. In this case, the uniform smearing of the centre-of-mass energy by such a k_T could account for the observed cross sections due to its steep slope as a function of p_T. Such an effect would then be more pronounced at the low end of the p_T spectrum than at the high, as indeed is born out by the data. Huston et. al. [51] showed that by convoluting the cross section with a Gaussian function of transverse momentum they could reproduce the observed data for both fixed target and collider experiments. Moreover, the amount of k_T required to reproduce the data, $\approx 1-2$ GeV for fixed target and $\approx 2-4$ GeV for collider experiments, is consistent with that inferred from dimuon, diphoton and dijet data [49]. The size of this k_T is over and above that which one would expect from the fact partons are bound inside the proton nucleus. It has therefore been suggested that extra k_T may be given to the system through the radiation of soft gluons before scattering. This initial-state soft-gluon radiation then provides an additional kick to the parton in excess of that expected by current NLO QCD calculations.

The expected effect of additional k_T at the LHC has been discussed in detail elsewhere [37]. However, the results from pairs of dimuons, diphotons and dijets show that the k_T grows approximately logarithmically with $\sqrt{s}$. For the LHC it is anticipated that for mass states of 30-40 GeV the range of k_T should be 6.5-7.0 GeV. At the Tevatron, translating this effect to the observed p_T spectrum of the direct photon, it is seen that the effect falls roughly as $1/p_T^2$. It is therefore not expected to be important past p_T of ≈ 30 GeV at LHC energies [37].

Experiment	Accelerator	Type	Initial State	$\sqrt{s}$	year	ref
R806	ISR	Collider	pp	63 GeV	1982	[54]
WA70	SPS	Fixed Target	pp	23 GeV	1988	[55]
UA1	S$p\bar{p}$S	Collider	$p\bar{p}$	630 GeV	1988	[56]
R110	ISR	Collider	pp	63 GeV	1989	[57]
R807	ISR	Collider	$p\bar{p}$	63 GeV	1990	[58]
UA2	S$p\bar{p}$S	Collider	pp	630 GeV	1991	[59]
UA6	S$p\bar{p}$S	Fixed Target	$p\bar{p}$	24.3 GeV	1988	[60]
UA6	S$p\bar{p}$S	Fixed Target	pp	24.3 GeV	1988	[60]
E706	Tevatron	Fixed Target	pBe	31.6 GeV	1998	[61]
E706	Tevatron	Fixed Target	pBe	38.8 GeV	1998	[61]
D0	Tevatron	Collider	$p\bar{p}$	1800 GeV	2000	[62, 63]
D0	Tevatron	Collider	$p\bar{p}$	630 GeV	2001	[64]
CDF	Tevatron	Collider	$p\bar{p}$	1800 GeV	2001	[66]
CDF	Tevatron	Collider	$p\bar{p}$	630 GeV	2001	[65]

Table 4.1: A list of direct photon experiments. Table taken from [67].

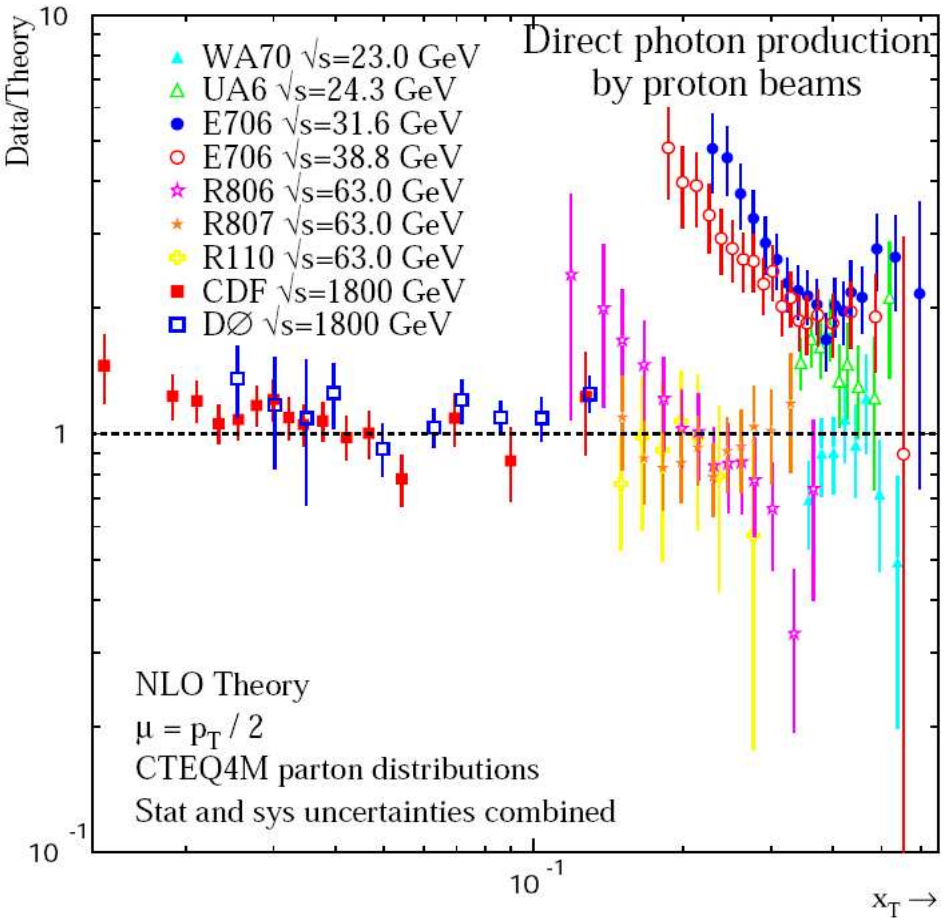

Figure 4.7: Comparison between proton-induced direct-photon data and NLO pQCD calculations. The data are plotted as a function of $x_T = 2p_T / \sqrt{s}$ *to compare data from experiments with differing values of* $\sqrt{s}$*; note the log scale on both axes. This plot was taken from [49].*

It should be noted though that this k_T hypothesis is not universally accepted. Since many of the stated data sets contain large systematic uncertainties it has been argued [52] that by carefully choosing the scales involved a reasonable agreement can be found to all data except that from the R806 and E706 experiments. The measured photon p_T spectra of R806 is 3-6 GeV and the authors of [52] argue it covers a range where pQCD is potentially unreliable. They therefore discount this result and claim the remaining data set, (E706), is inconsistent with both other experiments and the NLO theory. As a result they assert that no significant discrepancy exists. In addition, they also point out that the introduction of k_T smearing has an adverse effect on the agreement of other data sets with NLO theory, notably that obtained in the ISR. The authors show in [38] that good agreement between NLO theory and data is possible over a wide range of data sets without the need for additional k_T. This is reproduced in figure 4.8, showing data over eight orders of magnitude in cross section and two orders of magnitude in energy in agreement with the NLO JETPHOX Monte Carlo program. The clear exception to this is shown by the E706 data, on the bottom left of the figure.

4.5 Conclusion

Direct Photon production has long been seen as an ideal testing ground for pQCD. In addition to this it also offers the potential for further constraining the gluon distribution of the proton. However, the full potential of this process has yet to be realised due to the poor description of the data by pQCD. Whilst progress of the full resummation calculations continues, a convolution of the cross section with a Gaussian k_T smearing function has been developed and appears to improve the agreement with data. This method, however, is not universally accepted and remains a subject of much discussion. Additional data from the Tevatron along with that from the LHC may help to resolve this controversy and together with theoretical refinement provide a framework by which further constraints may be placed upon

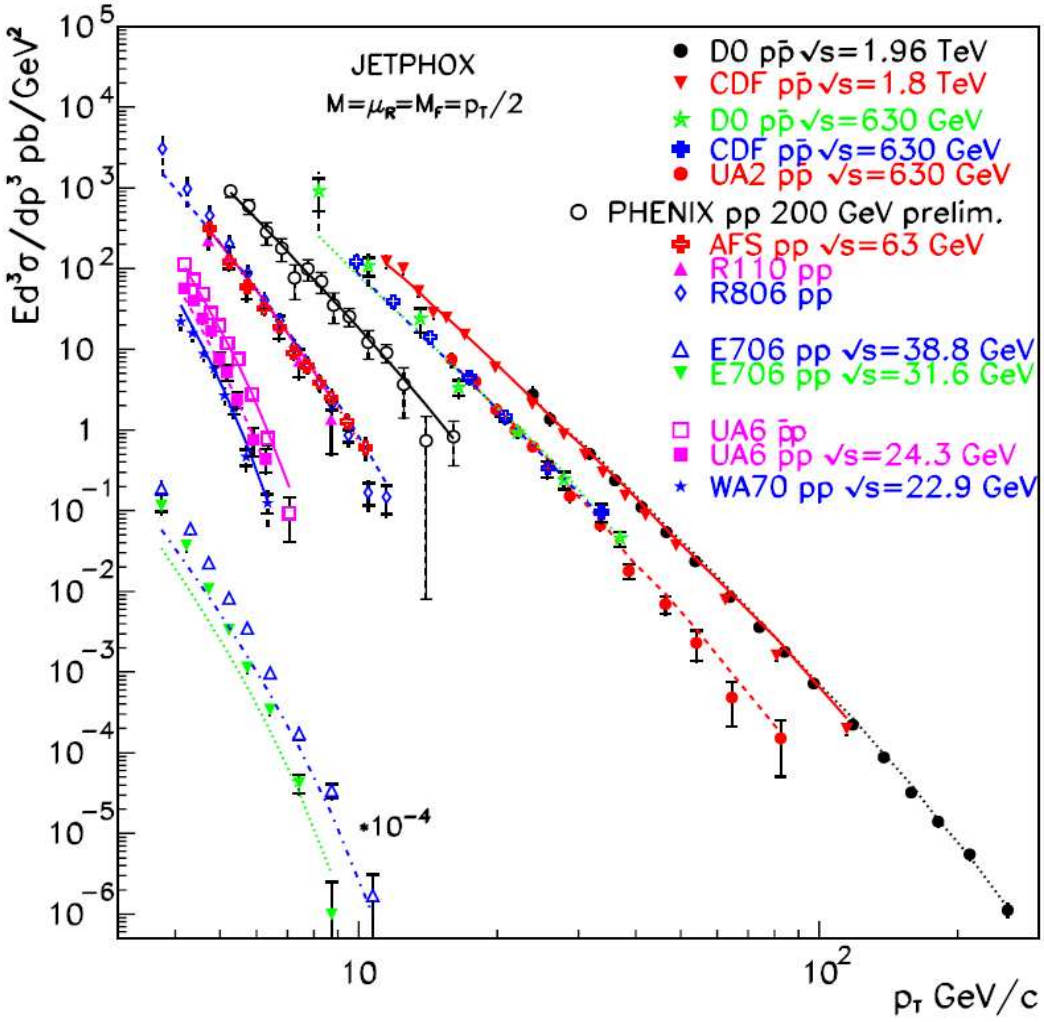

Figure 4.8: World's inclusive and isolated direct photon production cross sections measured in proton-proton and proton-antiproton collisions compared to JETPHOX NLO predictions using BFG II (CTEQ 6M) for fragmentation (structure) functions and a common scale $p_T/2$. For clarity of the figure the E706 data are scaled by a factor 10^{-4}. The plot and caption have been taken from [38].

the gluon distribution.

Chapter 5

Photon Identification

5.1 Introduction

In this chapter photon identification criteria are discussed; particular attention is paid to the identification of photons against the dominant source of background, QCD jets. The chapter outline follows a similar flow to the current ATLAS software reconstruction. Data samples and their production are presented first, followed by the preselection criteria used to obtain the starting sample of photons. Quantities useful in the identification of photons are discussed next and a comparison is made for photons and jets. Since the trigger simulation was not at the time of writing part of the standard simulation chain, potential trigger menus are discussed separately. The results obtained, together with a comparison with previous studies, are presented next before a discussion of the effects of pileup.

5.2 Data Samples

Event generation, simulation and reconstruction were performed within the Athena framework [68], release version 10.0.1. The Light Job Submission Framework (LJSF)

[71] was used to submit events to a network of PC clusters distributed around the world called 'The Grid'. Events were stored in a variety of data centres with analysis being performed on local copies of these files. All simulation samples used the 'Rome' detector layout [69] which was, at the time of production, the expected layout at the start of LHC running. This layout has been recently revised and it is now expected that the second pixel layout will be included at the start of the experiment. Its inclusion will slightly increase the amount of upstream material present in the detector, but it is not expected to have a significant effect on the simulation performance for this study. No pileup effects were included within the production although the effects of pileup are discussed in section 5.11.

In order to study the identification of photons and the rejection of QCD background events a number of data samples were used. Four energy ranges were considered, as summarised in table 5.1. A single particle gun generator was used to produce photons with fixed E_T and a flat η distribution. Background events were generated with Pythia 6.226 [70]; these consist mainly of QCD dijets with some other additional processes, as illustrated in table 5.2. These background process were generated in proportion to their expected cross sections at the LHC and then passed through an event filter.

Sample	E_T used in analysis	dataset	comments
Background	> 20	004814	official Rome production
Single Photon	≈ 20	970200	private production using LJSF
Background	> 60	004815	official Rome production
Single Photon	≈ 60	970600	private production using LJSF
Background	> 130	991300	private production using LJSF
Single Photon	≈ 130	971300	private production using LJSF
Background	> 370	993700	private production using LJSF
Single Photon	≈ 370	973700	private production using LJSF

Table 5.1: Summary of the data sets used.

The purpose of the event filter is to remove, at an early stage, events that are unlikely to be reconstructed as a photon. Since the simulation of a single QCD event can take approximately 30 minutes, the filter greatly reduces the amount of CPU time required. It operates on the generated particles as follows; the E_T sum of all stable Monte Carlo (MC) truth particles inside a sliding window $\Delta\eta \times \Delta\phi = 0.12 \times 0.12$ is calculated. This window is then moved around the region $|\eta| < 2.7$ and events that have an E_T sum greater than some minimum value are accepted. Minimum filter cuts for the four energy ranges considered are shown in table 5.3 together with the parton level cuts used in the generation and the E_T cuts used in the analysis. No such filters were applied to the single photon samples since they would pass with 100% efficiency.

During the subsequent analysis a bug was discovered in the Geant4 simulation. Under certain circumstances low energy photons (order MeV) had their energy erroneously increased by a factor 1000 and the detector response appropriate for such high energetic particles was recorded. The bug was found to be present in all data samples irrespective of production channel, as can be seen in figure 5.1. The transverse energy found in clusters (which form the starting point for the reconstruction of photons) is shown against the energy present in the MC truth for that region. This MC energy was calculated via a cone in $\eta \times \phi$ of size $R = 0.2$ ($R = \sqrt{(\Delta\eta^2 + \Delta\phi^2)}$) drawn around the cluster. All the energy from stable MC particles was summed and groups of events can be seen in both samples that have significant clusters of energy but no corresponding particles in the MC truth. Such events were removed from the following analysis by demanding that at least 80% of the reconstructed photon energy was accounted for by truth particles within a $\Delta R = 0.2$ cone. This requirement has a negligible effect on good events, as will be discussed in section 5.9. The observed rates of candidates passing the preselection criteria but having no basis in the MC truth was found to be 2%, 0.7%, 0.3% and 0.2% for the four energy regions in increasing order. The reduction in rate as energy increases, is due to the energy spectrum present in the source of these events.

Hard Process	Pythia Process	Expected cross-section (mb)
$f_i f_j \to f_i f_j$	11	
$f_i \bar{f}_i \to f_k \bar{f}_k$	12	
$f_i \bar{f}_i \to gg$	13	2.28
$f_i g \to f_i g$	28	
$gg \to f_k \bar{f}_k$	53	
$gg \to gg$	68	
$f_i \bar{f}_1 \to g\gamma$	14	4.17×10^{-4}
$f_i g \to f_i \gamma$	29	
$f_i \bar{f}_i \to Z^\star \gamma^\star$	1	4.53×10^{-4}
$f_i \bar{f}_i \to W^\pm$	2	1.41×10^{-4}
$f_i \bar{f}_i \to t\bar{t}$	81	4.91×10^{-7}
$gg \to t\bar{t}$	82	

Table 5.2: Direct photon signal and background composition as generated by Pythia 6.226. Cross sections shown are for the parton sample $E_T > 15$ GeV. The QCD processes (top left box) dominate in all of the four E_T ranges considered in this analysis, being $\gtrsim 99.9\%$ of the total number of events generated.

Sample	Generated E_T range (GeV)	Filtered E_T min (GeV)	Analysis E_T Cut (GeV)
Background	> 15	17	20
Background	> 47	50	60
Background	> 100	115	130
Background	> 300	345	370

Table 5.3: E_T cuts used in the generation (Pythia ckin 3 value), filter and analysis of the background sample.

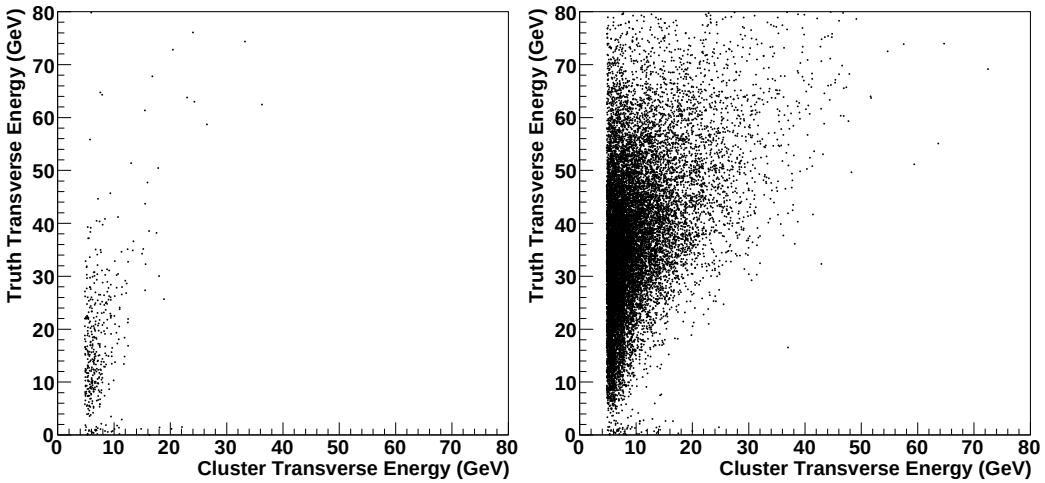

Figure 5.1: Fake clusters found in minimum bias (left) and dijet samples (right). Transverse cluster energy is plotted against the energy found in all stable Monte Carlo truth particles in a cone $\Delta R = 0.2$. Fake clusters can be seen on the bottom left of both plots; events that have a significant detector response but no corresponding particles nearby.

5.3 Preselection

Preselection forms the first stage in the identification of a photon. Selection criteria at this stage are necessarily loose and are designed to ensure that all potential candidates are considered. In the current reconstruction software this stage is the first step after simulation. However, in the actual experiment candidates will be required to pass both the level 1 and level 2 triggers before being fully reconstructed. The effects of these trigger conditions are considered separately in section 5.7.

Preselection is performed using a sliding window clustering algorithm to locate clusters of energy found in the electromagnetic calorimeters. This is a two step process and proceeds as follows:

• Energy from cells in the calorimeter samplings are summed in depth and mapped on to an $\eta - \phi$ matrix with cell granularity $\Delta\eta \times \Delta\phi = 0.025 \times 0.025$. A sliding window algorithm using 5x5 of these cells then scans over this matrix,

locating energy preclusters.

• Once a precluster is found, clusters of different sizes are then formed using the barycentre of the pre-cluster. Photon candidates use a 3x7 cluster formed around this barycentre.

Once such clusters are made, they are then used to form the basis for candidate photons. Only two additional criteria are required at this stage; constraints are placed upon the amount of energy leaking into the hadronic calorimeter and on the association of a track to the cluster:

• The energy in the first hadronic sampling in an area $\Delta\eta \times \Delta\phi = 0.2 \times 0.2$ behind the barycentre is calculated. This is required to be less than 20% of the energy in the 3x7 cluster.

• A match to nearby tracks is performed. Should a track be found within $\Delta\eta \times \Delta\phi = 0.05 \times 0.1$ of the cluster barycentre and the ratio of the energy of the cluster to the momentum of the track (E_{clus}/P_{trk}) be less than 4, then the object is classified as an electron. Clusters that have no such matches form candidate photons.

5.4 Selection Cuts

Candidate photons passing the preselection cuts have a series of selection cuts applied to them. These cuts are designed to reject possible background events and provide a final sample of photons from which an analysis can be performed. The most significant background for photons are the prolific QCD jets. Clearly the ill defined term 'jet' covers a multitude of final states and not all cuts will reject these final states in the same way. In order to reject the greatest number of background events a variety of quantities are considered. These are treated in turn in the next sections.

5.4.1 Hadronic Energy

A photon will deposit most of its energy in the electromagnetic calorimeter with only a small amount leaking into the hadronic calorimeter. This energy leakage is calculated by summing the transverse hadronic energy in a window $\Delta\eta \times \Delta\phi = 0.2 \times 0.2$ behind the candidate cluster. The candidate photon's transverse electromagnetic energy is also calculated and by forming the quantity $E_T(had)/E_T(em)$ the different composition of jets and photons can be shown, figure 5.2. Single photon events show a peak with typically $< 1\%$ of energy leaking into the hadronic calorimeter. Jets on the other hand posses a long tail, with many events containing significant hadronic activity.

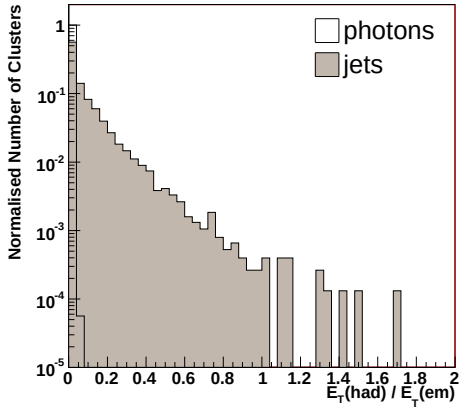

Figure 5.2: The ratio of energy deposited in $\Delta\eta \times \Delta\phi = 0.2 \times 0.2$ region in the hadron calorimeter, divided by the energy in the electromagnetic calorimeter.

5.4.2 Energy Deposition in the Second Electromagnetic Sampling

The second electromagnetic sampling is 16 radiation lengths long and most electromagnetic showers should terminate in this region. Photons, being single particles, should have narrow shower profiles whilst jets, being composed of multiple particles, should be typically broader. By looking at the shower properties for both types of

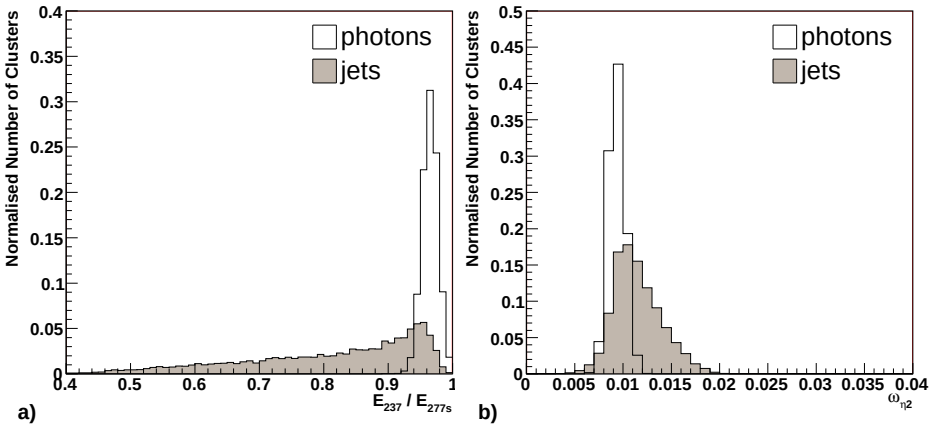

Figure 5.3: (a) The Ratio of the energy deposited in 3x7 cells in the electromagnetic calorimeter divided by the energy deposited in 7x7 cells. (b) The weighted sum of energy deposited in the second sampling of the electromagnetic calorimeter. See text for further explanation.

particles suitable identification cuts maybe chosen.

In this sampling a calorimeter cell measures $\Delta\eta \times \Delta\phi = 0.025 \times 0.025$, and a quantity may be defined by taking the ratio of energy deposited in 3x7 of these cells divided by the energy deposited in 7x7 cells, equation 5.1 below. This quantity, centred around the hottest cell, provides a crude measure of how wide the shower is in η. Wide showers will deposit more energy away from the central region and thus yield lower values; events that deposit all their energy within the region of 3x7 will have the maximal value of 1. Distributions formed for this quantity can be seen in figure 5.3 (a). Single photons events are peaked with $\approx 95\%$ of their energy being contained within the central region. Jets likewise are peaked at $\approx 95\%$, but possess a much longer tail due to their wide multiple particle composition.

$$E_{237/277} = \frac{E_2(3 \times 7)}{E_2(7 \times 7)} \tag{5.1}$$

A lateral shower width in η may also be defined and is given as a weighted sum of the transverse energy (E_c) deposited in 3x5 cells, equation 5.2 below. This sum

is dependent upon the impact parameter point inside the cell and the effect has been unfolded and then normalised to correspond to the impact position in the cell centre [74]. Equation 5.2 gives extra weight to those candidates that have energy far from the shower centre and so provides a complementary quantity with which to discriminate multiple particles events, as shown in figure 5.3 (b).

$$\omega_{\eta 2} = \sqrt{\frac{\sum(E_c \times \eta_c^2)}{\sum E_c} - \left(\frac{\sum E_c \times \eta_c}{\sum E_c}\right)^2} \tag{5.2}$$

Cuts made using the hadronic and second electromagnetic calorimeters will reject events that comprise jets with hadronic particles, or contain multiple particles with wide showers. The majority of background events that remain after these cuts contain narrow showers with little hadronic activity. These events typically contain single or multiple light mesons such as π^0, η and ω.

5.4.3 Energy Deposition in the First Electromagnetic Sampling

As described in section 2.4.2 the first electromagnetic calorimeter comprises thin ($\Delta\eta \times \Delta\phi = 0.003 \times 0.1$) strips and this high granularity allows the shower structure of the candidate particle to be studied. Given the limited depth of the calorimeter (4.3 X_0) not all candidate particles will deposit sufficient energy for this analysis to be performed. In common with previous studies [74, 77] the minimum energy deposition in the first layer is set to be 0.5% of the total transverse energy of the candidate. No cuts are performed for events that do not meet this criteria; identification instead being done solely on the shower profiles in the hadronic and second electromagnetic calorimeters. Figure 5.4 (a) shows the fraction of energy deposited for both photons and jets. Whilst there is a degree of similarity between the two classes of events, it can be seen that photons on average deposit less energy in this calorimeter than jets. Quantities formed with the first electromagnetic calorimeter

can be divided into those looking at the general shower width and those looking at the substructure of individual particle decays, specifically those of the light mesons.

Shower width

The shower is studied in a window $\Delta\eta \times \Delta\phi = 0.0675 \times 0.2$ around the most energetic strip. These 40 strips, 20 in η by 2 in ϕ, are then used to form the quantities outlined below. Only the quantity ω_{tot1} uses all 40 of these, with the other two using seven and three strips respectively.

• The total width (ω_{tot1}) is a weighted sum over all available strips in the region $\Delta\eta \times \Delta\phi = 0.0675 \times 0.2$, equation 5.3, where E_i is the transverse energy of the i^{th} strip and i_{max} is the strip with the highest energy. As with $\omega_{\eta 2}$ this width is dependent upon the impact point within a calorimeter cell, and as before the effect is unfolded. Figure 5.4 (b) shows this distribution for both photons and jets.

$$\omega_{tot1} = \sqrt{\frac{\sum E_i \cdot (i - i_{max})^2}{\sum E_i}} \tag{5.3}$$

• The fraction of energy outside the shower core in η ($fracs1$) is calculated by adding the two ϕ bins together giving strips with total ϕ dimensions of 0.2 radians. The amount of energy found in ± 3 ($E(\pm 3)$) and ± 7 ($E(\pm 7)$) strips either side of the hottest strip is used to measure how well contained the shower is in η, equation 5.4. As can be seen from figure 5.4 (c), typically more than 75% of the photon's energy in the first sampling is contained within this region. Jets containing multiple particles have typically larger values of this quantity.

$$fracs1 = \frac{E(\pm 7) - E(\pm 3)}{E(\pm 3)} \tag{5.4}$$

• The shower width using the three strips ($\omega_{3strips}$) is calculated using strips either side of the most energetic strip, equation 5.5. The quantity is formed in a

similar fashion to ω_{tot1} and likewise similar considerations apply. Figure 5.4 (d) shows the corrected distribution for photons and jets.

$$\omega_{3strips} = \sqrt{\frac{\sum E_i \cdot (i - i_{max})^2}{\sum E_i}} \tag{5.5}$$

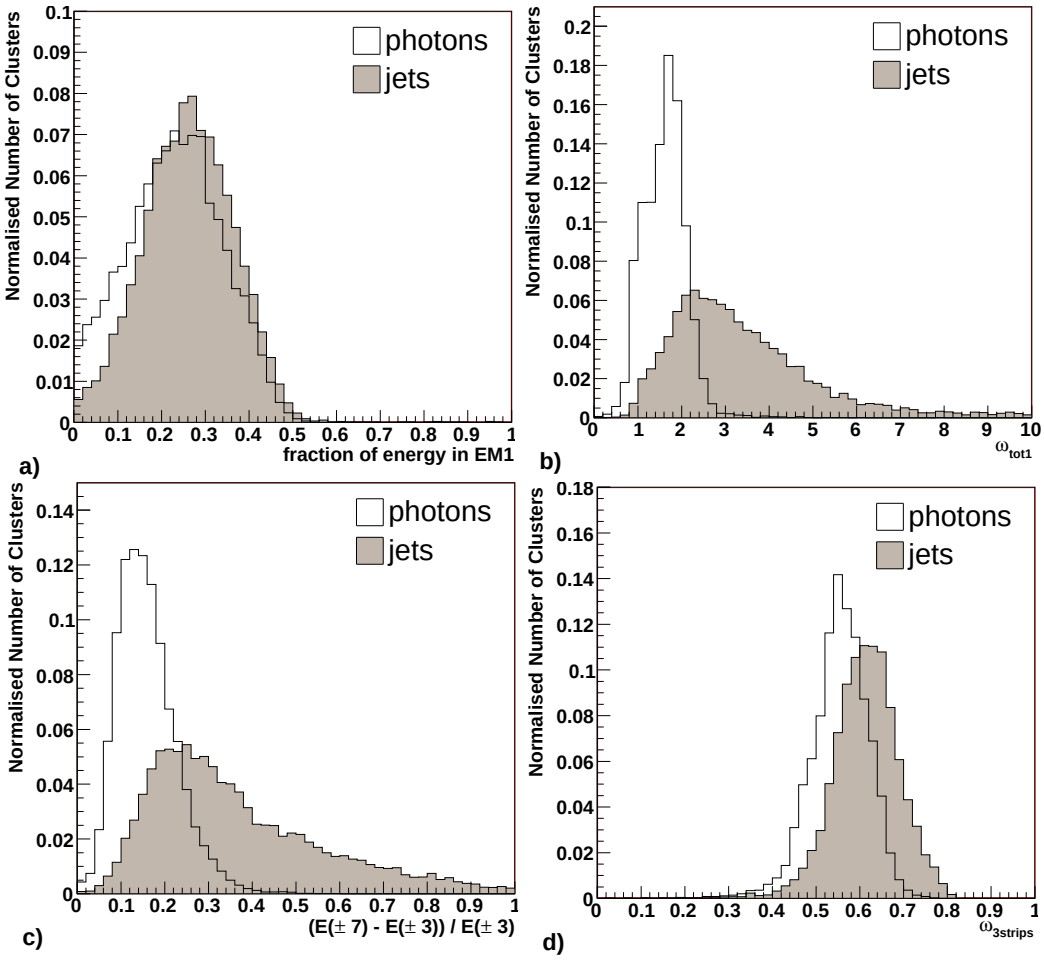

Figure 5.4: Distributions for single photons and jets formed using the first electromagnetic calorimeter. See text for further details.

Search for the second maximum

The most problematic background to photons are those jets that contain one or two light mesons carrying a significant fraction of the fragmented parton momentum.

These mesons in turn decay into two or more photons, often in very close proximity. Rejection against such events is possible, at least at low energies by studying the shower structure in detail. In particular, the fine granularity of the strips is used to try and detect the two maxima caused by the two photons from the meson final state. As before, the shower is studied in a window $\Delta\eta \times \Delta\phi = 0.0675 \times 0.2$ around the most energetic cell. These 40 cells are scanned, looking for a second maximum, and in the case where multiple second maxima are found, the highest one is used. The energy found in this second maxumum is given by E_{max2}. Two quantities of interest are used and discussed below:

• By looking at the size of the second maximum (E_{max2}), events that contain significant amounts of energy away from the initial peak may be detected. Such events indicate a more complicated shower than would be expected from a single particle. The size of the second maximum is expected to scale approximately linearly with E_T and as such equation 5.6 below is formed; plotted in figure 5.5 (a) for photons and jets. There is a clear difference between the two types of events with photons being strongly peaked with $E_{max2}/E_T < 0.01$, showing the relative insignificance of their second peak.

$$Significance = E_{max2}/E_T \tag{5.6}$$

• The difference in energy of the second maximum and the strip with the minimum energy between first and the second maximum strip is also formed, see equation 5.7 below. For events that have two well resolved double peaks (from two photons) in the first sampling this value should be large, indicating the separation of the two peaks. Values that are close to zero are indicative of a small second maximum or of peaks that are not well resolved. Distributions for photons and jets are shown in figure 5.5 (b) and again a clear difference between photons and jets can be seen. Photons typically have $\Delta E < 100$ MeV and demonstrate the fact that these events have second peaks only slightly larger than the minimum value E_{min}; i.e. their second maximas are small and so probably unrelated to other particles in

the event.

$$\Delta E = E_{max2} - E_{min} \tag{5.7}$$

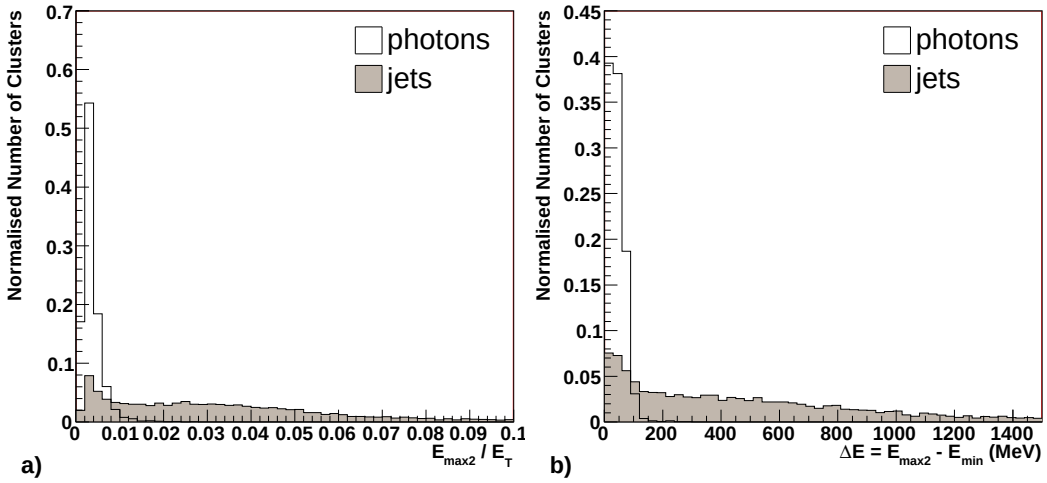

Figure 5.5: Distributions formed using energy deposited in the first electromagnetic calorimeter. The focus of these two distributions is to try and reject against any light mesons present in the event. See text for further details.

5.5 η Dependence

As discussed in section 2.4.2 the electromagnetic calorimeter construction changes with η. This change, together with the varying material profile, as shown in figure 5.6, motivates the provision of η dependent identification cuts. Figure 5.7 shows how the eight identification criteria discussed in the previous section change with η. Figures 5.7 (d) and (e) almost completely shadow the material profile, with many of the other plots showing increases correlated with the amount of material the shower traverses. Distributions made with the second electromagnetic sampling, figures 5.7 (b) and (c), use larger cells and as a result seem to be less sensitive to material in the detector. The resultant division of the η range for photon identification is given below.

- $|\eta| \leq 0.8$
- $0.8 < |\eta| \leq 1.37$
- $1.37 < |\eta| \leq 1.52$
- $1.52 < |\eta| \leq 1.8$
- $1.8 < |\eta| \leq 2.0$
- $2.0 < |\eta| \leq 2.4$

As can be seen from figure 5.6 significant amounts of material are present in the region $1.37 < |\eta| \leq 1.52$. This region, sometimes referred to as the crack region, marks the transition from the barrel to the end-cap calorimeters and the routing of many of the Inner Detector readout and power services through this gap, see figure 2.6. Due to the difficulty of accurate photon identification within this high material region it has been excluded from the analysis and identification is instead optimised separately for the five remaining η bins. The effect of this is to improve the identification plots shown in section 5.4. Plots for the eight identification criteria are repeated in figure 5.8 with the restricted range of $|\eta| \leq 0.8$. The distributions show an increased resolution with stronger peaks and smaller tails. This should lead to improved photon identification and increased rejection of background events. Similar plots can be made for each of other four η ranges but are omitted here for brevity.

5.6 Isolation

The identification criteria discussed so far have concentrated on the area immediately surrounding the calorimeter shower. Single photons from many different processes are expected to be isolated, consideration of the area surrounding the

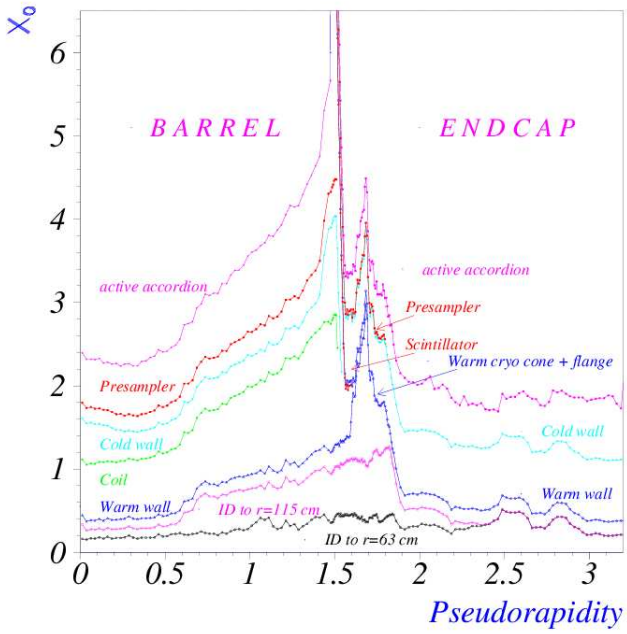

Figure 5.6: The anticipated material budget over the ATLAS detector as at May 1999. The figure has been taken from [21].

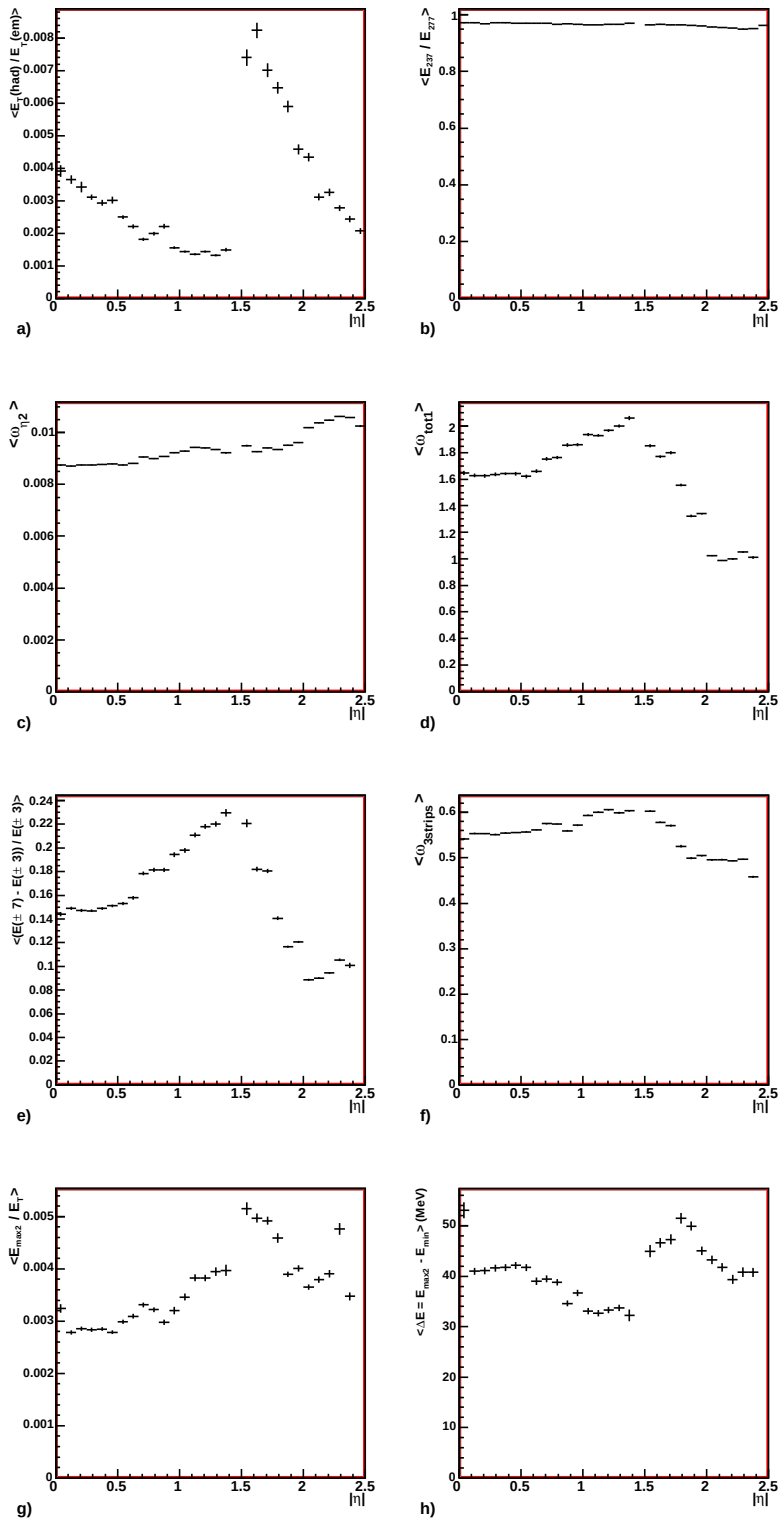

Figure 5.7: The η dependence of the identification variables. Plotted are the profile of the identification variables discussed in the text. Distributions are shown for single photons produced at 20 GeV.

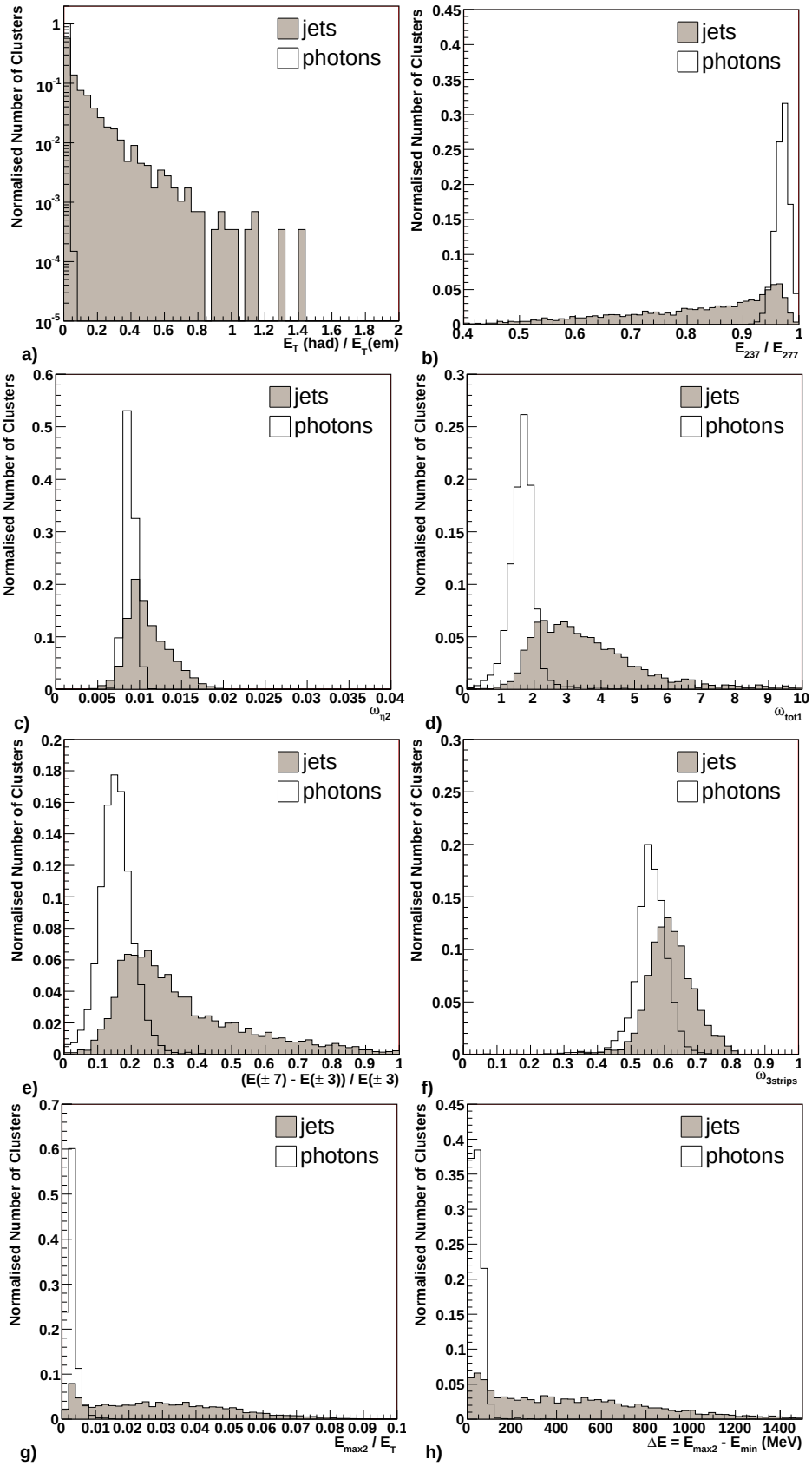

Figure 5.8: Photon identification distributions for candidate particles in the region $|\eta| < 0.8$. *Distributions are for jet and single photons events. See text for further details.*

shower may yield further improvements in rejection. The amount of energy is calculated for an isolation cone of radius $\Delta R = \sqrt{(\Delta\eta)^2 + (\Delta\phi)^2}$ where $\Delta\eta$ and $\Delta\phi$ are the displacements in η and ϕ from the candidate photon. The inner ring of this isolation is bounded by the region of 5x7 calorimeter cells and is approximately $\Delta\eta \times \Delta\phi = 0.125 \times 0.175$ in size. Added to this is the energy deposited in the hadronic calorimeter immediately behind this core giving a three dimensional isolation of the shower. Since this isolation scales roughly with energy, as shown in figure 5.9, candidates are considered if they possess a fraction of energy ϵ_{iso} less than some fixed quantity ϵ_γ, as expressed in equation 5.8. Figure 5.9 shows the mean value of energy found in the isolation ring for each of the samples. There will of course be tails associated with these mean values, the length and severity of which will determine both its usefulness in rejecting background events and the efficiency with which it is able to do this.

$$\frac{E_T^{iso}}{E_T^{\gamma}} = \epsilon_{iso} < \epsilon_\gamma \tag{5.8}$$

The amount of energy found in a cone $\Delta R = 0.4$ but outside the core 5x7 cells is shown in figure 5.10 for photons and jets. With only the preselection criteria applied, figure 5.10 (a), QCD jets can be seen to have a large amount of activity in the region surrounding the central 5x7 core. Even with calorimeter identification, figure 5.10 (b), there is a clear distinction between the two samples indicating further rejection may be obtained from using this quantity.

Optimisation of this quantity requires the removal of events that have a large amount of energy in the isolation cone. This in turn requires a good knowledge of the level of activity expected in this region. Three effects contributing to the energy around a photon are noise, the underlying event and pile-up. Noise has been included as part of the simulation, however the effects of the underlying event and of pileup are not present in the single photon sample used in figure 5.10. Both effects are most apparent at low E_T, where they will tend to broaden the identification distributions and, as will be discussed in section 5.11, lead to an increase in the tails

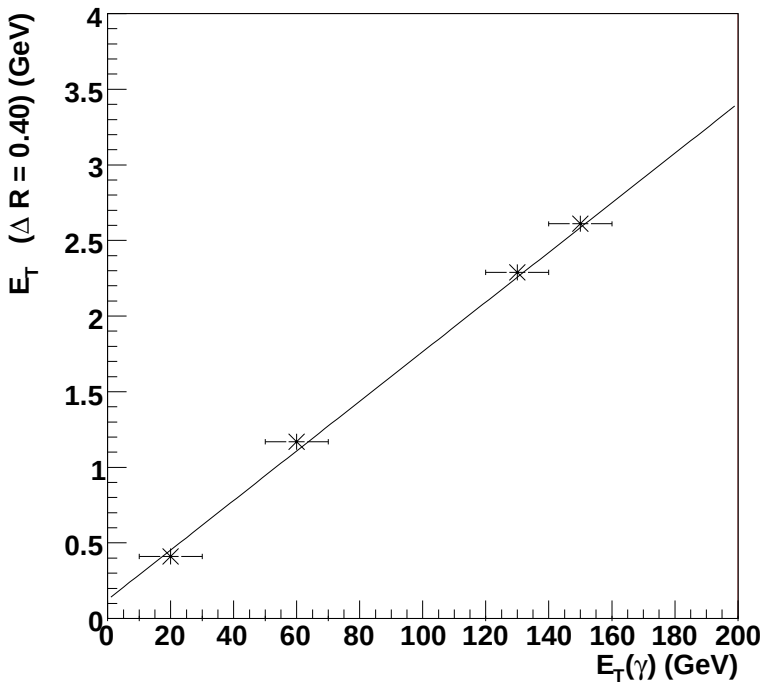

Figure 5.9: Isolation of single photons at four different energies. Plotted is the mean value of energy found in a cone of $\Delta R = 0.4$ around a 5x7 core.

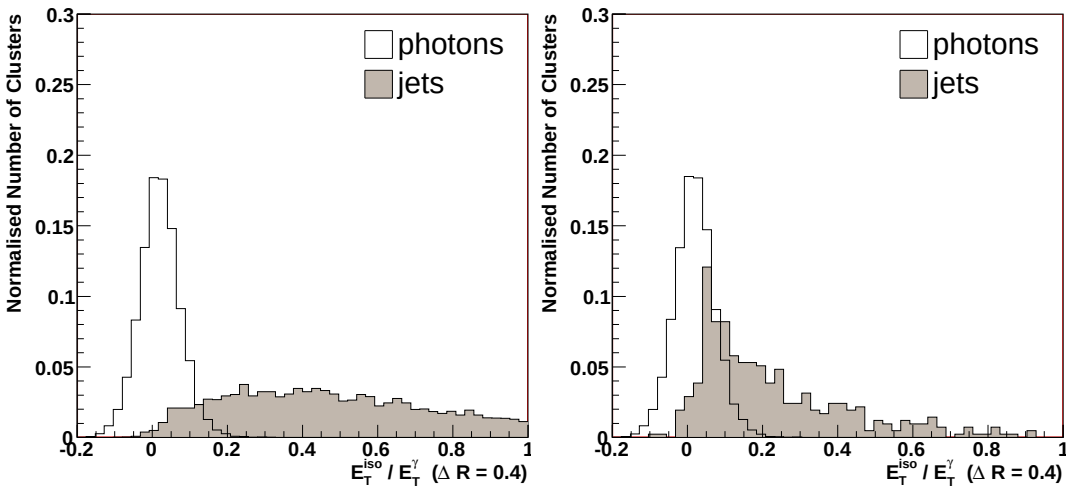

Figure 5.10: Isolation of photons and jets for a cone of $\Delta R = 0.4$ around a 5x7 core. On the left is shown distribution for particles passing the preselection criteria and on the right events that have passed calorimeter only identification cuts.

associated with these distributions.

5.7 Trigger Selection

In order for an event to be read out of the ATLAS detector, both the level 1 (LVL1) and high-level trigger (HLT) conditions must be satisfied. The LVL1 trigger is responsible for reducing the observed event rate in the ATLAS detector from 1 GHz to 75 kHz, the HLT then in turn reduces this to O(100) Hz for readout. At the time of writing both trigger menus have yet to be finalised, however, almost all of the technical aspects of the trigger systems have been agreed and are being implemented, further details of which can be found in [72, 73].

Photon identification at the LVL1 stage will be based solely on calorimeter information. Calorimeter cells are summed to form so called 'trigger towers' that measure $\Delta\eta \times \Delta\phi = 0.1 \times 0.1$. A sliding window algorithm is then moved around this space looking for clusters of energy and once found is measured by 1×2 or 2×1 trigger towers. If isolation is required, the amount of energy in the 12 trigger towers surrounding the 2×2 trigger tower cluster core is used. Possible trigger menus for photons at low and (high) luminosity are given below,

- e20i (e30i)
- 2e15i (2e20i)
- e60

where 'e' denotes the amount of transverse energy needed in the trigger tower, the number '2' before this quantity signifies triggers that requires two trigger objects and 'i' denotes an isolation requirement. The single object triggers e20i and e30i are both isolated and should be efficient for photons and electrons with $E_T > 20$ (30) GeV. Thresholds for this and for all triggers will be dependent upon the exact event rate, trigger performance, and priority given by the collaboration. All of these factors

are currently under review and as such the trigger menus are expected to evolve significantly. Triggers that require two objects, 2e15i and (2e20i), have lower event rates and as a result will almost certainly have lower thresholds as indicated. Due to the lower event rate at high E_T, the trigger e60 in all likelihood will be non-isolated. In addition to these, other prescaled triggers for photons may also exist; these would allow a certain proportion of low E_T photon events to be taken.

Triggering by the high level trigger (HLT) uses many of the quantities outlined in section 5.4. The trigger comprises a level 2 trigger and an event filter. For the level 2 trigger, only information from the calorimeters is used, since information from the inner detector would be too time consuming. The event filter has access to the entire event record and is the final stage before permanent write out. As with the LVL1 trigger the optimisation for the HLT is still being performed, however, it has a similar basic goal of maximising the rejection whilst maintaining a high photon efficiency.

No trigger analysis was performed with the generated samples as at the time of generation the trigger simulation was not included in the standard event reconstruction. Nevertheless, the effect on the rejection obtained in section 5.8 should be limited. Given that the quantities used in both triggers have either similar or less granularity than those found in section 5.4, these triggers should not remove many additional background events. Efficiency for both triggers is likely to be in the region of 90%, as shown in [74].

5.8 Results

5.8.1 Photon Efficiency

Results are presented for samples at four different energies, 20, 60, 130 and 370 GeV. Photon candidates are required to pass cuts on the identification criteria outlined

above. These were optimised over the five η ranges described in section 5.5, to give a single photon efficiency of $\approx 90\%$. Efficiency is calculated as the number of events passing these cuts relative to the number of preselected candidate photons. Table 5.4 shows this efficiency for the four types of cuts made after the preselection. Cuts made using the second electromagnetic calorimeter can be seen to remove very few true photon events. This is due to the strongly peaked distributions found in this sampling (for example figure 5.8 (b) and (c)) enabling cuts to be made tight up against these peaks with little loss of signal. Shower distributions formed using the hadronic and first electromagnetic calorimeters (for example figure 5.8 (c)) contain longer tails and so are therefore more sensitive to these identification cuts, which in turn leads to a greater loss of efficiency. Previous studies [74, 76] show equal reductions in efficiencies across all three calorimeters; however, these studies have an additional cut in the second electromagnetic calorimeter, on the size of the shower in ϕ. This distribution has a comparably longer tail and is the source of their reduction in efficiency. No such cut was made in this analysis.

Tables 5.5 and 5.6 show efficiencies for direct photons and bremsstrahlung photons using the same identification cuts. Total direct photon efficiencies increase from 80% at 20 GeV to around 87% in the high E_T range. Efficiencies are lower than the single photon case for all E_T ranges, however, the difference decreases with increasing energy. At low energies activity from the underlying event, not present for the single photon sample, causes broadening of the identification distributions and results in the removal of more events. As the energy increases, the relative importance of the underlying event decreases and the efficiencies approach that for the single photon case, as shown in figure 5.11. Bremsstrahlung photon efficiency can be seen to decrease over the E_T range from 67% to 35% and has its cause in the softening of the dijet E_T spectrum. The likelihood of the bremsstrahlung process is strongly dependent upon the fraction of the fragmenting parton's E_T carried off by the radiated photon. Radiated photons with small fractions of the parton's E_T are much more common than those with large fractions. As a result, since the high E_T samples have a softer E_T jet spectrum, they have proportionally more 'higher E_T'

jets and consequently photons radiated with a 'small' fraction of their E_T are more likely to pass the kinematic cuts. The remaining energy is present in the associated jet and it is the increased activity of this jet and its associated particles that causes the loss of efficiency.

Cuts	$\approx$ 20 GeV	$\approx$ 60 GeV	$\approx$ 130 GeV	$\approx$ 370 GeV
Preselection	100%	100%	100%	100%
Hadronic calorimeter	97.2%	97.3%	98.1%	96.6%
Second electromagnetic calorimeter	97.0%	97.3%	98.9%	96.4%
First electromagnetic calorimeter	91.2%	90.5%	90.8%	90.4%
Isolation	90.3%	90.3%	90.1%	89.8%

Table 5.4: Photon identification efficiency for single photons in the range $|\eta| \leq 2.4$ excluding the crack region, $1.37 < |\eta| \leq 1.52$. The associated errors for these cumulative cuts are shown in figure 5.11.

Cut	$\approx$ 20 GeV	$\approx$ 60 GeV	$\approx$ 130 GeV	$\approx$ 370 GeV
Preselection	100%	100%	100%	100%
Hadronic calorimeter	90.2%	92.9%	95.2%	95.3%
Second electromagnetic calorimeter	89.9%	92.8%	94.9%	95.3%
First electromagnetic calorimeter	83.4%	88.8%	91.3%	87.6%
Isolation	80.5%	88.4%	87.0%	86.3%

Table 5.5: Photon identification efficiency for direct photons in the range $|\eta| \leq 2.4$ excluding the crack region, $1.37 < |\eta| \leq 1.52$. The associated errors for these cumulative cuts are shown in figure 5.11.

5.8.2 Converted and Non-converted Photons

Approximatively 1/3 of photons will convert somewhere inside the Inner Detector. The conversion vertex of these photons is shown in figure 5.12 and details an 'X-Ray'

Cut	$\approx$ 20 GeV	$\approx$ 60 GeV	$\approx$ 130 GeV	$\approx$ 370 GeV
Preselection	100%	100%	100%	100%
Hadronic calorimeter	82.7%	78.0%	67.2%	48.7%
Second electromagnetic calorimeter	82.7%	75.2%	66.9%	48.7%
First electromagnetic calorimeter	75.3%	65.1%	63.3%	43.4%
Isolation	66.6%	54.1%	50.0%	34.8%

Table 5.6: Photon identification efficiency for bremsstrahlung photons in the range $|\eta| \leq 2.4$ *excluding the crack region,* $1.37 < |\eta| \leq 1.52$*. The associated errors are shown in figure 5.11.*

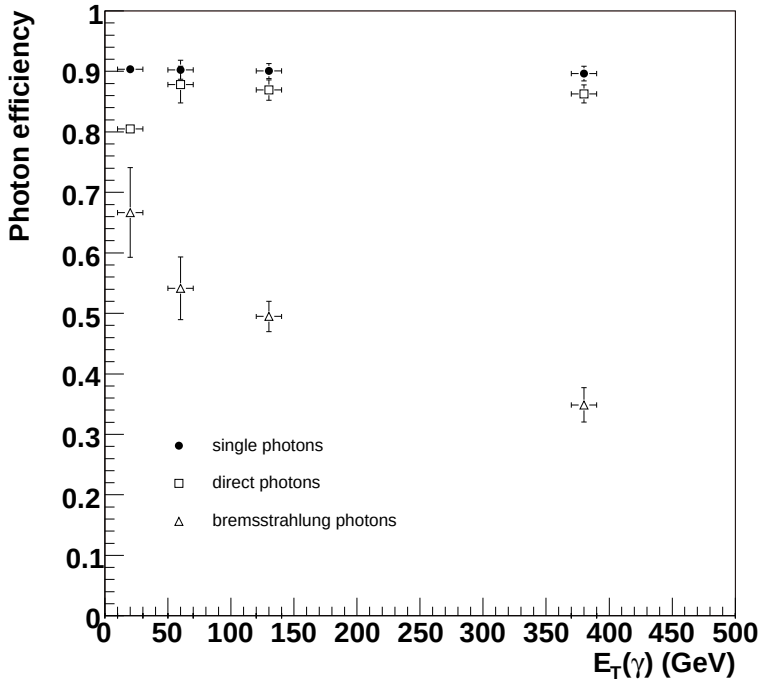

Figure 5.11: Photon efficiency as a function of E_T *for three different sources of photons.*

of the material present in the region $R < 115$ mm. The Pixels, SCT and TRT are all clearly visible, as are the barrel and end-cap structures of these detectors.

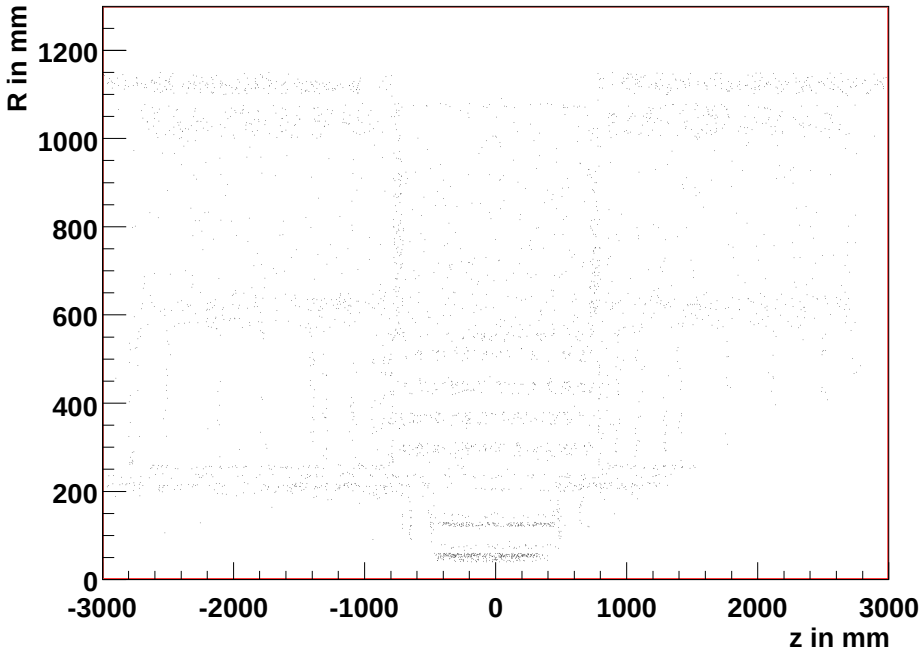

Figure 5.12: Photon conversion vertices.

Figures 5.13 and 5.14 show photon efficiency for the 20 GeV sample using alternative definitions of efficiency. Figure 5.13 shows the efficiency with respect to the MC truth, for converted and non-converted photons as well as the sample as a whole. It shows that a significant number of converted photons are lost in preselection, in particular photons that have converted before a radius of 300 mm. This can be explained with reference to the preselection criteria of section 5.3. Photons that convert into electron-positron pairs within 300 mm have 4 silicon layers of the SCT to traverse before entering the calorimeter. As a result there is a high probability that their electromagnetic clusters will have a track associated with them and that these particles will be reconstructed as electrons. These conversion electrons and positrons may be recombined in an additional reconstruction step to form their parent photon; however, no attempt to do so is made here.

As a result and as previously stated the benchmark for efficiency is taken as those photons that pass the preselection criteria as shown in figure 5.14. Photon efficiency

for the calorimeter cuts, figure 5.14 (a), is flat across η and for those photons that convert, it increases with the conversion radius R, figure 5.14 (b). Electrons and positrons from converted photons are bent in opposite directions by the magnetic field present in the Inner Detector. When the electron and positron do not separate enough to form two distinct showers, energy is deposited in the calorimeter over a broader area and leads to a widening of the identification distributions. For a fixed energy, the size of this effect is dependent on the conversion distance R, with earlier conversions showering earlier, separating more and hence having a reduced efficiency. As the energy of the photon increases, the opening angle between the electron and positron reduces and this effect becomes less pronounced. Figures 5.14 (c) and (d) show efficiencies for the isolation cuts implemented and since these cuts were specifically optimised to remove $< 1\%$ of single photons the effect of this additional cut is small.

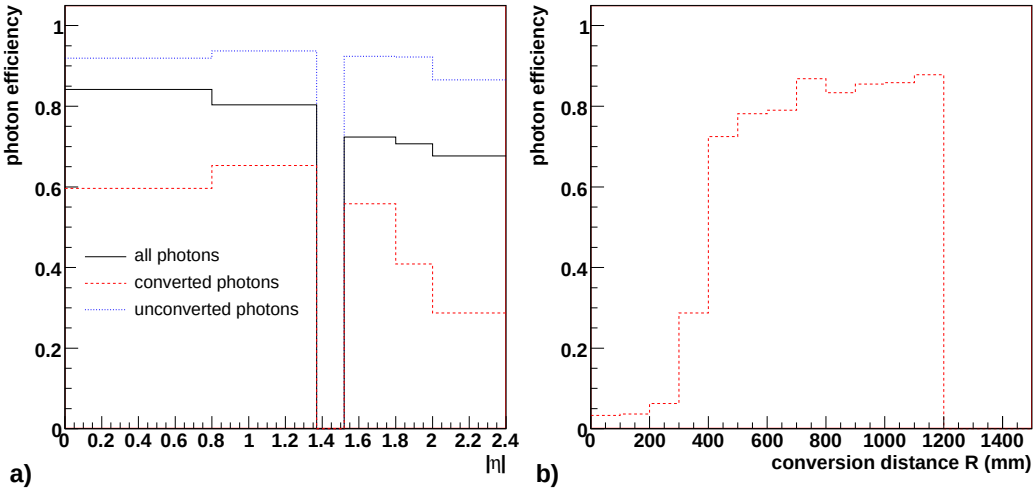

Figure 5.13: Efficiency of photons that pass the calorimeter cuts defined relative to MC particles produced using the single particle gun. On the left efficiency as a function of η and on the right, for those photons that convert, the efficiency as a function of conversion radius R.

In summary, for photons that convert inside the Inner Detector, these plots show efficiency is strongly dependent upon the conversion radius. Photons converting very early will require an additional reconstruction algorithm to recombine the conversion

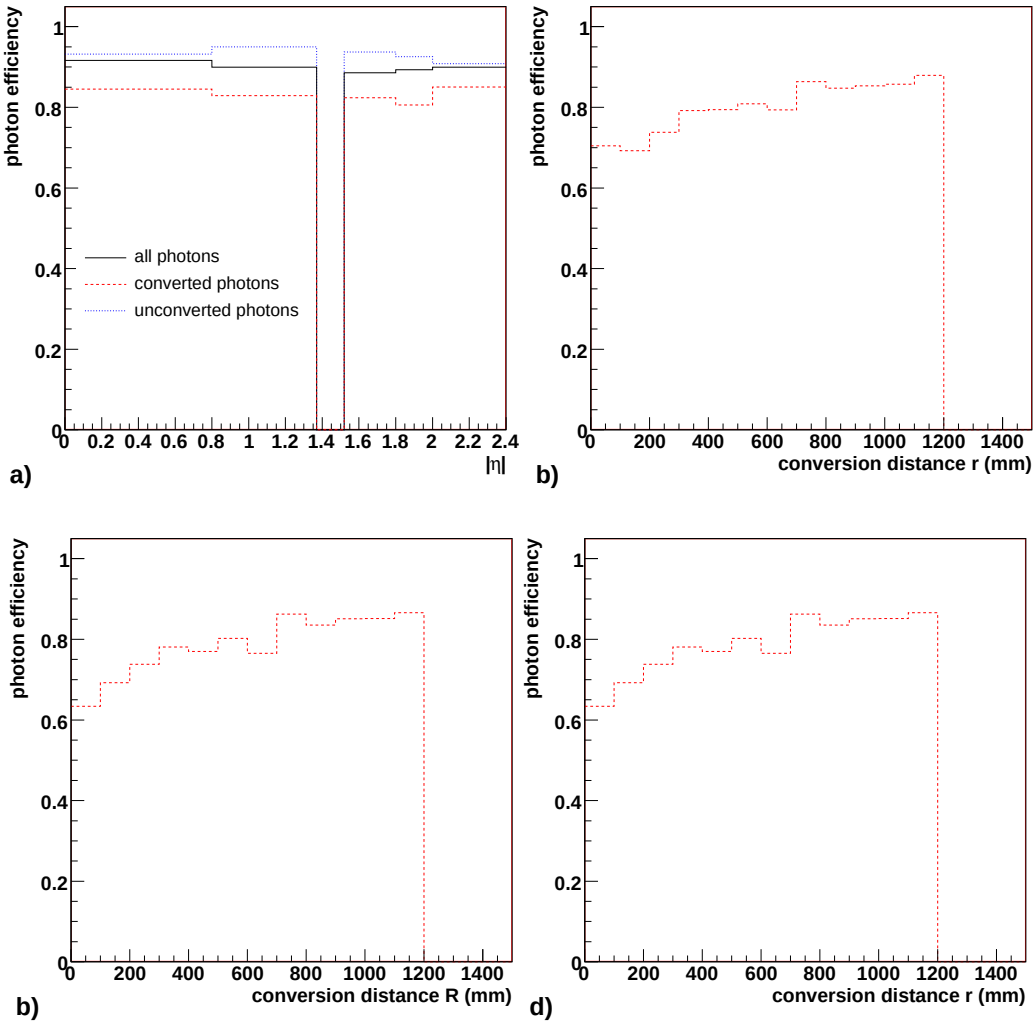

Figure 5.14: Photon efficiency defined relative to photons that pass the pre-selection criteria. On the left efficiency as a function of η and on the right, for those photons that convert, the efficiency as a function of conversion radius R. (a) and (b) show photons that pass the calorimeter identification cuts, (c) and (d) show photons that additionally pass the isolation criteria.

electron and positron; photons converting later are generally better reconstructed the later they convert. Total photon efficiency has been optimised to 90% of those single photons passing the preselection cuts. Direct and bremsstrahlung photon efficiencies are both lower than this, with direct photon efficiency increasing with E_T to around 90% at 60 GeV. Bremsstrahlung photon efficiency decreases with E_T to around 35% at 370 GeV.

5.8.3 Jet Rejection

To obtain a value for the rejection of jets against photons, the number of jets passing the identification cuts is normalised to the number of jets produced. In common with previous analyses this normalisation is done to the number of jets obtained from the ATLAS fast detector simulation, ATLFAST [27]. The rejection is given by

$$R = \frac{N(ATLFAST\ jets)}{N(fakes)} \tag{5.9}$$

The number of ATLFAST jets corresponding to each of the samples is given in table 5.7. Calorimeter and isolation cuts used in this analysis are summarised in table 5.8. Calorimeter cuts have been optimised separately for each E_T range and for each of the five η bins. Isolation cuts were optimised to remove $< 1\%$ of photons from the single photon sample and were done for each of the four E_T samples as a whole. This represents a light isolation criterion comparable to previous studies [75]. Rejections obtained using just the calorimeter cuts, table 5.9, can be seen to increase with E_T from 2,611 at 20 GeV up to 12,773 at 370 GeV albeit with a large uncertainty. These are also plotted as a function of E_T in figure 5.15 and show more clearly the progression with energy. This compares favourably with studies using the full detector layout and with the older Geant3 detector simulation package [74–76]. Rejections stated in [74] include direct and bremsstrahlung photons, specifically excluded here since they form part of the signal of interest. These previous studies have focussed on the low E_T range where jet rejection is important

for the $H \rightarrow \gamma\gamma$ discovery channel. Photon efficiency was optimised to 80% in these studies, and the difference to the 90% observed here is approximately accounted for by the absence of pileup; this effect is discussed in more detail in section 5.11.

Sample (GeV)	Number of Generated Events	ATLFAST Jets per Event
20	2,751,392	0.31
60	891,991	0.40
130	2,637,661	0.37
370	646,905	0.47

Table 5.7: The number of jets per generated event found with the ATLFAST simulation. Events were generated with Pythia as described in table 5.3. The rates shown are for jets in the range $|\eta| \leq 2.4$ *excluding the region,* $1.37 < |\eta| \leq 1.52$.

The rejection factor when including the isolation criterion, figure 5.16, offers an improvement of between 2 and 4 increasing with E_T, although the very high E_T range suffers from low statistics. With the current data available it is unclear whether the rejection reaches a similar plateau to figure 5.15, or continues to increase with E_T. Again the results in the region of energy overlap compare well to those obtained in [75, 76] although as discussed in section 5.11 the results here are probably high for the low E_T samples due to the absence of pileup.

In order to assess the effectiveness of each of the four types of cuts they were performed in a variety of combinations, as shown in table 5.10. A high degree of correlation can be seen between the different types of cuts and in each case the cut that is performed first reduces the background the most. Since most background events look dissimilar to photons, they can be removed by any one of a number of cuts. If the isolation criteria are applied first, this yields rejections that are approximately twice that of all the calorimeter cuts combined. This cut removes very effectively events that do not fragment cleanly into well isolated photons, although it should be noted that this cut will be strongly dependent upon the amount of noise and any additional activity in the event.

GeV		$\lvert\eta\rvert \leq 0.8$	$0.8 < \lvert\eta\rvert \leq 1.37$	$1.37 < \lvert\eta\rvert \leq 1.8$	$1.8 < \lvert\eta\rvert \leq 2.0$	$2.0 < \lvert\eta\rvert \leq 2.4$
$20 \leq E_T < 60$	E_{had}/E_T	0.03	0.008	0.03	0.02	0.015
	$E_{237/277}$	0.925	0.94	0.92	0.94	0.93
	$\omega_{\eta 2}$	0.011	0.011	0.012	0.0115	0.0125
	$\omega_{3strips}$	0.68	0.7	0.7	0.6	0.56
	ω_{tot1}	2.2	2.7	2.6	1.8	1.4
	fracs1	0.26	0.32	0.35	0.18	0.16
	E_{max2}/E_T	0.01	0.012	0.01	0.01	0.011
	ΔE	100.	150.	120.	100.	100.
	isolation	$\epsilon_{iso} < 15\%$	$\epsilon_{iso} < 15\%$	$\epsilon_{iso} < 15\%$	$\epsilon_{iso} < 15\%$	$\epsilon_{iso} < 15\%$
$60 \leq E_T < 130$	E_{had}/E_T	0.02	0.01	0.03	0.02	0.02
	$E_{237/277}$	0.94	0.94	0.94	0.95	0.94
	$\omega_{\eta 2}$	0.011	0.011	0.011	0.011	0.012
	$\omega_{3strips}$	0.64	0.44	0.65	0.57	0.58
	ω_{tot1}	2.2	2.3	2.2	2.0	1.4
	fracs1	0.21	0.27	0.27	0.2	0.14
	E_{max2}/E_T	0.003	0.0035	0.005	0.004	0.0045
	ΔE	100.	100.	120.	120.	120.
	isolation	$\epsilon_{iso} < 7.5\%$	$\epsilon_{iso} < 7.5\%$	$\epsilon_{iso} < 7.5\%$	$\epsilon_{iso} < 7.5\%$	$\epsilon_{iso} < 7.5\%$
$130 \leq E_T < 370$	E_{had}/E_T	0.01	0.008	0.03	0.02	0.015
	$E_{237/277}$	0.95	0.95	0.94	0.95	0.94
	$\omega_{\eta 2}$	0.01	0.012	0.012	0.0115	0.012
	$\omega_{3strips}$	0.62	0.64	0.66	0.6	0.56
	ω_{tot1}	2.0	2.3	2.3	2.0	1.4
	fracs1	0.2	0.3	0.3	0.18	0.16
	E_{max2}/E_T	0.0017	0.0025	0.003	0.002	0.0025
	ΔE	100.	90.	130.	110.	130.
	isolation	$\epsilon_{iso} < 6\%$	$\epsilon_{iso} < 6\%$	$\epsilon_{iso} < 6\%$	$\epsilon_{iso} < 6\%$	$\epsilon_{iso} < 6\%$
$370 \leq E_T$	E_{had}/E_T	0.015	0.01	0.02	0.02	0.015
	$E_{237/277}$	0.95	0.95	0.94	0.95	0.94
	$\omega_{\eta 2}$	0.01	0.01	0.011	0.011	0.01
	$\omega_{3strips}$	0.60	0.62	0.68	0.6	0.55
	ω_{tot1}	2.0	2.5	2.2	2.0	1.4
	$fracs1$	0.18	0.24	0.3	0.18	0.2
	E_{max2}/E_T	0.001	0.001	0.0015	0.0013	0.0015
	ΔE	100.	100.	150.	140.	130.
	isolation	$\epsilon_{iso} < 5\%$	$\epsilon_{iso} < 5\%$	$\epsilon_{iso} < 5\%$	$\epsilon_{iso} < 5\%$	$\epsilon_{iso} < 5\%$

Table 5.8: Values for the calorimeter and isolation cuts. Calorimeter optimisation was done for each energy range and for each of the five η bins shown so that the final photon efficiency of $\approx 90\%$ was obtained. For the isolation criteria the amount of energy inside a cone of $\Delta R = 0.4$ (relative to the candidate photon) was optimised for each energy range. This removed $< 1\%$ of single photon candidates.

Cut	$\approx$ 20 GeV	$\approx$ 60 GeV	$\approx$ 130 GeV	$\approx$ 370 GeV
Preselection	71.3 ± 0.7	70.6 ± 1.0	73.0 ± 0.6	66.7 ± 1.0
Hadronic calorimeter	$1,200 \pm 45$	$2,190 \pm 172$	$3,419 \pm 203$	$3,195 \pm 341$
Second electromagnetic calorimeter	$1,432 \pm 59$	$2,532 \pm 213$	$4,183 \pm 274$	$4,296 \pm 513$
First electromagnetic calorimeter	$2,611 \pm 144$	$6,052 \pm 788$	$7,860 \pm 706$	$12,773 \pm 2,391$
Isolation	$(4.7 \pm 0.4) \times 10^3$	$(1.3 \pm 0.2) \times 10^4$	$(2.4 \pm 0.4) \times 10^4$	$(6.1 \pm 2.5) \times 10^4$

Table 5.9: Rejection rates (R) for background events in the range $|\eta| \leq 2.4$ excluding the crack region, $1.37 < |\eta| \leq 1.52$. Cuts are applied in sequence, top to bottom. The rates shown at the first electromagnetic calorimeter represent rejections obtained using all three of the calorimeters.

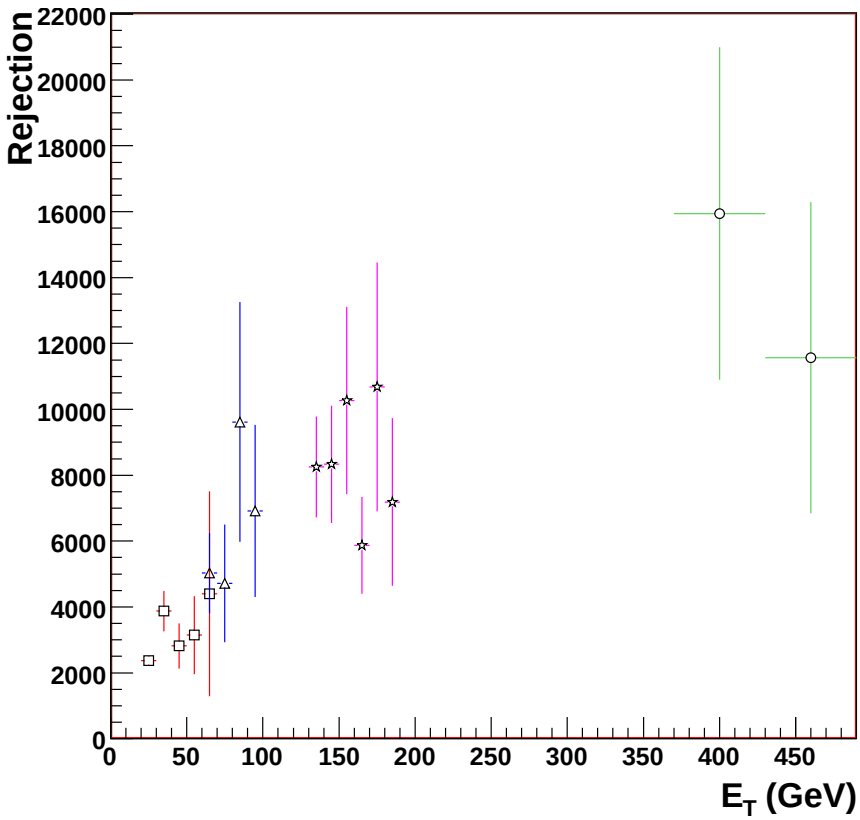

Figure 5.15: Jet rejection as a function of E_T. Shown are the four data samples for calorimeter only identification.

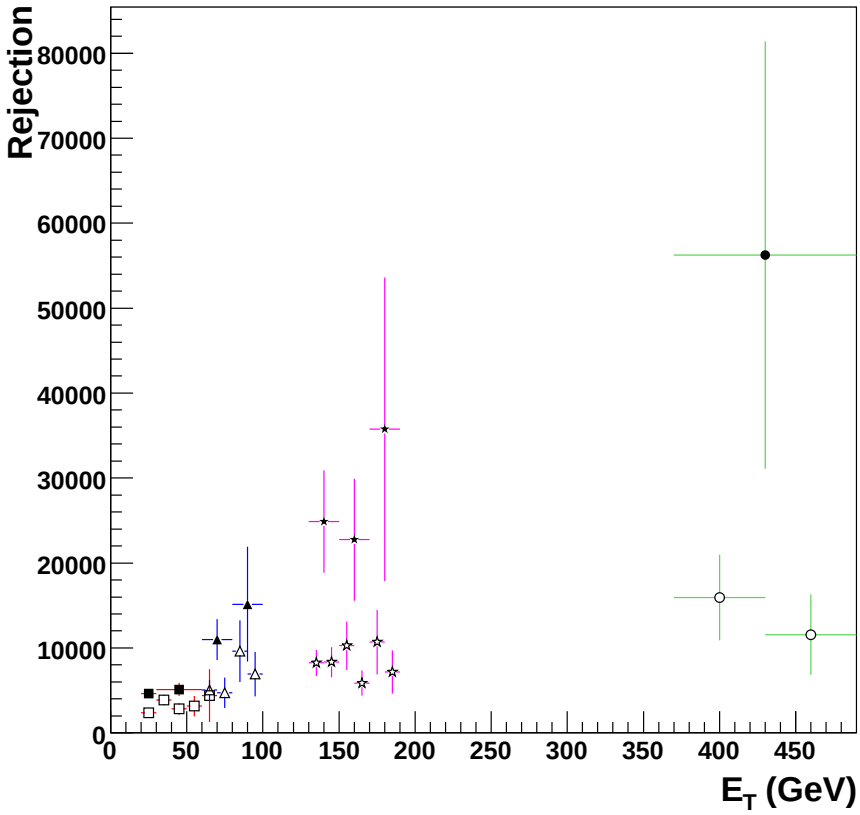

Figure 5.16: Jet rejection as a function of E_T. Shown are the four data samples for calorimeter only identification (open points) and rejection for isolated photons (solid points).

Cut	Rejection	Cut	Rejection
Preselection	73	Preselection	73
Second electromagnetic calorimeter	3,883 (53)	First electromagnetic calorimeter	6,962 (95)
First electromagnetic calorimeter	7,383 (1.9)	Hadronic calorimeter	7,383 (1.1)
Hadronic calorimeter	7,860 (1.1	Second electromagnetic calorimeter	7,860 (1.1)
Isolation	23,771 (3.0)	Isolation	23,771 (3.0)
Preselection	73	Preselection	73
First electromagnetic calorimeter	6,962 (95)	Isolation	13,536 (185)
Second electromagnetic calorimeter	7,440 (1.1)	First electromagnetic calorimeter	23,205 (1.7)
Hadronic calorimeter	7,860 (1.1)	Hadronic calorimeter	23,205 (1.0)
Isolation	23,771 (3.0)	Second electromagnetic calorimeter	23,771 (1.0)

Table 5.10: Identification of photons with $E_T > 130$ GeV. Rejection rates are for background events in the range $|\eta| \leq 2.4$ excluding the crack region, $1.37 < |\eta| \leq 1.52$. Cuts are applied in sequence, top to bottom and in brackets are the incremental increases due to each cut.

5.9 Categorisation of Fakes

Showers that were reconstructed as a photon were analysed to determine their true identity. The MC truth was used to investigate all particles within a cone of $\Delta R = 0.2$ as a possible source for the 'photon'. Given the Geant4 bug outlined in section 5.2, there exists the possibility that the reconstructed photon had no source, i.e. that it is the result of the simulation bug. In order to remove these cases, at least 80% of the reconstructed photon energy was required to be present within a $\Delta R = 0.2$ cone in the truth (the rejections quoted above include this requirement). The sensitivity of the rejection factors to the choice of ΔR and energy was investigated. For the 130 GeV sample, changing ΔR to 0.4 and 0.1 had no discernible effect on the rejections obtained. Likewise requiring 70% or 90% of the photon energy be found in the truth had no significant effect on the rejection. Similar results were obtained for the other samples and from this analysis it is concluded that the sensitivity of the rejection to these requirements was small.

The composition of background events that pass the identification cuts is pre-

sented in table 5.11. These show that the dominant source of events passing the calorimeter identification cuts is from single π^0s. This proportion is increased further by the addition of the isolation cut which removes events that have a multiple particle nature. Although such a cut cannot distinguish the multiple particles causing the reconstructed photon, it can remove other particles associated with these events that do not fragment into just a single particle. A decay such as $\omega^0 \rightarrow \pi^+\pi^-\pi^0$ may pass calorimeter cuts, the π^0 being reconstructed as a possible photon candidate. However, although the π^0 is unlikely to fail the isolation cut, the decay as a whole may do so, due to presence of the other particles in the event, the π^+ and π^- associated with the π^0 in the ω^0 decay.

cause of shower	> 20 GeV			> 60 GeV		
	preselection	Cal Cuts	Isolation	preselection	Cal Cuts	Isolation
π^0	2,705 (22.5%)	266 (81.1%)	148 (81.8%)	538 (10.7%)	52 (88.1%)	25 (92.6%)
$\pi^0\pi^0$	1,114 (9.3%)	1 (0.3%)	0 (0%)	400 (8.0%)	0 (0%)	0 (0%)
η, ω	741 (6.2%)	40 (12.2%)	21 (11.6%)	194 (3.8%)	5 (8.5%)	1 (3.7%)
multiple particles	5,802 (48.3%)	7 (2.1%)	2 (1.1%)	3649 (72.2%)	0 (0%)	0 (0%)
single particle	1,652 (13.8%)	14 (4.3%)	10 (5.5%)	271 (5.4%)	2 (3.4%)	1 (3.7%)
cause of shower	> 130 GeV			> 370 GeV		
	preselection	Cal Cuts	Isolation	preselection	Cal Cuts	Isolation
π^0	1,080 (8.1%)	96 (77.4%)	47 (81.0%)	321 (7.6%)	12 (50.0%)	3 (60.0%)
$\pi^0\pi^0$	785 (5.9%)	4 (3.2%)	1 (1.7%)	220 (5.2%)	3 (13.0%)	0 (0%)
η, ω	377 (2.8%)	15 (12.1%)	7 (12.1%)	129 (3.1%)	3 (13.0%)	1 (20.00%)
multiple particles	10,774 (80.8%)	7 (5.6%)	2 (3.5%)	3,489 (82.8%)	4 (24.0%)	0 (0%)
single particle	324 (2.4%)	2 (1.6%)	1 (1.7%)	54 (1.3%)	0 (0%)	1 (20%)

Table 5.11: Analysis of background events passing the incremental identification cuts. The cause of a reconstructed photon has been found when $> 80\%$ of the detected energy has been found in the MC truth particles.

With such a high proportion of background events coming from a single source, namely the fragmentation of a parton into a π^0, the rejection rates are highly dependent upon the accurate measurement and simulation of these fragmentation functions. Fragmenting partons were identified by matching the identified π^0 to the highest energy parton within a cone of $\Delta R = 0.4$. For background events passing the calorimeter cuts, a typical fraction of the parton energy carried away by

the π^0 (z) is around 0.7 for non-isolated cases and between 0.8 - 0.85 for isolated cases. These fractions appear to be more or less independent of energy. Results from LEP (e^+e^-) provide the bulk of the data constraining these fragmentation functions, with data existing with a reasonable degree of accuracy out to around $z = 0.7$ [76, 79]. Quark fragmentation functions according to the authors of [76] are better constrained than the gluon and since the majority of leading isolated π^0s originate from quark initiated jets, rejections obtained for the non-isolated case should not be overly sensitive to the choice of fragmentation function. Less data are available in the region probed in the isolated case (z = 0.8 - 0.85) and it is likely that the error associated with this rejection is larger as a result.

5.10 Comparison to 'isEM'

In the ATLAS reconstruction software a standard photon identification flag already exists: 'isEM'. This is applied to all candidate photons and details their properties against standard identification cuts similar to those outlined in sections 5.4.1- 5.4.3. Optimisation for this flag was largely based on the results of [74] and has its primary focus in the photon E_T range, 20-100 GeV. The 'isEM' flag has no E_T dependent identification but has been optimised for the 5 η ranges discussed in section 5.5; the optimised value of its cuts are shown in table 5.12. Rejections obtained using the four E_T samples together with corresponding efficiencies for photons are shown in table 5.13. Table 5.14 shows a comparison of 'isEM' with the optimised calorimeter cuts detailed in section 5.8.3. 'isEM' photon efficiencies are constant over the entire E_T range and considerably higher that those obtained before. This is reflected in the reduced values for jet rejection obtained with the flag, which increase from 1,200 to around 3,000 at 100 GeV, figure 5.17. These values are somewhat below those obtained above and in [74, 77], principally because the 'isEM' identification criteria are less harsh than those used in this analyses. The high photon efficiencies are a good indication that there is scope for further optimisation of this flag, as borne out

by the results of section 5.8.3.

Variable	$\|\eta\| \leq 0.8$	$0.8 < \|\eta\| \leq 1.5$	$1.5 < \|\eta\| \leq 1.8$	$1.8 < \|\eta\| \leq 2.0$	$2.0 < \|\eta\| \leq 2.4$
Hadronic Leakage	3	0.008	0.03	0.02	0.015
$E_{237/277}$	0.915	0.91	0.89	0.92	0.91
$\omega_{\eta 2}$	0.012	0.012	0.012	0.0115	0.0125
$\omega_{3strips}$	0.75	0.75	0.8	0.7	0.6
ω_{tot1}	2.7	3.5	3.5	2.0	1.4
$fracs1$	0.35	0.6	0.68	0.3	0.2
E_{max2}	0.25	0.5	1.1	0.40	0.3
ΔE	150.	150.	350.	200.	150.

Table 5.12: Photon identification cuts used in the 'isEM' flag.

Sample	rejection factors		efficiency	
(GeV)	pre sampler	'IsEM' Cuts	single γ	direct γ
20	71.3± 0.7	1,200 ± 45	96.7 ± 0.6 %	92.9 ± 1.5 %
60	70.7± 1.0	2,138 ± 165	97.3 ± 1.7 %	95.1 ± 5.0 %
130	73.1± 0.6	3,175 ± 181	97.4 ± 1.3 %	95.3 ± 1.9 %
370	66.7± 1.0	2,811 ± 281	96.8 ± 1.3 %	94.3 ± 1.7 %

Table 5.13: Jet rejections obtained using the 'isEM' identification flag. Efficiencies shown are for single photons and direct photons.

5.11 The Effect of Pileup

Pileup is the term used to describe the situation where multiple events super-impose themselves on the event of interest. By far the largest cross-section at the LHC will be that of inelastic, non-diffractive pp scattering and is expected to be ≈ 70 mb. At this rate around ≈ 2 such minimum bias events are expected to be present in any one bunch crossing at low luminosity ($\approx 10^{33}\text{cm}^{-2}\text{s}^{-1}$), rising to around ≈ 23 minimum

Sample	rejection factors		single γ efficiency	
(GeV)	'isEM' Cuts	Optimised Calo Cuts	'isEM'	Optimised Calo Cuts
20	1,200 ± 45	2,611 ± 144	92.9 ± 1.5 %	91.2 ± 0.8%
60	2,138 ± 165	6,052 ± 788	95.1 ± 5.0 %	90.5 ± 1.5%
130	3,175 ± 181	7,860 ± 706	95.3 ± 1.9 %	90.8 ± 1.2%
370	2,811 ± 281	12,773 ± 2,391	94.3 ± 1.7 %	90.4 ± 1.2%

Table 5.14: A comparison of jet rejection and single photon efficiencies obtained using the 'isEM' identification flag and the optimised calorimeter cuts of table 5.8.

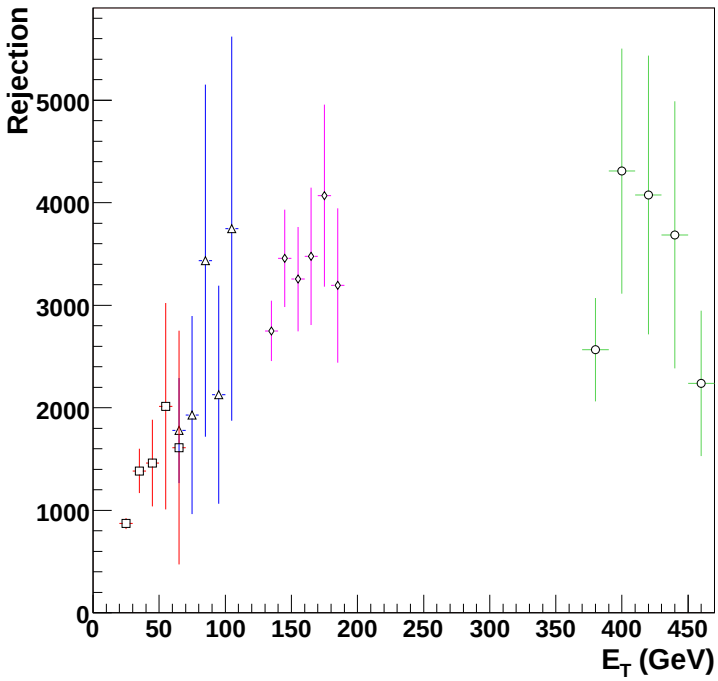

Figure 5.17: Rejection obtained using the standard cuts present in the 'isEM' flag.

bias events at high luminosity, ($\approx 10^{34} cm^{-2} s^{-1}$). The effect of these events will vary across the ATLAS subdetectors depending on the properties of each system. Readout from the pixels and SCT is fast enough that only minimum bias events from bunch crossing 0 (the one of interest) need be considered. The calorimeter's response is slower and consideration must be given to a number of events before and after bunch crossing 0. Further details of these issues can be found in [22, 78].

The effect on the photon calorimeter identification of low luminosity pileup is comparatively modest. At 20 GeV distributions used in the rejection of the QCD background show only a slight broadening due to the additional activity of minimum bias events, as shown in figure 5.18. This reduces the single photon efficiencies quoted in table 5.4 to a value before isolation of 79%. Since this broadening effect will also be seen in the background events, the most likely effect is a small increase in the rejection as well, albeit for a much lower photon efficiency. It should be noted that the studies referred to in section 5.8 optimised identification cuts to a photon efficiency of $\approx 80\%$. This is smaller that the 90% photon efficiency the results of table 5.9 were optimised to, but is of the same order as the effect of including pileup; $\approx 10\%$. As a result, the rejections quoted in table 5.9 are probably obtainable in the low luminosity environment, albeit with a photon efficiency of $\approx 80\%$. The effect of minimum bias events in calorimeter performance is expected to decrease with increasing photon E_T since the energy of these events remains fixed. As such the effect of pileup is expected to be small for energies beyond 100 GeV.

The effect of the isolation cut at low energies is more pronounced, as shown in figure 5.19. As would be expected, the effect increases as the isolation cone size increases, with more activity from the minimum bias events being associated with the photon. For the 20 GeV isolation cut shown in table 5.8 the effect is to reduce the single photon efficiency to 54%. This is clearly not optimal, and the isolation cut would need to be retuned for the case where pile-up was included. This has indeed been done in the previous studies which show isolated rejections $\approx 20\%$ below those

quoted in table 5.9. Again the effect from the minimum bias events is expected to decrease with E_T and is probably small past 100 GeV, although confirmation of this is obscured by the low statistics of the pileup comparison present in [76].

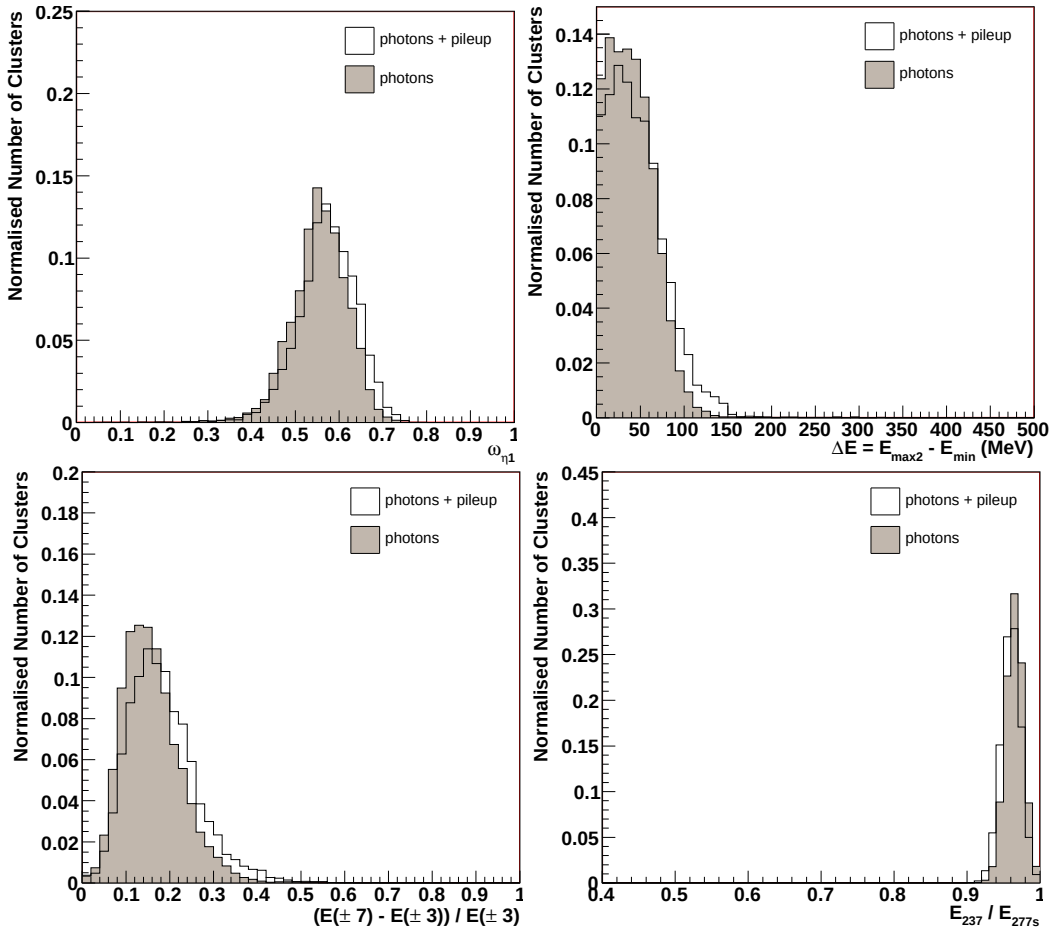

Figure 5.18: A selection of $E_T \approx 20$ GeV single photon identification distributions with and without low luminosity pileup.

5.12 Conclusion

Photon identification has been studied over the E_T range 20 - 450 GeV and efficiencies of $\approx 90\%$ have been obtained for single photons in the absence of an underlying event and pileup. Direct photon efficiencies increase with E_T due to reduction in

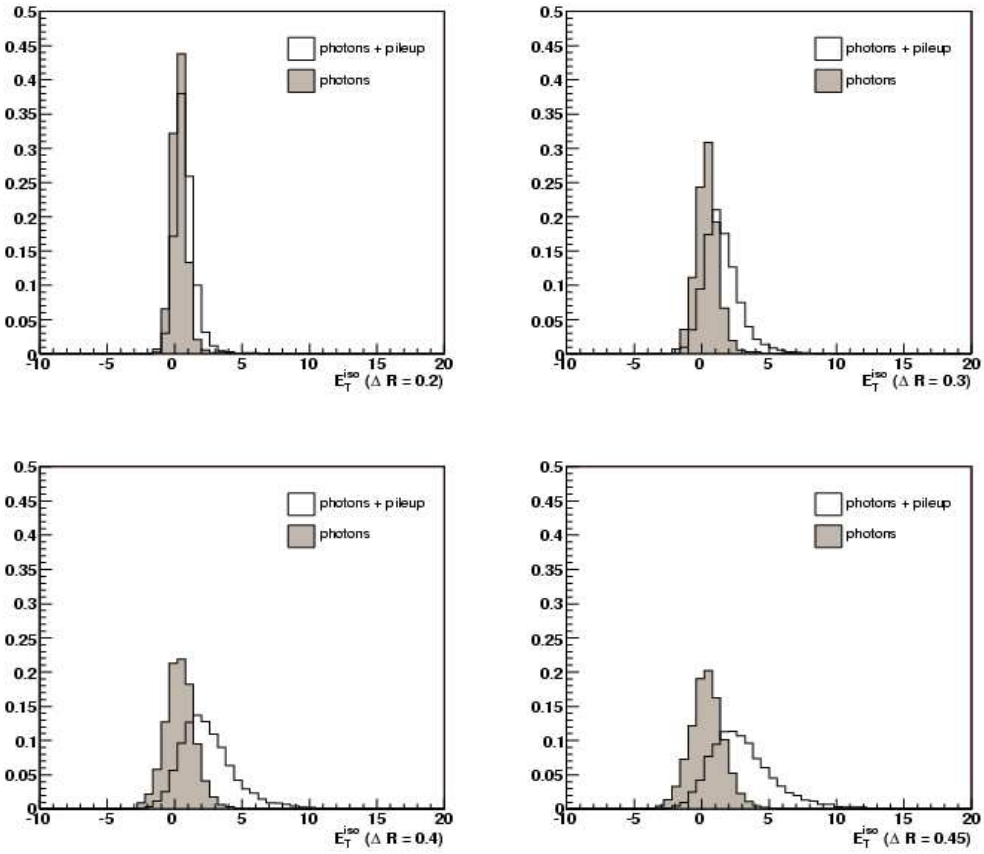

Figure 5.19: The energy deposited inside various isolation cones ($\Delta R = 0.2, 0.3, 0.4, 0.45$) surrounding a $E_T \approx 20$ GeV single photon. The plots illustrate photons with and without low luminosity pileup.

importance of the underlying event. Using the optimised calorimeter cuts a rejection of QCD jets of 2,600 can be obtained at $E_T > 20$ GeV rising to 12,700 at $E_T > 370$ GeV. The addition of an isolation cut increases this rejection to 4,700 at $E_T > 20$ GeV and to 61,000 at $E_T > 370$ GeV. Due to a lack of statistics significant uncertainty is associated with this high E_T isolated rejection and the upward trend at such energies is unclear. The effects of pileup have been considered, and whilst its inclusion is likely to lead to a reduction in the rejection at low energy, its effects on the high energy rejection are likely to be negligible. Therefore, it can be concluded that the detector is expected to have excellent photon identification well into the high E_T region.

Chapter 6

Cross Section Measurement

6.1 Introduction

In this chapter the possibility of performing a direct photon cross section measurement is discussed. The chapter starts with an overview of the likely event rates at the LHC. Next, expected signal to background ratios are presented, together with possible ways of measuring and verifying this quantity. A brief overview of experimental considerations is given before a short discussion on systematics.

6.2 Event Rate Expectations

A direct photon cross section measurement consists of recording the number of signal events (N_{signal}) in given p_T and η bins. It is calculated according to

$$\frac{d\sigma^2}{dp_T d\eta} = \frac{N_{signal}}{A \cdot \epsilon \cdot \Delta p_T \cdot \Delta\eta \cdot \int \mathcal{L}} \tag{6.1}$$

where N_{signal} is to be extracted from the total number of observed events. $A \cdot \epsilon$

is the acceptance multiplied by the efficiency; this compensates for the number of events lost due to the design of the detector and the identification cuts used. $\int \mathcal{L}$ is the integrated luminosity corresponding to the analysed sample.

Expected event rates predicted by the leading order event generator Pythia are shown in table 6.1. The rates correspond to 10 fb^{-1} of data and would take approximately one year at low luminosity (10^{33} cm^{-2}s^{-1}) or about one month at high luminosity (10^{34} cm^{-2}s^{-1}) to acquire. Significant numbers of events are expected in the low and mid E_T regions. Such event rates mean that at low E_T primary consideration can be given to accurately determining N_{signal} and its associated efficiencies, even at the loss of a significant fraction of the signal. For high E_T bins, due to the reduced signal, it will be important to preserve these events and this will probably mean the analysis being optimised separately for these ranges.

Rates calculated using LO generators necessarily exclude the effects of higher order terms. An indication of these effects can shown by looking at the dependence of the cross section on the renormalisation scale (μ). Figure 6.1 shows this variation as a function of E_T for a choice of two scales in comparison with the standard setting of $\mu = p_T$. The inclusion of the next to leading order (NLO) term should reduce this dependency; indeed this would be completely removed if all higher order terms were included.

Where the NLO terms can be calculated, differences to the LO cross section can be summarised by so called K-factors. These are defined as the ratio of the NLO and LO cross section for a given E_T. For direct photons in the E_T range of interest, these K-factors vary between 1.5 and 2.0 [36], as shown in figure 6.2. They demonstrate that the event rates at the LHC are likely to be in excess of those detailed in table 6.1.

E_T (GeV)	N_{signal} (100%)	E_T (GeV)	N_{signal} (100%)	E_T (GeV)	N_{signal} (100%)	E_T (GeV)	N_{signal} (100%)	E_T (GeV)	N_{signal} (100%)
0-10	-	100-110	1.98×10^6	200-210	9.26×10^4	300-310	1.32×10^4	400-410	3.07×10^3
10-20	7.42×10^9	110-120	1.26×10^6	210-220	7.63×10^4	310-320	1.15×10^4	410-420	2.69×10^3
20-30	8.67×10^8	120-130	8.54×10^5	220-230	5.75×10^4	320-330	9.82×10^3	420-430	2.32×10^3
30-40	2.17×10^8	130-140	6.20×10^5	230-240	4.72×10^4	330-340	8.29×10^3	430-440	2.09×10^3
40-50	7.36×10^7	140-150	4.52×10^5	240-250	3.90×10^4	340-350	7.13×10^3	440-450	1.77×10^3
50-60	3.21×10^7	150-160	3.31×10^5	250-260	3.18×10^4	350-360	6.02×10^3	450-460	1.70×10^3
60-70	1.54×10^7	160-170	2.52×10^5	260-270	2.63×10^4	360-370	5.24×10^3	460-470	1.43×10^3
70-80	8.26×10^6	170-180	1.91×10^5	270-280	2.19×10^4	370-380	4.62×10^3	470-480	1.24×10^3
80-90	4.93×10^6	180-190	1.50×10^5	280-290	1.89×10^4	380-390	4.01×10^3	480-490	1.15×10^3
90-100	3.02×10^6	190-200	1.15×10^5	290-300	1.53×10^4	390-400	3.55×10^3	490-500	1.09×10^3

Table 6.1: Expected events rates for direct photons with 10 fb^{-1} *of luminosity. Only leading order (LO) processes are considered (Pythia 6.228) with* $|\eta_\gamma| < 2.5$. *No correction has been made for acceptances or expected efficiencies.*

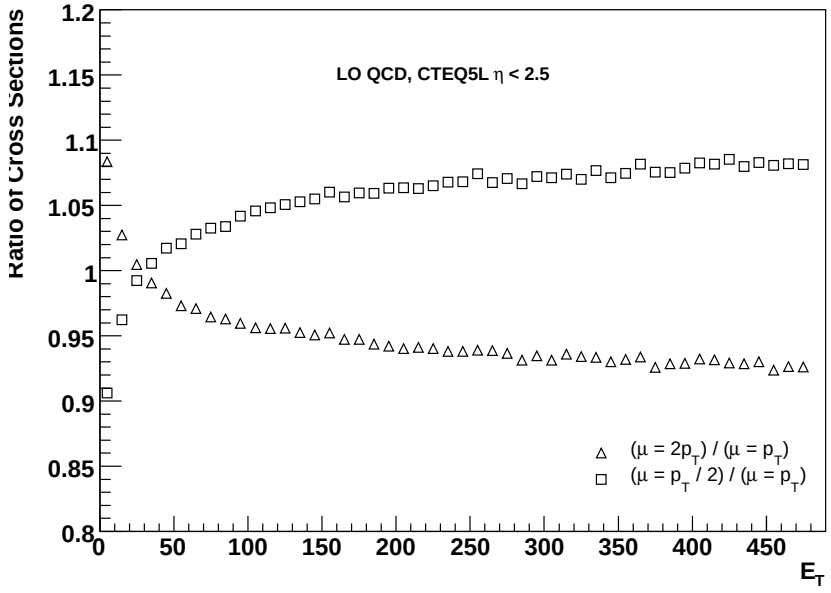

Figure 6.1: Ratio of cross sections obtained using the Pythia LO Monte Carlo generator for two choices of scales, $\mu = 2p_T$ *and* $\mu = p_T/2$. *Both cross sections have been normalised to the standard choice of scale,* $\mu = p_T$.

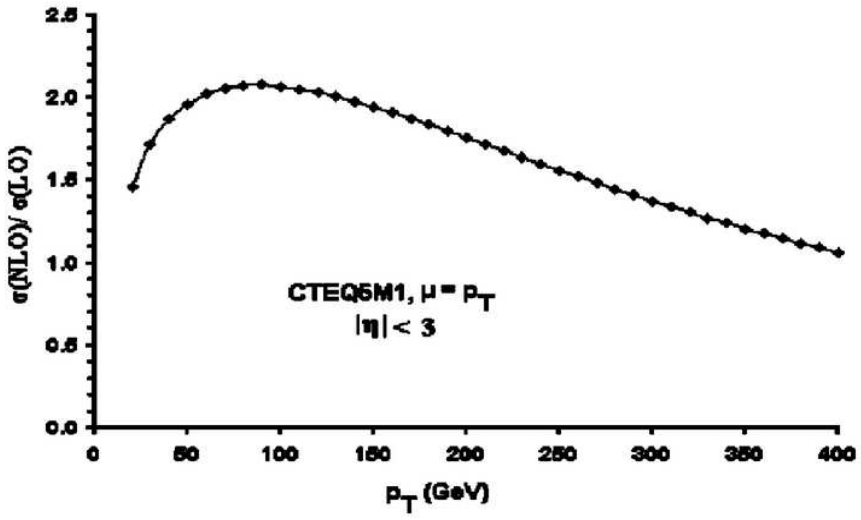

Figure 6.2: K-factors for the direct photon cross section at the LHC. The plot has been taken from [36] and uses the LO generator Pythia and NLO calculations based on [80].

6.3 Signal to Background

As seen in section 5.9 the most significant background to direct photons will be that of light mesons. Particles such as the π^0 and η have high cross sections and decay almost instantaneously into photons with $\pi^0 \rightarrow \gamma\gamma$ (98.8%) and $\eta \rightarrow \gamma\gamma$ (39.4%). Using the rejection rates and identification criteria outlined in chapter 5, a signal to background ratio for direct photons can be calculated. This shows the relative sizes of the expected direct photon signal and the fraction of backgrounds that pass the photon identification cuts. Backgrounds considered are shown in table 5.2. Results are shown in figure 6.3. This signal includes the irreducible bremsstrahlung photon that cannot be distinguished from the true direct photon, as discussed in section 4.2.2. Efficiencies for these two types of photons are shown in figure 5.11 and in tables 5.5 and 5.6. They essentially demonstrate that good direct photon efficiencies can be obtained at all energies and that bremsstrahlung photon efficiencies

reduce with E_T. Figure 6.3 shows the signal to background for both non-isolated and isolated photons. Due to the uncertainly relating to the π^0 fragmentation function and to the effect of pileup on the isolation cuts (as discussed in sections 5.9 and 5.11 respectively) the true errors for the isolated signal to background are likely to be larger than those shown. Nevertheless it is reasonable to assume that the isolated case will yield signal to backgrounds of between factor 2 and 4 greater than the non-isolated case.

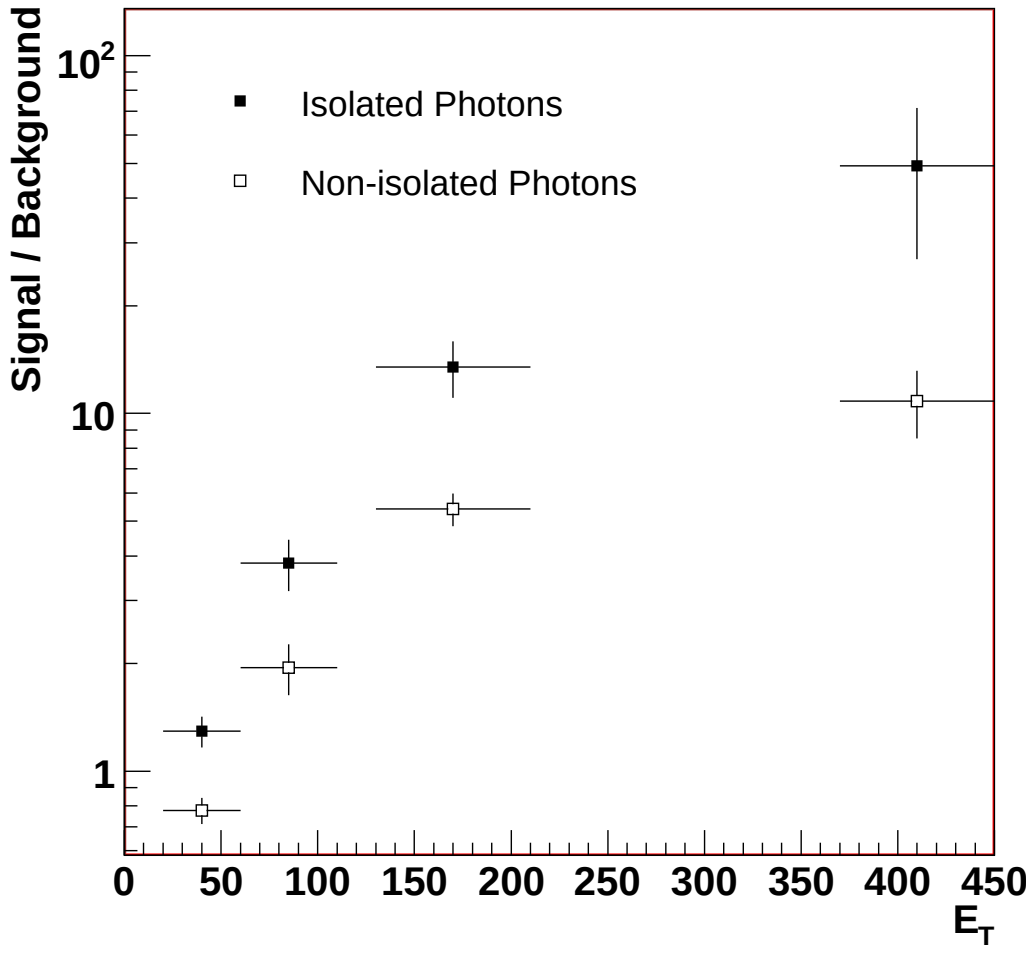

Figure 6.3: Expected signal to background as a function of E_T for direct photons.

6.4 Background Measurement

The ATLAS detector should be able to achieve an isolated signal to background ratio of around unity at 20 GeV rising to in excess of 30 at high E_T. This compares very favourably with ratios achieved in other hadronic collider experiments; ISR (0.05-0.6) [54], UA2 (2.6) [59], D0 (0.4-2) [63] and CDF (0.67-10) [65]. Measurement of this ratio in the running experiment will enable the background component of the photon sample to be estimated and then statistically subtracted to give N_{signal}. Previous experiments, discussed in section 4.4, have used a variety of techniques to do this and two of these methods are explored.

Both methods employ techniques to distinguish multi-gamma final states from those containing a single photon. The profile method looks at the shower profile of candidates and uses a fit to extract the proportion of signal and background events. The conversion method uses the probability of a candidate photon converting before the presampler and relies on the different conversion probabilities found in the signal and background.

6.4.1 Sample Simulation

The Geant4 [25,26] detector simulation was used to model the detector response for both cases. Details of the simulation and of the Rome layout used can be found in section 2.6 and in [69] respectively. The simulation was performed in Athena version 10.0.1 with the final event reconstruction in version 10.0.4.

6.4.2 The Profile Method

The profile method takes advantage of the different shower profiles of photons and light mesons, the principal source of background. At low energies the two photons

from the background are well separated and form wider showers than do single photons. Photon identification rejects events on this basis; however, due to the presence of tails and other features many of these background events are not distinguishable on an event by event basis. By looking at the population as a whole and by comparing it to expectations for pure photons and pure background it should be possible to extract the mixture of these two types of events.

Quantities formed using information from the highly granular first electromagnetic calorimeter will be the most sensitive to the different showers of photons and light mesons. In order to demonstrate the technique the quantity $fracs$, defined in equation 5.4, was chosen to illustrate the potential power of the method. Figure 6.4 shows distributions formed for two samples; pure photons and pure π^0s, the dominant source of background. Standard ATLAS identification 'isEM' (discussed in section 5.10) was required for both photons and π^0s. Since both samples were generated from a single particle gun and are therefore well isolated, no additional isolation was required. At 20 GeV figure 6.4 shows significant differences exist between the two samples. As the energy range increases the opening angle between the two photons of the π^0 will close up and as a result signal photons and π^0s should yield very similar distributions for $E_T > 100$ GeV. For this reason the method will be most useful in the lower E_T region.

A separate sample of photons and π^0s was then prepared, the exact mix of which was unknown at the time of analysis. Figure 6.5 (a) shows the $fracs$ distribution for this sample, together with that of the pure photons and π^0s from figure 6.4. The mix of photons and π^0s was then extracted using the sum of the least squares fit,

$$s = \sum_{bins} \left(\frac{O - E}{\sigma_O} \right)^2 \tag{6.2}$$

where O is the observed value of the $fracs$ distribution in each bin with associated error σ_O and E is the expectation for that value based on a hypothesised mix of

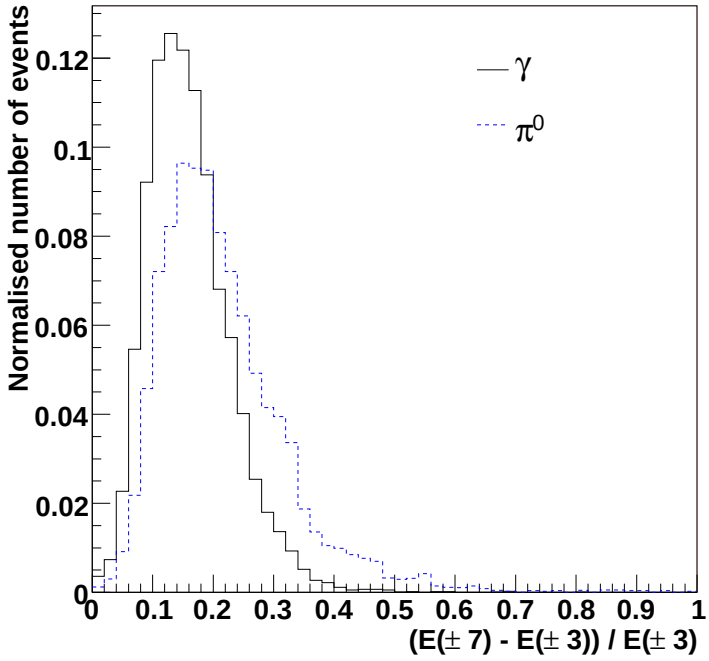

Figure 6.4: Different calorimeter distributions for photons and $\pi^0 s$ with fixed $E_T \approx 20$ GeV. Plotted is the fracs quantity (equation 5.4) formed from the energy deposited in the first electromagnetic calorimeter.

photons and $\pi^0 s$. This fit was then done over a number of hypothesised mixes from all π^0s to all photons. The range of $fracs$ used in the fit was restricted to reduce the effect of tails and low statistics bins. The photon purity, defined as the number of photons divided by the total sample, is then extracted via the minimisation of s as shown in figure 6.5 (b). Table 6.2 shows this minimum value and extracted photon purity for a number of fit ranges. Expected values of s, based on a χ^2 per degree of freedom, were 12, 17 and 9 for the three fit ranges considered. The measured values of s are all lower than these values, but nevertheless, indicate a reasonable fit has been made. True purity, looked up after the analysis, was 72.8% and compares very favourably with that obtained from the fit.

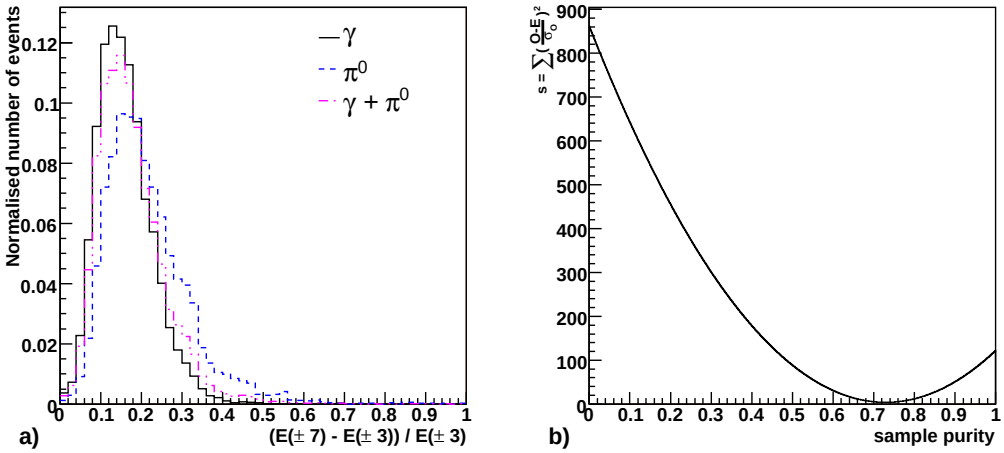

Figure 6.5: (a) Different calorimeter distributions for three samples with fixed $E_T \approx 20$ GeV. Plotted is the $fracs$ quantity (equation 5.4) formed from the energy deposited in the first electromagnetic calorimeter. (b) Fit to extract the photon purity using the profile method.

Experimental Considerations

The principal issues for this measurement will be the accurate modelling of electromagnetic showers and the feasibility of cross checking the shower simulation with

Fit Range to $fracs$	s	extracted Purity
0.02 - 0.3	4.42	72.3%
0.02 - 0.4	3.44	72.2%
0.1 - 0.3	3.86	73.0%

Table 6.2: Extracted photon purity for a sample of $E_T \approx 20$ GeV photons and π^0s. An estimate of the size of the error associated with the extracted purity is shown by varying the range the fit is performed over. This gives an error of $\pm 1\%$. The true purity, looked up after the analysis, was 72.8%.

experimental data. The availability of highly pure samples of photons and π^0s would greatly enhance the reliability of this method since the errors associated with the shower model are likely to be a significant contribution to the background estimation systematics and hence the cross section measurement. In the above analysis π^0s were the only form of background considered. Other sources and their relative abundances need to be understood since they will have a direct effect on the observed shower shape and hence the effectiveness of the fit. Since all of these factors are also relevant to the conversion method they are discussed in more detail in section 6.4.4.

6.4.3 The Conversion Method

Photons converting before the calorimeters will deposit a fraction of their energy in the presampler. This liquid argon calorimeter is described in more detail in section 2.4.2 and also in [23, 81]. It covers the range $|\eta| < 1.8$ with a uniformly granular cell size of $\Delta\eta \times \Delta\phi = 0.025 \times 0.1$. As shown in figure 2.6 it is situated after the cold wall just before the first electromagnetic calorimeter. Two standard quantities are formed from these cells; the energy deposited in a single cell ($e011$), and the energy deposited in a group of nine (3x3) cells ($e033$). In both cases the cell(s) are centred on the electromagnetic shower as measured by a sliding window

algorithm, as detailed in section 5.3, running over the sum of all energy deposits in the electromagnetic calorimeters.

The material profile of the ATLAS detector can be seen in figure 5.6. The large amount of material present means a significant number of photons will convert before reaching the presampler. The probability of a photon converting (ϵ_γ) is given approximately by,

$$\epsilon_\gamma = 1 - exp(-7t/9) \tag{6.3}$$

where t is the amount of material traversed in radiation lengths, X_0. The majority of the background remaining after the identification cuts described in section 5.4 will come from the decay of light mesons into two narrowly separated photons. In comparison with the single photon signal, these background events should have a higher probability of containing at least one converted photon. If the background is assumed to consist entirely of two photon final states, then the conversion probability (ϵ_b) is related to the single photon conversion probability (ϵ_γ) via

$$\epsilon_b = 2\epsilon_\gamma - \epsilon_\gamma^2 \tag{6.4}$$

The number of signal photons (N_γ) is then given by

$$N_\gamma = \frac{\epsilon - \epsilon_b}{\epsilon_\gamma - \epsilon_b} N \tag{6.5}$$

where N is the number of photons in the analysed sample and ϵ is the conversion probability for those photons.

Background events used in the demonstration of the conversion method were assumed to come solely from π^0s and were generated as described in section 6.4.1.

Presampler Noise and Event Pileup

To determine whether a signal observed in the presampler was the result of a photon conversion, the noise present in that region needs to be understood. It is the signal over and above the background noise that is then used to determine the number of events containing a conversion. An estimate of the noise was obtained by randomly selecting presampler cells and plotting the distribution of the observed energy as shown in figure 6.6 (a). The effect of low luminosity pileup can be seen in figure 6.6 (b) and broadens this distribution only slightly. As a result it will not be considered further. The rms noise was found to be approximately 56 MeV for a single cell and adding the noise from nine such cells in quadrature yields an estimate for the noise in a 3x3 region. Coherent noise effects are ignored by this approach and for this reason the result is likely to be an underestimation.

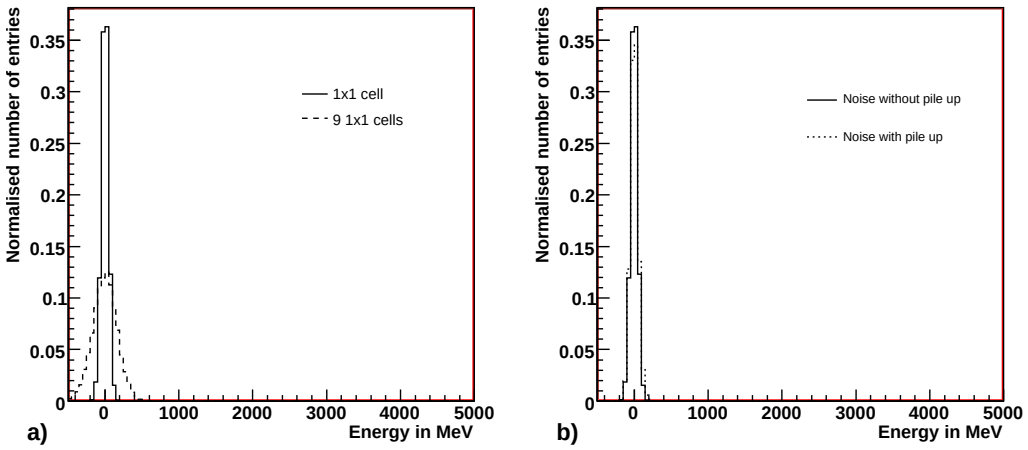

Figure 6.6: Simulated noise in the presampler. (a) The noise distribution for a single presampler cell together with nine random cells added in quadrature. The rms noise for a single cell was found to be 56 MeV. (b) The effect of adding low luminosity pileup.

Conversion Probabilities for π^0s and γs

The higher π^0 conversion probability can be seen in figure 6.7. For three different samples, 20, 60 and 130 GeV the amount of energy deposited in the presampler is shown for $e011$ and $e033$. The conversion probability was obtained by using a cut $\approx 3\sigma$ above the noise measured in figure 6.6; at 150 MeV for the one cell energy measurement and 450 MeV for the 3x3 cell energy measurement. Events containing energy above this cut were classified as converted events, below, unconverted events. Table 6.3 shows values of the conversion probabilities ϵ_γ and ϵ_{π^0}. $e011$ and $e033$ are consistent with one another and as a result either quantity may be used the extract the signal.

E_T	e011		e033	
(GeV)	ϵ_γ	ϵ_{π^0}	ϵ_γ	ϵ_{π^0}
20	0.70	0.81	0.69	0.83
60	0.71	0.87	0.72	0.89
130	0.76	0.90	0.76	0.90

Table 6.3: Calculated values for the conversion probabilities ϵ_γ and ϵ_{π^0} using the energy deposited in a single presampler cell ($e011$) and a group of nine presampler cells ($e033$).

Extracting the Signal from the Background

Using the conversion rates for photons and π^0s, a dummy analysis was performed to extract the photon signal from a mix of signal and background. A separate Monte Carlo sample was produced at 20 GeV containing an unknown proportion of photons and π^0s. These were generated using the same detector description and releases as in the previous study. Photons and π^0s were required to pass the standard ATLAS photon identification criteria 'isEM'. No isolation cuts were required since

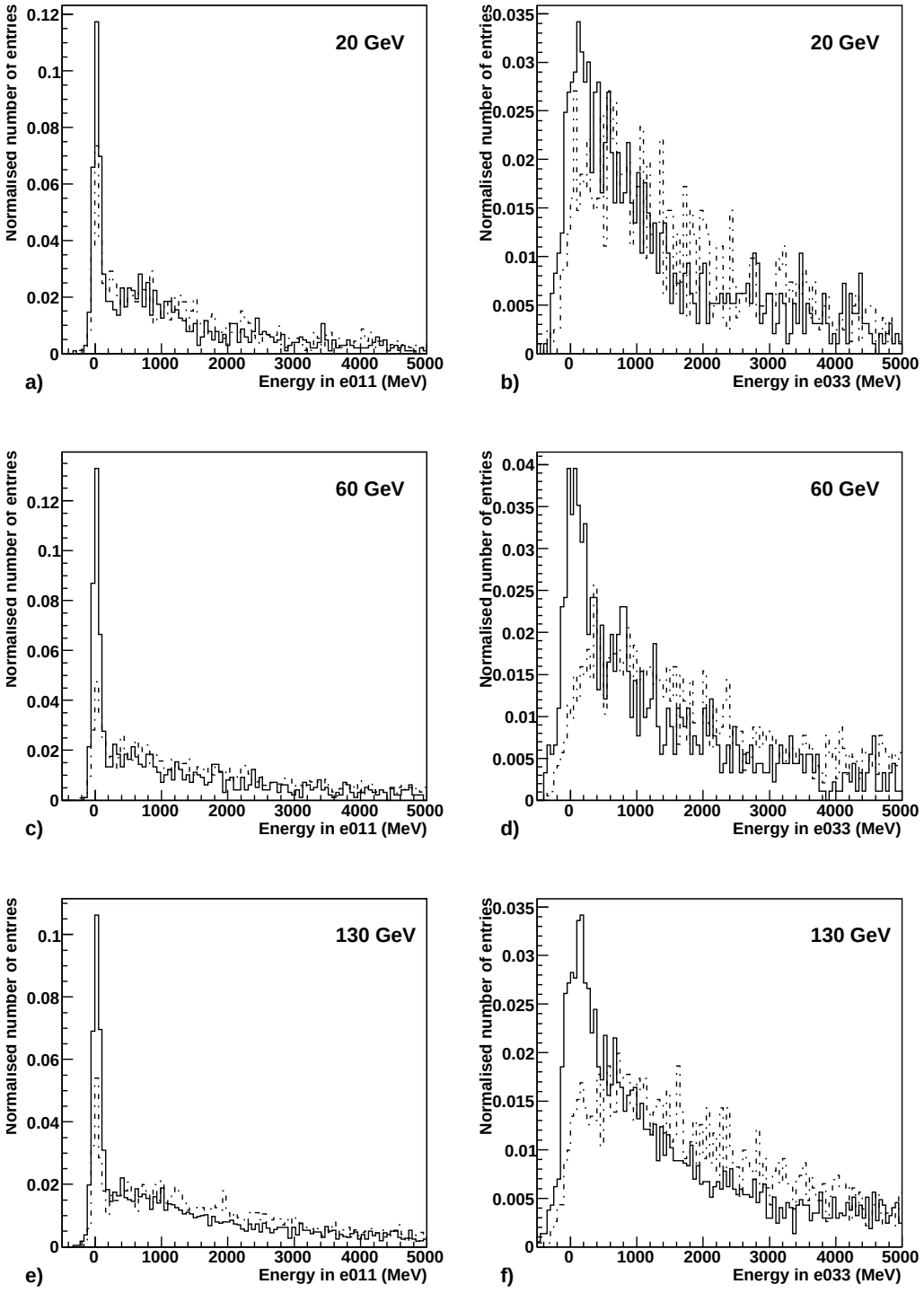

Figure 6.7: Energy deposited in the presampler for photons (solid line) and π^0 (dotted line). The photons and π^0s were generated using a single particle gun. Plots on left show the energy in a single presampler cell in front of the main shower and on the right the energy in 3x3 cells, again centred on the main shower. Events from a π^0 shower have on average a higher probability of conversion.

both samples were generated with a single particle gun and should be well isolated. Measured energy deposits in the presampler are show in figure 6.8, the corresponding conversion rates are shown together with the extracted signal (N_{signal}) and true signal (N_γ) in table 6.4. N_{signal} was calculated using equation 6.5 and the conversion probabilities ϵ_γ and ϵ_{π^0} shown in table 6.3.

The number of signal photons was calculated to be $11,359 \pm 568$ using $e011$ and $11,349 \pm 523$ using $e033$. As expected the two measurements are consistent with each other since they measure the same events. These values are also consistent with the true number of photons used in the study (10,819), revealed after the calculations were made. The successful recovery of N_γ demonstrates that the method could be useful in verifying the signal contamination after photon identification. Additionally, since this method relies on the conversion probability and is independent of the opening angle of the photons coming from the π^0, the method should be equally effective in the high E_T region. The overlap in the low E_T region provided by the profile method will also allow these two independent methods to be cross checked against each other.

Calorimeter quantity	20 GeV			
	ϵ	Cal Purity	N_{signal}	N_γ (actual)
$e011$	0.750	72.80%	$11,369 \pm 568$	10,819
$e033$	0.731	72.67%	$11,349 \pm 523$	10,819

Table 6.4: Measured values for ϵ for a random mix of photons and π^0. N_{signal} was calculated using equation 6.5 and the conversion probabilities shown in table 6.3. Errors are statistical in nature and include the compound errors of ϵ_γ, ϵ_{π^0} and ϵ.

Experimental Considerations

Key for the successful use of the conversion method will be the determination of the ϵ_γ and ϵ_{π^0}. Any error in these conversion probabilities will have a direct effect on

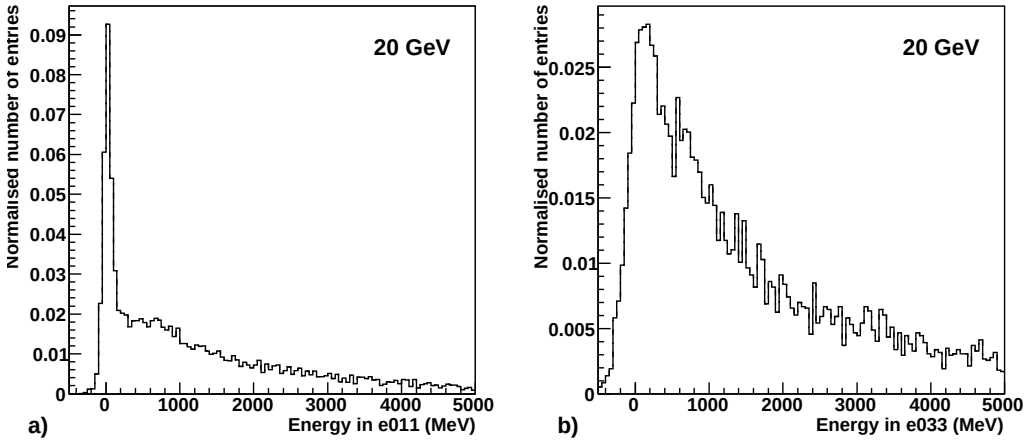

Figure 6.8: Energy deposited in the presampler for a mixture of photons and π^0s. a) the energy in a single presampler cell ($e011$) in front of the electromagnetic shower. b) the energy in a group of nine ($e033$) cells in front of the electromagnetic shower.

N_{signal} and hence the cross section measurement.

As the photon energy is increased the expected signal to background should also increase (figure 6.3) and as a result at 400 GeV a purity of up to 98% may be expected. With such a high purity further background subtraction may not yield significant improvements in the cross section measurement given the other associated experimental errors. Nonetheless, in such a situation the method could still play an important role in verifying this very high purity. Again the accurate modelling, especially of ϵ_γ will be vital.

6.4.4 Experimental Issues

In describing both the profile and conversion methods the background has been approximated to events containing single, isolated, π^0s. Table 5.11 shows that π^0s account for the vast majority of background events, but that nevertheless a total contribution of around 10% can be expected from η, ω and other particles. The

most common type of these other backgrounds are η and for decays $\eta \rightarrow \gamma\gamma$ (BR = 39.4%) the above methods should be equally valid. However, contributions from other decay modes and from other particle sources will need to be considered if both methods are to be used effectively.

Both the profile and conversion methods rely on the accurate simulation of photons and π^0s. It will therefore be useful to cross check the simulation with experimental data, verifying the accuracy of the showering and conversion model. For this purpose $Z \rightarrow ee$ events will be valuable since they should provide a clean source of electrons. Photons convert into electron-positron pairs in the first stage of showering and hence should contain a degree of similarity with showers originating from electrons. By comparing the expected shower profiles for electrons to those observed from $Z \rightarrow ee$ events, a cross check on the electron showering model may be obtained.

Further verification of the showering model as well as the conversion rates could be achieved if pure samples of photons and π^0 were obtained. In the hadronic environment at the LHC this could prove challenging. Nevertheless there are a number of promising methods. Samples of π^0s could be obtained by using the first electromagnetic calorimeter to look for two well separate peaks of energy characteristic of a π^0 decay. This method would have a limited energy range since the photons from high E_T π^0s have small opening angles.

A pure source of photons could be obtained by looking at radiative Z decays. These are Z events that decay to two electrons, one of which then emits a single hard photon. Forming the invariant mass of the two observed electrons and by requiring this mass to be well below the Z resonance, a search is then made for an isolated photon. If present, this is then added to the invariant mass of the electron pair to recover the Z mass. Events within a window of the Z mass can then be used to give a sample of photons. Since the chance that random particles faking a photon or electron, will also have the correct invariant mass to reconstruct the Z resonance is small, this should yield a sample of highly pure photons.

Figure 6.9 and table 6.5 shows a test in principle of this method. $Z \rightarrow ee$ events were generated with Pythia and simulated in the ATLAS fast detector response program ATLFAST [27]. Apart from the electrons and photons being required to be in the region $|\eta| < 2.5$, no efficiency effects or particle misidentification are included. The invariant mass of the two highest E_T electrons is shown in figure 6.9 (a), the large tail represents those electrons that either radiate photons or that have one of their electrons outside the detector acceptance. Events that had an invariant mass of between 30-70 GeV are then replotted in figure 6.9 (b) with the invariant mass of the two highest E_T electrons and the highest E_T photon shown. The photon was required to have $E_T > 20$ GeV and must be $\Delta R > 0.4$ away from the closest electron. This last requirement ensures that the photon and electrons are well separated and should be visible as distinct objects in the detector. A fit was then made to the peak of the recovered Z mass in the window 88-94 GeV and gives a peak value of 90.8 ± 0.2 GeV. This compares reasonably well to the standard Z mass value of 91.2 GeV [82]. Photons from events in the mass window 87-95 GeV are shown in table 6.5. The numbers have been normalised to 100 fb^{-1} of data which approximates to about one year at high luminosity. Although these events are scarce it should be possible, even after taking detector efficiency into account, to obtain a sample of reasonable size. This sample of pure photons can then be used to cross check the simulation and provide confirmation of the showering model and conversion rates.

A powerful cross check on the conversion and profile methods lies in the potential overlap between the two. At low energies both methods can be expected to perform well and as a result provided the opportunity to compare the signal extracted for each of the methods. Good agreement between these two approaches would be an additional source of validation for the signal.

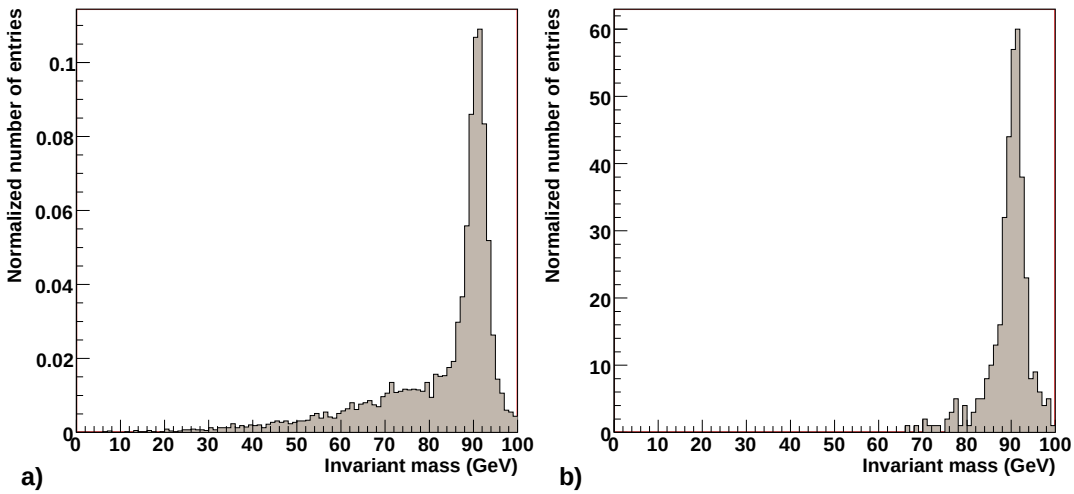

Figure 6.9: (a) Invariant mass formed from the highest E_T electrons in $Z \rightarrow ee$ events. (b) For events in (a) within the invariant mass window 30-70 GeV the invariant mass is plotted for the two highest E_T electrons and the highest E_T photon.

E_T range	Number of Events for 100 fb^{-1}
$20 - 30GeV$	12,200
$30 - 40GeV$	5,800
$40 - 50GeV$	1,400
$50 + GeV$	600

Table 6.5: The number of photons per E_T bin obtained through the reconstruction of radiative Zs. Figures are for 100% electron and photon efficiencies and assume 100 fb^{-1} of data, approximately one year at high luminosity.

6.5 Systematic Errors

Sources of systematic error within the direct photon measurement will be varied and ultimately represent the lack of understanding of the experimental apparatus. Major sources of systematic error are expected to be luminosity measurement, trigger efficiency, energy calibration, background subtraction, vertex determination, acceptance and identification efficiencies. The size of each of these uncertainties will reduce as more data are gathered and will vary as a function of E_T.

• The goal of the ATLAS experiment is to be able to measure luminosity initially to 10% improving to 5% or below as beam conditions and luminosity monitors become better understood.

• Absolute electromagnetic energy scale should be ultimately known to around 1% and the linearity of this scale to around 0.5%. However, when these are convoluted with the falling E_T spectrum of direct photons, it translates into a systematic uncertainty of around 5%. This is comparable with other hadronic collider experiments such as D0 and CDF which have energy scale uncertainties of 3-10% for the direct photon measurement [63, 65].

• Identification and acceptance efficiencies will be limited by the ability to select clean events and model these using Monte Carlo simulations. Experience at the Tevatron suggests that these things may be known to around 5%. However, given ATLAS high statistics and the ability to select preferentially clean events, this precision may be improved.

• Trigger efficiencies are known in D0 and CDF to within 10-5% becoming better known at high energies. The degree to which these efficiencies can be measured in ATLAS will depend on the identification and exploitation of processes that contain redundant triggers. Diphotons, γ-jet events and radiative Zs may all have a part to play in this. The expected event rates of these processes, especially diphotons and

jet-gamma events mean a first estimate of the effect of trigger uncertainties may be $\approx 5\%$.

• Background subtraction provides the other major source of systematic error and given the uncertainty in this, a conservative estimate on its effect on the cross section is 10%. This will vary considerably as a function of E_T, with higher E_T events having a higher purity and as a result a smaller dependence on this factor.

If rates for the above factors are taken into account and if a vertex systematic error similar to D0 and CDF is assumed ($\pm 5\%$), then the effect on the cross section measurement is probably around 15%. It should be emphasised that many of these factors are either first approximations or the ATLAS stated performance goals and as such further work to reinforce this figure is needed. Cross section measurements performed by D0 and CDF have stated systematic uncertainties of 22-15% and 18-11% at respectively low-high E_T. ATLAS should therefore not only be able measure direct photons at higher E_T but do so with a significant improvement in precision.

6.6 Conclusion

The feasibility of a direct photon measurement has been discussed. Significant numbers of events are expected over a large range of E_T with a good signal to background. Two methods of quantifying the main background have been presented and show it should be possible to recover accurately the direct photon signal. Ways of checking these two approaches have also been discussed and of particular importance will be the overlap region between the two. Finally, possible sources of systematics have been discussed, all of which will need to be understood if a competitive direct photon measurement is to be made. Given these factors and performance goals of ATLAS a measurement should be possible at low E_T with about one year of low luminosity data and should surpass the precision of other experiments.

Chapter 7

Constraining the Gluon PDF

7.1 Introduction

The chapter begins with a brief description of the motivation behind the use of direct photons to probe the gluon content of the proton. A recap of the kinematic scattering in the process is presented and this is applied to various parton density functions (PDFs) showing potential regions of interest. These are investigated further using the Pythia Monte Carlo generator and an analysis of the direct photon's sensitivity to the gluon content of the proton is given. Areas of further study are discussed, followed by some experimental considerations.

7.2 Motivation

Many physics signatures at the LHC involve a gluon in the initial state and will require knowledge of its PDF. It is therefore vital for both the understanding and interpretation of these Standard Model processes and the new physics searches, that the contribution from this parton can be accurately described. An example

of interest is the production of a light Higgs in the low mass region (100-200 GeV) via the process $gg \rightarrow H \rightarrow \gamma\gamma$. Current uncertainties in the gluon-gluon luminosity arising from the gluon PDF lead to a production uncertainty of this light Higgs of around $\pm 5\%$ at the LHC [6]. Z, W and γ all have similar uncertainties in their quark-gluon production channels arising from the behaviour of the gluon PDF. In addition, backgrounds to many of these and other processes involve gluons in the initial state and it will therefore be a prerequisite to their accurate estimation that the gluon PDF be understood.

The current constraints on the gluon PDF come from two principal sources, DIS experiments and high E_T jet data from the Tevatron. DIS data precisely determine the quark content of the proton and hence, via the momentum sum rules, the gluon content. Given the vast amount of DIS data available this process places considerable constraints on any PDF fit and is of particular importance in the low to mid x range, $10^{-5} < x < 10^{-1}$ [6]. An example of this is the DIS data used in the CTEQ 4M fit which constrains the total momentum carried by the gluon to be 42% with an uncertainty of 2% [83]. As a result, any increase in the gluon content at any x, requires a reduction at another and places an important restriction on the gluon. The second principal constraint in PDF fits affects the mid to high x region and is provided by the inclusive jet data published by D0 and CDF [16–18]. These experiments measure jets in the range $50 < Q < 500$ GeV and correspond to $0.01 < x < 0.5$. Their inclusion in PDF fits has had the effect of hardening the gluon content in this high x region. Nevertheless, despite recent advances in the precision of both types of constraints, the gluon is still by far the least well constrained parton. Added to this is the opportunity to study the PDF in the new kinematic region opened up at the LHC with events being produced at higher values of Q^2 than ever before. This will allow not only a further test of pQCD but also the DGLAP equations that describe the PDF evolution in Q.

7.3 Scattering Kinematics

As shown in section 4.3 the kinematics of the two body scatter representing the direct photon process can be described as

$$x_a = \frac{x_T}{2}(e^{\eta_c} + e^{\eta_d}) \tag{7.1}$$

$$x_b = \frac{x_T}{2}(e^{-\eta_c} + e^{-\eta_d}) \tag{7.2}$$

where $x_T = 2p_T/\sqrt{s}$ is the transverse momentum fraction probed by the process. Equations 7.1 and 7.2 relate the struck parton's momentum fraction (x_a and x_b) to the kinematic observables p_T, η_c and η_d. p_T is the transverse momentum of the jet or photon (in this naive scatter they will be the same) and η_c and η_d are the pseudorapidity of the jet and photon (or vice versa).

Using PDFs, a probability map of the interaction can be produced. For each point in η_c and η_d the probability of obtaining a γ-jet event can be obtained by using equations 7.1 and 7.2 together with the relative probability of obtaining partons with the corresponding x_a and x_b. It is assumed that the scatter will occur via the Compton process, a gluon-quark interaction, and that the likelihood of obtaining a parton of momentum fraction x is given by the appropriate PDF. Figure 4.3 shows the validity of this first assumption with $> 80\%$ of direct photons in the LHC expected to be produced via the Compton process. Matrix element effects and contributions from initial and final state radiation (ISR / FSR) are ignored in this kinematic approach. In particular, the presence of ISR means that the x probed by the interaction, or indeed the species, may not necessarily be the x from the parton in the proton. However, this approach does represent a first expectation for η distributions in the kinematic region of interest. It can therefore be used to study the sensitivity of direct photons to different PDF sets and provides a convenient starting point for the analysis. Once regions displaying this sensitivity have been

identified, they can be fully explored with a full Monte Carlo simulation.

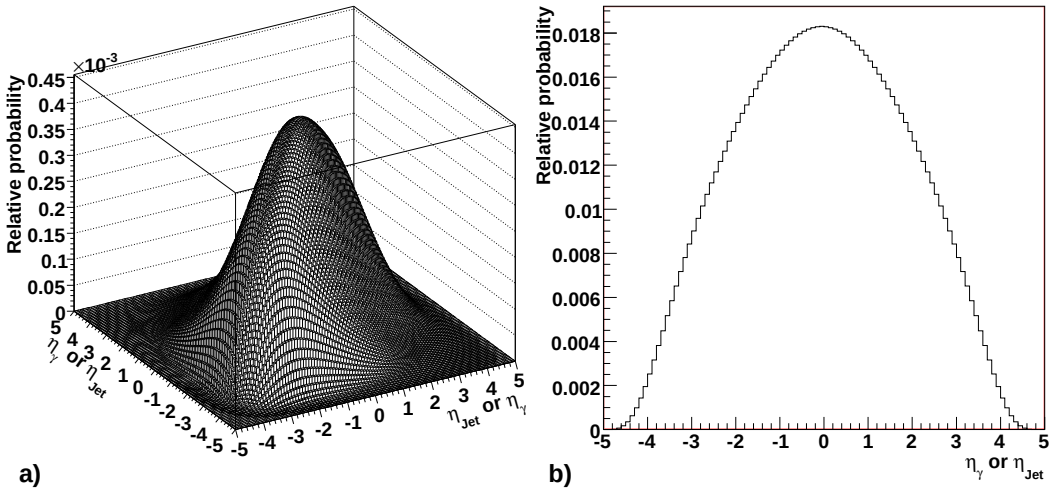

Figure 7.1: Probability map of the η distributions from direct photon events using CTEQ 6M, equations 7.1 and 7.2 with Q=100 GeV.

Figure 7.1 shows the probability map for γ-jet events using the PDFs of CTEQ 6M and equations 7.1 and 7.2. The four momentum transfer (Q) was 100 GeV and translates approximately to the p_T of the outgoing photons and jets. Figure 7.1 (a) shows the relative probability of producing a photon and jet at a specific η_c and η_d, whilst (b) shows the distribution obtained if only one of the outgoing particles is plotted. Since only scattering kinematics have been considered the distributions of the photon and jet are identical. Events are peaked in the central region of the detector and in the majority of cases the photons and jets will be observed in the same η half of the detector.

In this naive model photons and jets are produced at a fixed p_T; 100 GeV in the case of figure 7.1. Previous analysis [36] suggests that the sensitivity to the different parametrisations will be most apparent in the η spectrum of the photon. This will be borne out by figures 7.5 and 7.6 of section 7.4 and for this reason the analysis is primarily focused on these distributions.

7.3.1 Effect of Different PDF Sets

Since different PDF fits describe the same underlying physics, and in many cases use similar data sets, they show distributions comparable to those of figure 7.1. In order to show the differences between the sets, figures 7.2 (a) to (d) show variations relative to one common PDF set, CTEQ 6M [6]. The plots have been restricted to the range $|\eta| < 3.2$ and represent the coverage of the electromagnetic calorimeter where the photon will be observed. On the left are differences in the η distributions from measuring both the jet and photon. In many cases significant variations between the two sets can be seen, for example figure 7.2 (b1) (CTEQ 6M versus ZEUS 2005 ZJ) shows a 15-20% difference diagonally across η. Closer examination, however, reveals that these effects are unlikely to be observed in reality since they come from regions where η_{Jet} and η_{γ} are in opposite sides of the detector. The relative probability of finding these events is shown by considering the appropriate region of figure 7.1 and a full examination using the Pythia Monte Carlo shows that only a couple of events per year would be expected in this region. Plots on the right of figure 7.2 show the expected η distributions from either photons or jets. These distributions, modified by the matrix element effects and ISR / FSR, are expected to be observable in the detector. Differences of between 3-10% can be seen in these distributions and confirm that η_{γ} may be sensitive to the different parametrisation of PDF sets. The plots of figure 7.2 are repeated in figure 7.3 and figure 7.4 for $Q = 100$ GeV and $Q = 300$ GeV and again show differences between the PDF sets. At $Q = 100$ GeV the variation seems to fall to 2-5%, but increases again at $Q = 300$ GeV where they are around 8% for all sets. Again at all energies the most significant variation between sets is diagonally accross $\eta_{\gamma} - \eta_{jet}$, with large variations especially noticeable at $Q = 300$ GeV. However, as before, such effects are unlikely to be observed due to the low numbers of events expected in these regions. Observed variations will instead be most prominent in the projections of η_{γ} and η_{jet}, as shown in the right hand plots of figures 7.3 and 7.4. The absolute size of these amounts are not as important as the fact that differences exit. A full Monte Carlo simulation can be

expected to modify significantly these distributions and it is these new distributions that need to be investigated further.

7.4 Leading Order Differences in PDFs

The Pythia [70] Monte Carlo generator was used to produce direct photon events at leading order (LO). This used the PDF interface LHAPDF [84] and specifically includes the matrix element and ISR/FRS effects absent in section 7.3.1. Data were generated for low p_T (> 30 GeV), mid p_T (> 110 GeV) and high p_T (> 300 GeV), a sample of 5 million events being produced for each data set. This corresponds to approximately 1 fb^{-1}, 10 fb^{-1} and 500 fb^{-1} of luminosity for the respective sets. Distributions shown within figures 7.5 and 7.6 correspond to the same luminosity, with variations in cross sections being seen as relative offsets in the plots. Figure 7.5 shows normalisation differences in the p_T spectrum of photons; these are $\sim 10\%$ at 30 GeV falling to $\sim 7\%$ at 300 GeV and increasing again to $\sim 10\%$ at 600 GeV. Since these are within the anticipated normalisation uncertainty of the experiment such differences are unlikely to be visible in the detector. The analysis has instead been focused on the relative shape of the η distribution, something that should be more visible.

Figure 7.6 shows the difference in the η distributions for a number of different PDF sets. In all cases these distributions have been normalised to that of CTEQ 6M (central value). At $p_T > 30$ GeV the η distribution extends outward to $\eta \approx 5$. However, since the range of the electromagnetic calorimeter is limited, photons can only be detected up to $|\eta| < 3.2$. Differences between sets should still be visible in this range, the H1 and older CTEQ sets especially showing large variations when compared to CTEQ 6M.

As p_T increases the width of the η distribution tightens up and the majority of the events will be visible in the detector. Differences, observed at 30 GeV, are increased

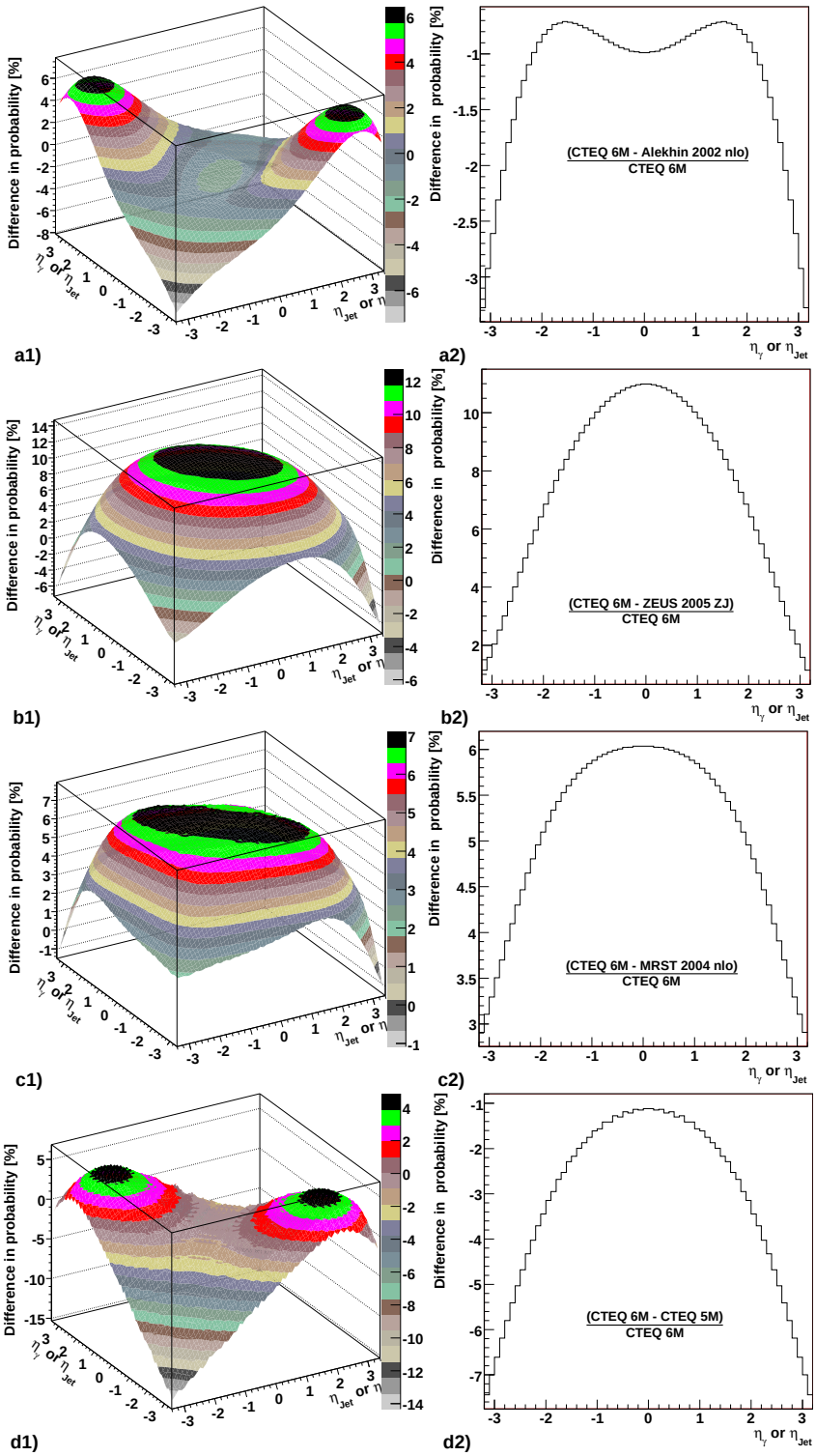

Figure 7.2: Differences in the probability map of η distributions from various PDF sets at Q=20 GeV. On the left are differences in the relative probability of obtaining a photon and jet at given values of η. Probabilities are based on scattering kinematics only; no account has been made of matrix element corrections or initial / final state radiation. On the right hand side differences in the η distribution from observing just one outgoing 'particle'.

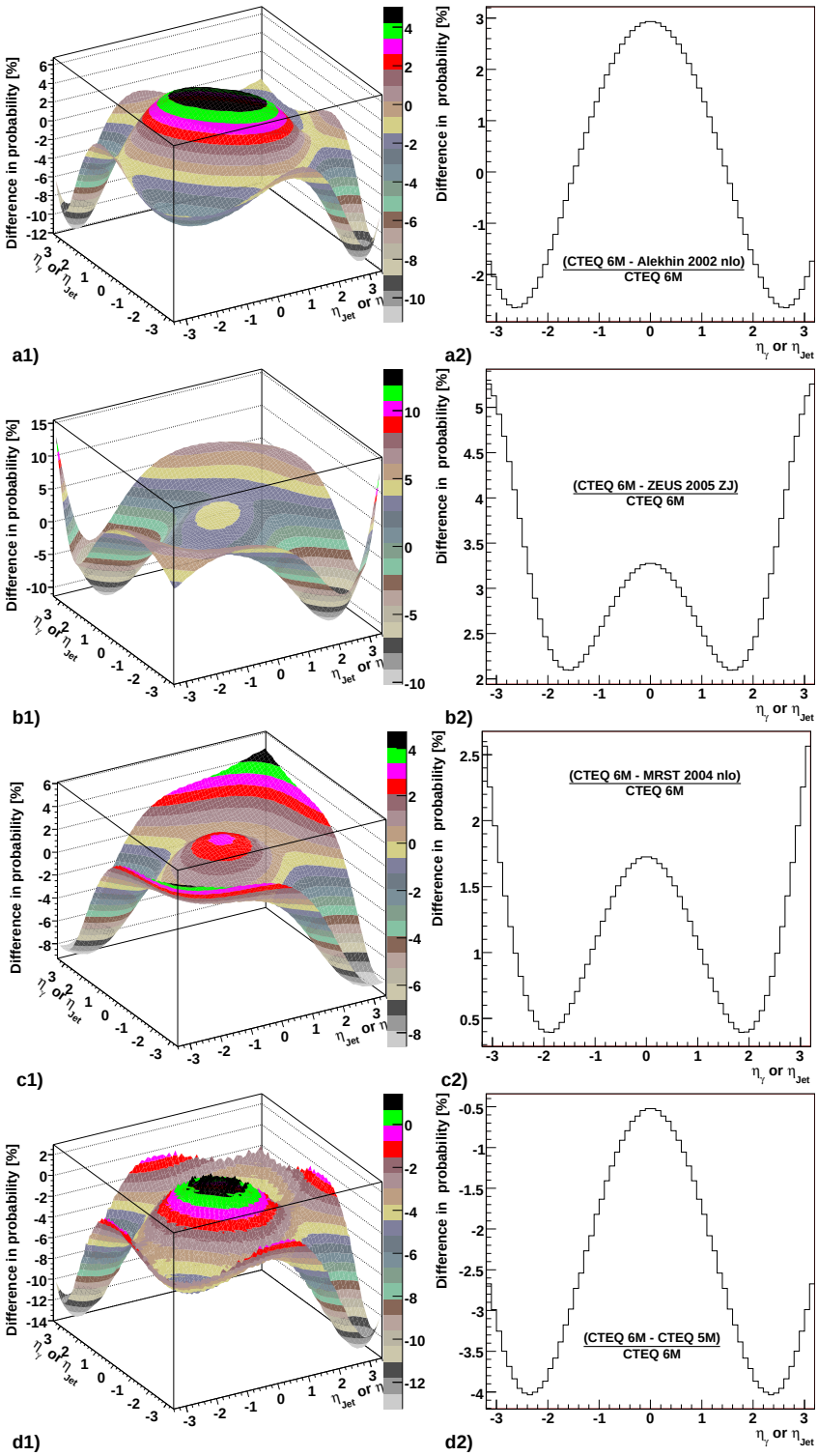

Figure 7.3: Differences in the probability map of η distributions from various PDF sets at Q=100 GeV. On the left are differences in the relative probability of obtaining a photon and jet at given values of η. Probabilities are based on scattering kinematics only; no account has been made of matrix element corrections or initial / final state radiation. On the right hand side differences in the η distribution from observing just one outgoing 'particle'.

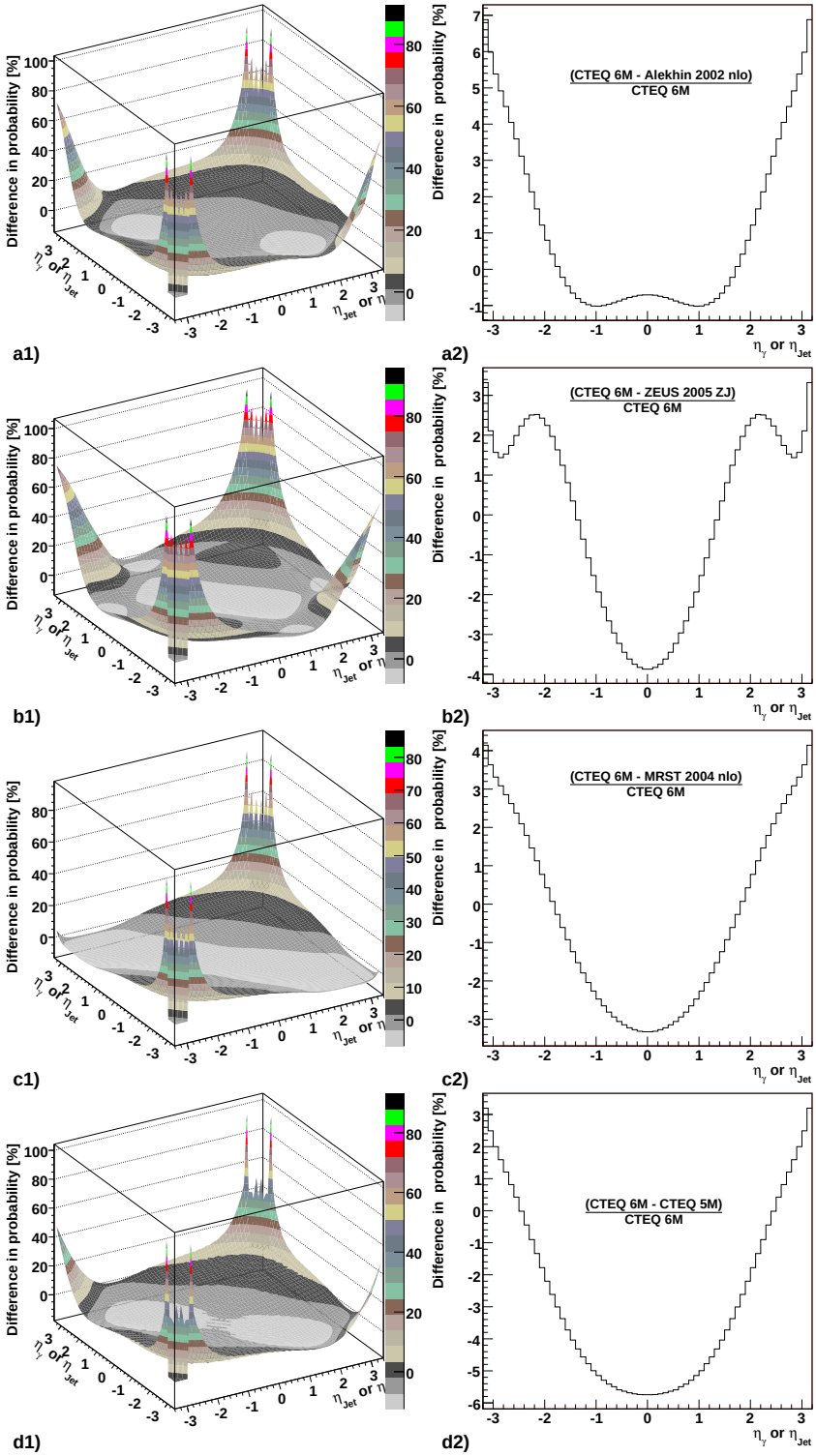

Figure 7.4: Differences in the probability map of η distributions from various PDF sets at Q=300 GeV. On the left are differences in the relative probability of obtaining a photon and jet at given values of η. Probabilities are based on scattering kinematics only; no account has been made of matrix element corrections or initial / final state radiation. On the right hand side differences in the η distribution from observing just one outgoing 'particle'.

at 110 GeV and variations of $\approx 10\%$ are seen between sets. At $p_T > 300$ GeV all events should be visible to the detector and as the increased differences between PDF sets continue, variations across η of $10 - 15\%$ are typically of the PDF sets investigated. The cause of these effects and their interpretation are considered in section 7.5. In conclusion, the differences seen in section 7.3 appear to be present in the Pythia Monte Carlo.

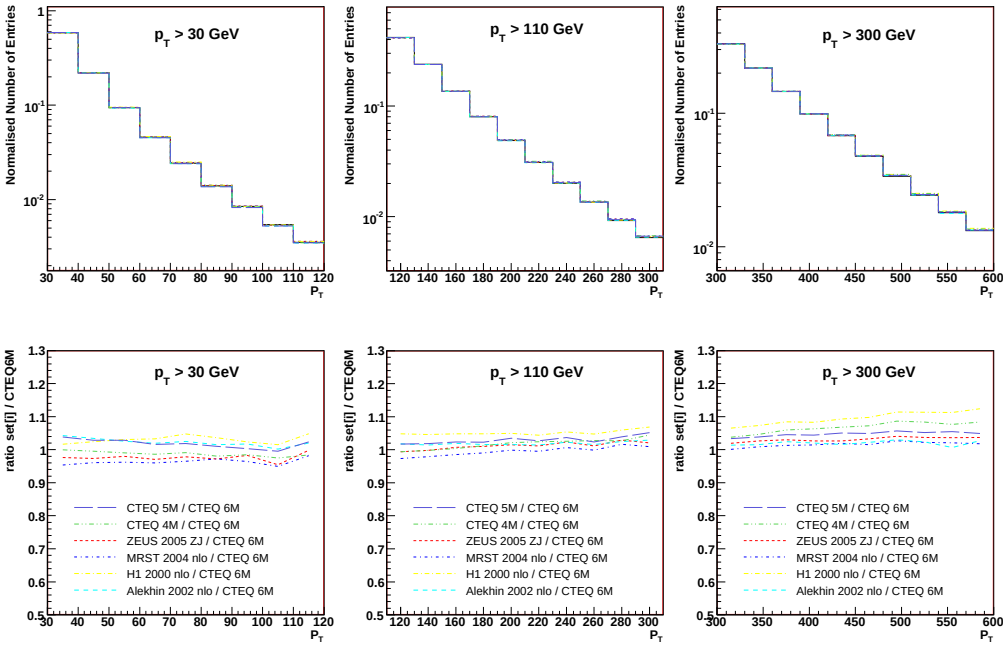

Figure 7.5: p_T distributions for direct photons with $p_T > 30$, 110 and 300 GeV generated with Pythia. On top are distributions for a variety of PDF sets and at the bottom are those sets relative to CTEQ 6M.

7.5 Probing the Structure of the Proton

An attempt is made to understand the cause of the variations seen in sections 7.3 and 7.4. Differences in the PDF predictions of figure 7.6 have their origins in either the gluon or quark PDF, these being the only quantities varied between the distributions. An investigation into the properties of the interacting partons is performed

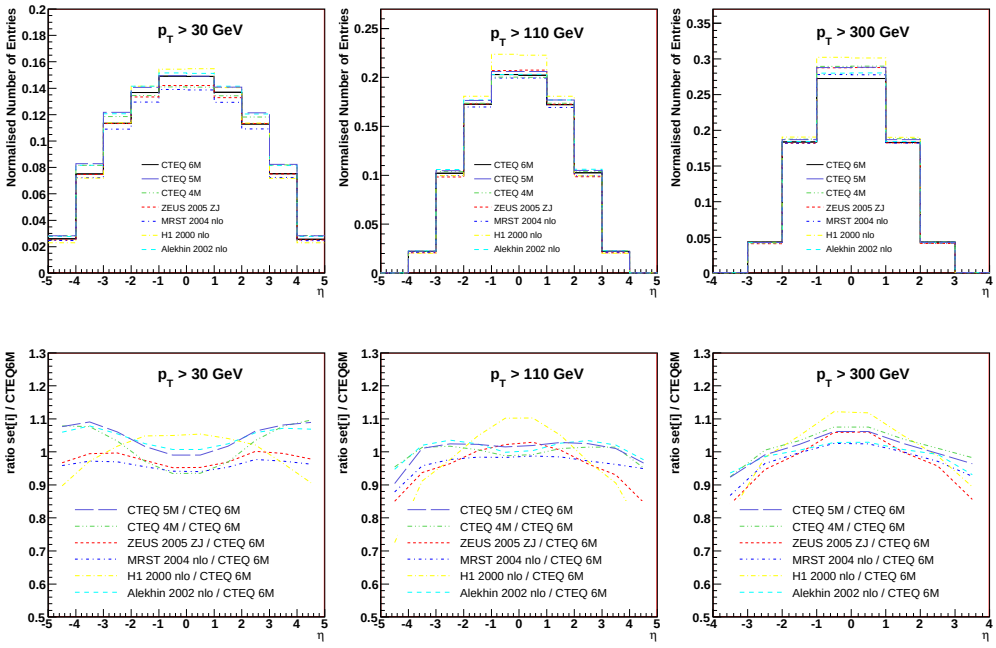

Figure 7.6: η distributions for direct photons with $p_T > 30$, 110 and 300 GeV generated with Pythia. On top are distributions for a variety of PDF sets and at the bottom are those sets relative to CTEQ 6M.

with Pythia and this is then used to interpret results obtained using the CTEQ 6M error sets.

7.5.1 Parton Momentum Fractions Probed

Quark-gluon scattering was simulated in the standalone Pythia Monte Carlo 6.228. Tree level four vectors were written out in the ASCII format along with the *type* and x value of the interacting partons. Around 10^4 events were generated for each p_T range investigated. Figure 7.7 shows distributions for $p_T > 50$ GeV and illustrates the connection between the x involved in the hard scatter and η_γ observed in the detector. Figure 7.7 (a) shows the x value of the two interacting partons for each value of η_γ. A profile of this scatter plot is shown in figure 7.7 (b) detailing how these values are distributed over the four orders of magnitude considered. Finally (c) shows the η distribution of the direct photon and via the shaded regions connects this to the partonic x. Since to create each direct photon two partons are involved, this distribution has two entries for each η_γ.

At high η, events show the high-x - low-x structure of the interacting partons, forming the cross shaped scatter plot shown in figure 7.7 (a). As expected at $\eta \approx 0$ events contain two partons of roughly equal momentum, each of $x \approx 10^{-2}$. From figure 7.7 (a) and (c) it can be seen that the majority of events in the central part of the detector ($|\eta| < 1.0$) originate from partons with $10^{-3} - 10^{-1}$. Partons with x very large ($> 10^{-1}$) or very small ($< 10^{-3}$) produce photons predominately in the region $\eta > 2.0$ and at the extreme value of η ($\eta = 3.2$) the minimum value of x probed can be seen to be consistent with equation 4.7, restated below. Using $\eta = 3.2$ and $x_T = 2p_T/\sqrt{s} = 7.14 \times 10^{-3}$ this predicts $x_{min} = 1.60 \times 10^{-4}$, which is indeed the minimum of figure 7.7 (a).

$$x_{min} = \frac{x_T e^{-\eta}}{2 - x_T e^{\eta}}$$

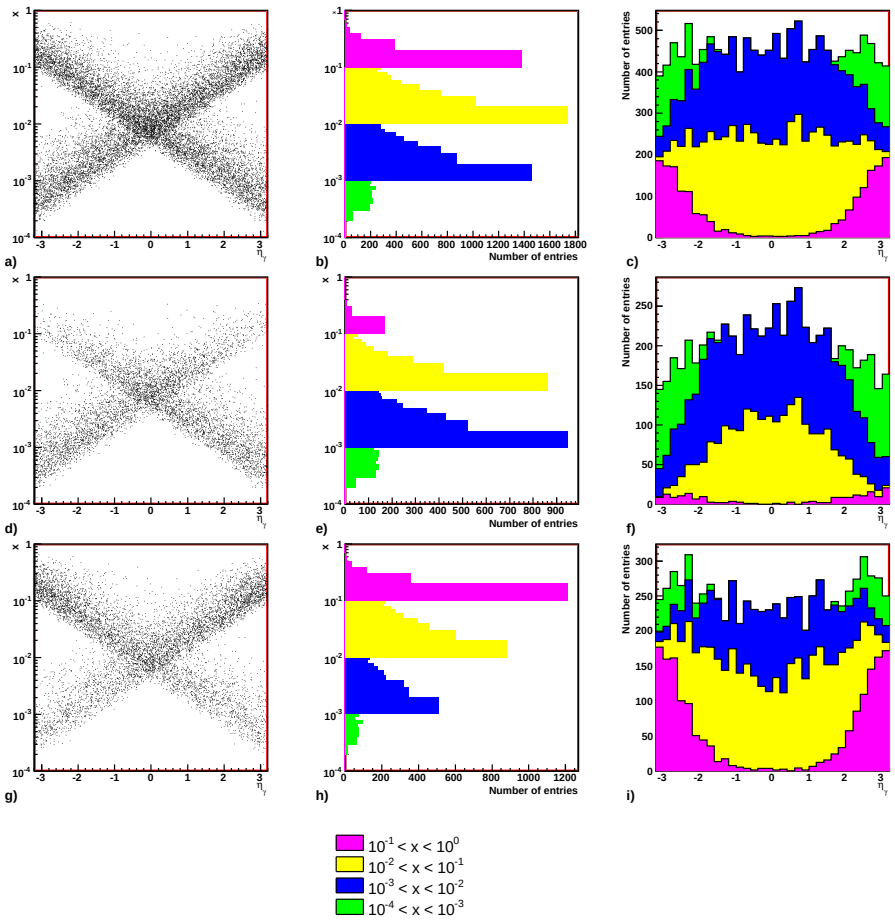

Figure 7.7: Correlations between the momentum fractions x of the initial partons and η_γ for $p_T > 50$ GeV. Plots (a)-(c) are for all interacting partons, (d)-(f) for gluons and (g)-(i) for quarks. See text for further details.

The plots of figure 7.7 (a)-(c) show the x values of both the interacting gluon and quark. These plots are repeated for each of these two types; figures 7.7 (d)-(e) for gluons, figures 7.7 (g)-(i) for quarks. Immediately the effects of the different contributions can be seen. The gluon has a typical x value smaller than that of the quark and is a direct result of the relative sizes of their PDFs. As can be seen from figure 7.8 for all values of $x \lesssim 10^{-1}$ the gluon dominates and is therefore the most likely source for this low x parton; for $p_T > 50$ GeV the gluon is the lowest x parton in $\approx 68\%$ of interactions. Since the low-x gluon will similarly dominate for all values of Q, the pattern of high-x quark and low-x gluon will continue into the high p_T region. Furthermore, as the energy of the scatter is increased, the average high-x

and average low-x values also increase. As x increases so too does the quark PDF relative to the gluon. Hence, for these high p_T scatters the proportion of high-x quark - low-x gluon events correspondingly increases: $\approx 73\%$ at 100 GeV, $\approx 78\%$ at 300 GeV and $\approx 80\%$ at 600 GeV. However, despite this, it still leaves a significant number of events that probe the high-x gluon in the region $x \gtrsim 10^{-1}$.

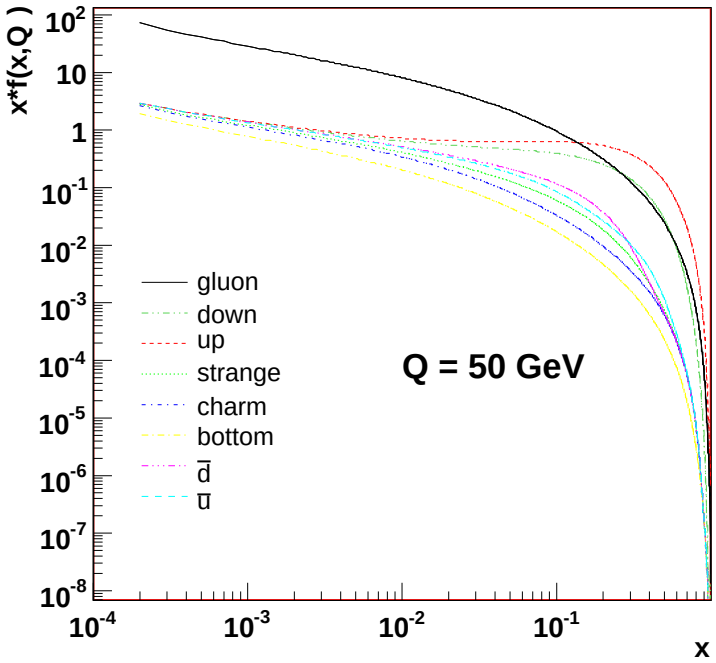

Figure 7.8: Parton Density Functions for CTEQ 6l.

Figure 7.9 repeats the plots of figures 7.7 (d)-(f) for the ranges $p_T > 100,\ 300$ and 600 GeV. They show how the x value of the gluon evolves with increasing p_T, until at 600 GeV about 1/3 of events involve a gluon with $x > 10^{-1}$. These events are obtained from either the minority of scatters that consist of a low-x quark and high-x gluon, or from those scatters that are centrally produced with $p_T > 700$ GeV such that both partons are in the region $x > 10^{-1}$. It should also be noted that, as the energy region is increased, initial state radiation (ISR) has an increased effect. At 600 GeV $\approx 50\%$ of the gluons taking part in Pythia's Compton scattering process have their origin in ISR and not in the gluon PDF. These gluons are excluded from all plots since they are unrelated to the gluon found in the proton.

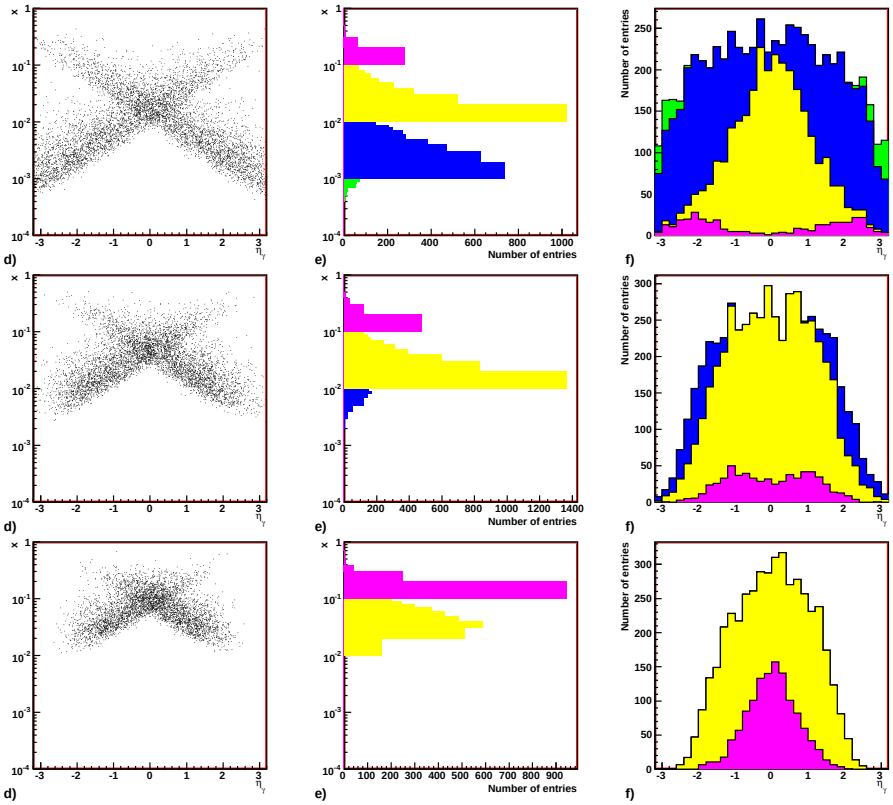

Figure 7.9: Correlations between the momentum fractions x of the initial partons and η_γ. The top line of plots are for $p_T > 100$ GeV, the middle plots $p_T > 300$ GeV and the bottom plots $p_T > 600$ GeV. See text for further details.

From this analysis, it can be concluded that the majority of direct photons produced will originate from a high-x quark and a low-x gluon. This proportion increases with p_T, as does the number of events involving gluons with $x \gtrsim 10^{-1}$. These events should then be sensitive to the different parametrisations of the gluon which is relatively unconstrained at high-x. Events involving a low p_T photon will likewise be sensitive to the low-x gluon and may help to constrain this function in the region $10^{-4} < x < 10^{-3}$.

7.5.2 CTEQ6 Error Sets

The CTEQ6 PDF is the latest set produced by the CTEQ group and contains a number of fits, together with a systematic assessment of the associated errors [6,85]. This is important, since many of the global PDF fits produced by various groups, make similar assumptions and use similar data sets. As a result the traditional method of estimating uncertainty, by comparing the various different published parametrisations, could give unreliable estimates. Central values for the CTEQ error sets are obtained in the familiar way; a hypothesised PDF form is fitted to a variety of experimental data sets and a global χ^2 function is minimised providing a central value for each PDF. The CTEQ group then goes on to identify 20 free parameters that describe the behaviour of the global χ^2 in the neighbourhood of this minimum. Then, by allowing these to vary to their minimal and maximal values, they form 40 eigenvector error sets parameterising the uncertainty of the central value.

The full uncertainty associated with the fit of CTEQ6 is calculated according to

$$\Delta X = \frac{1}{2}\left(\sum_{i=1}^{N_p} [X(S_i^+) - X(S_i^-)]^2 \right)^{1/2} \tag{7.3}$$

where X is the observable, $X(S_i^{\pm})$ are the predictions based on the error sets $S_i^{\pm}$ and N_p is the number of pairs of such sets, 20 in this case [6]. The observed X can

be anything that can be predicted from $S_i^{\pm}$ and includes the PDFs themselves. ΔX scales linearly with the tolerance (T) used in the global χ^2 fit [85]. The CTEQ group have carried out an estimate on the value of T needed to justify their fundamental assumption that the data sets used in their global fit are individually acceptable and mutually compatible. They estimate that $T \approx 10 - 15$ [85], with a value of 10 being used in the calculation of equation 7.3 above [6].

Importantly, these error sets, associated with the central fit, have some physical interpretation and can be related to the parameters used to describe the shape of the PDF. Eigenvector 15 and the associated sets 29 and 30 translate primarily into the uncertainty of the gluon, specifically one of the parameters used to parametrise the gluon PDF, A_2. This is not the complete uncertainty, since this can only be calculated with reference to the full 40 sets, nevertheless, it enables the effect of part of the gluon uncertainty to be shown in η distributions.

The total uncertainty, ΔX, is applied to CTEQ 6M and used to calculate the maximum and minimum gluon contribution of CTEQ 6M, (CTEQ 6M $\pm\Delta X$). Figure 7.10 shows this expressed as a ratio to the central value, forming upper and lower bands. The bands themselves do not represent allowed PDFs, since to ensure the total contribution remains constant, if the gluon is high at one value of x it must be low at another value. Sets 29 and 30 are shown as dashed and dotted lines in figure 7.10 and form an example of two of the allowed PDFs. These two sets are used in figure 7.11 and show the effect on the probability map (discussed in section 7.3.1) of the change in the gluon PDF. This is around 4% at 20 GeV, increasing to $\approx 7\%$ at 100 GeV and $\approx 10\%$ at 300 GeV. However, since the total uncertainty on the gluon is larger than that given in these two sets, the actual difference is likely to be greater.

Figure 7.12 shows the direct photon η distribution as generated in Pythia 6.323 using the error sets 29 and 30. Four different p_T ranges are considered, $p_T >$ 20, 50, 300 and 600 GeV, with no corrections being made for detector effects or for

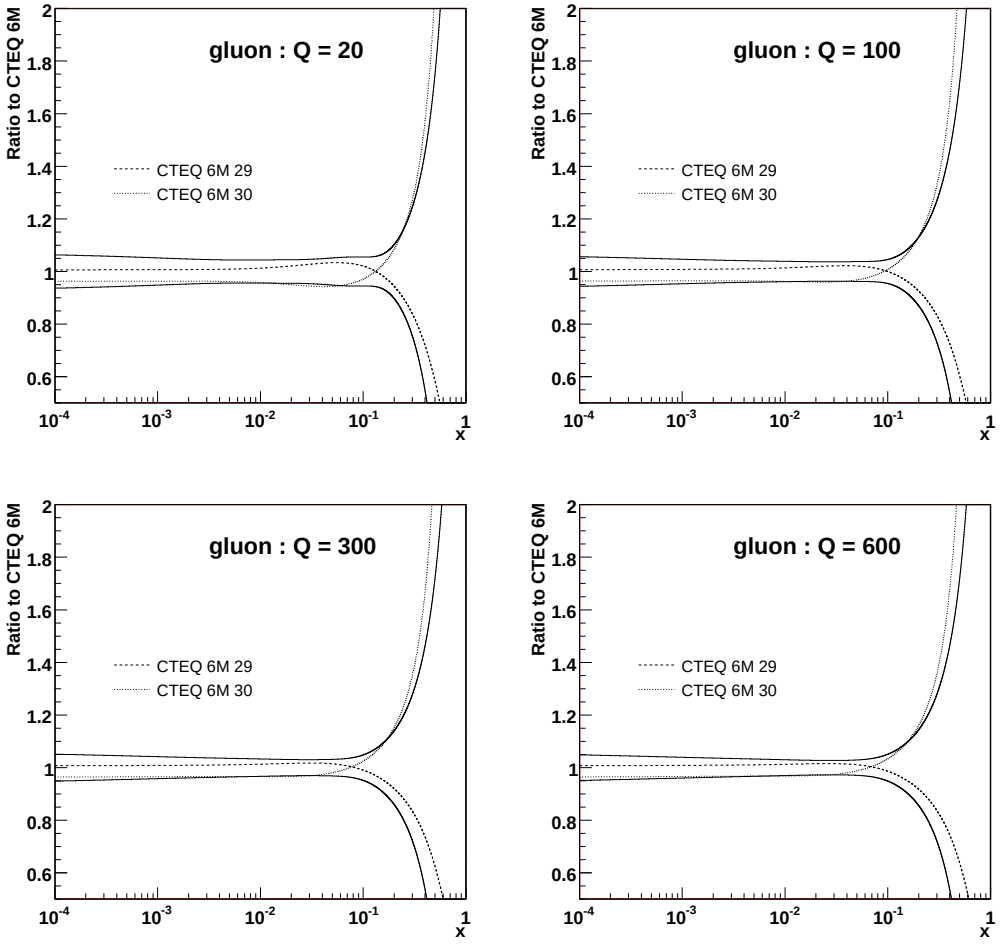

Figure 7.10: Uncertainty present in the CTEQ 6M PDF fits. The solid lines are the maximum and minimum variation for the gluon content of the proton, as calculated from equation 7.3. The dashed and dotted lines represent two possible PDF fits, CTEQ 6M error sets 29 and 30.

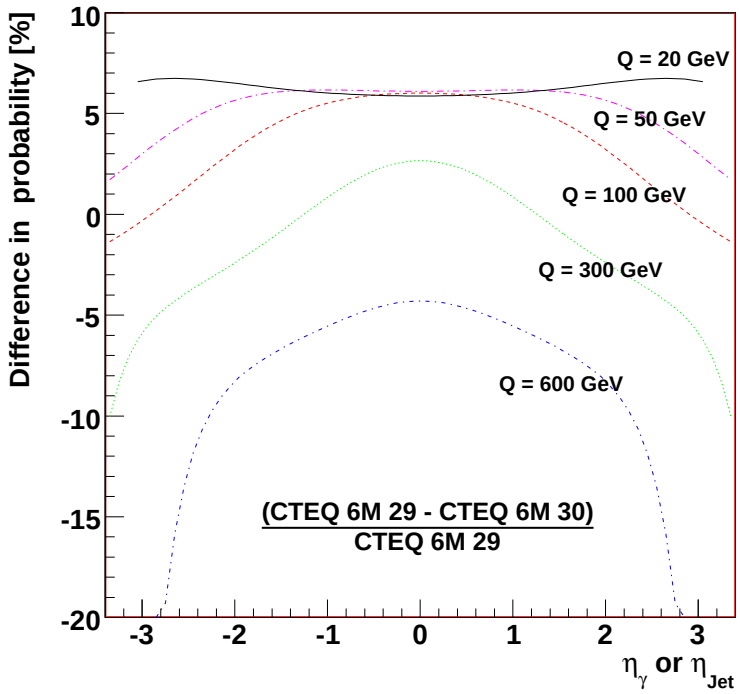

Figure 7.11: Differences in the probability map of η distributions for CTEQ 6M 29 and 30.

inefficiencies. In all cases the ratio of the two sets are given below the corresponding η distribution. The range of this ratio is restricted to the region where the photons can be observed $|\eta| < 3.2$. A small variation between the two sets is seen at $p_T > 20$ GeV and is consistent with the expectation based on figure 7.11. As the p_T range of the photon is increased, the difference between the two sets becomes more visible and increases from about 5% at 50 GeV to 7% at 300 GeV and 10% at 600 GeV. A total of one million events for each PDF were used in figure 7.12, with the exception of $p_T > 600$ GeV which used 0.4 m events. Whilst event rates for the lower p_T ranges should be obtainable, at 600 GeV it represents 1 ab^{-1} of data and would take the LHC 10 years at design luminosity to accumulate. It is included here for illustrative purposes to show the maximum variation that could be achieved.

It is clear from figures 7.11 and 7.12, that as energy increases, the differences shown by CTEQ 6M 29 and 30 become larger. This sensitivity could be caused by differences in either the gluon, or quark PDF, since one of each type is used

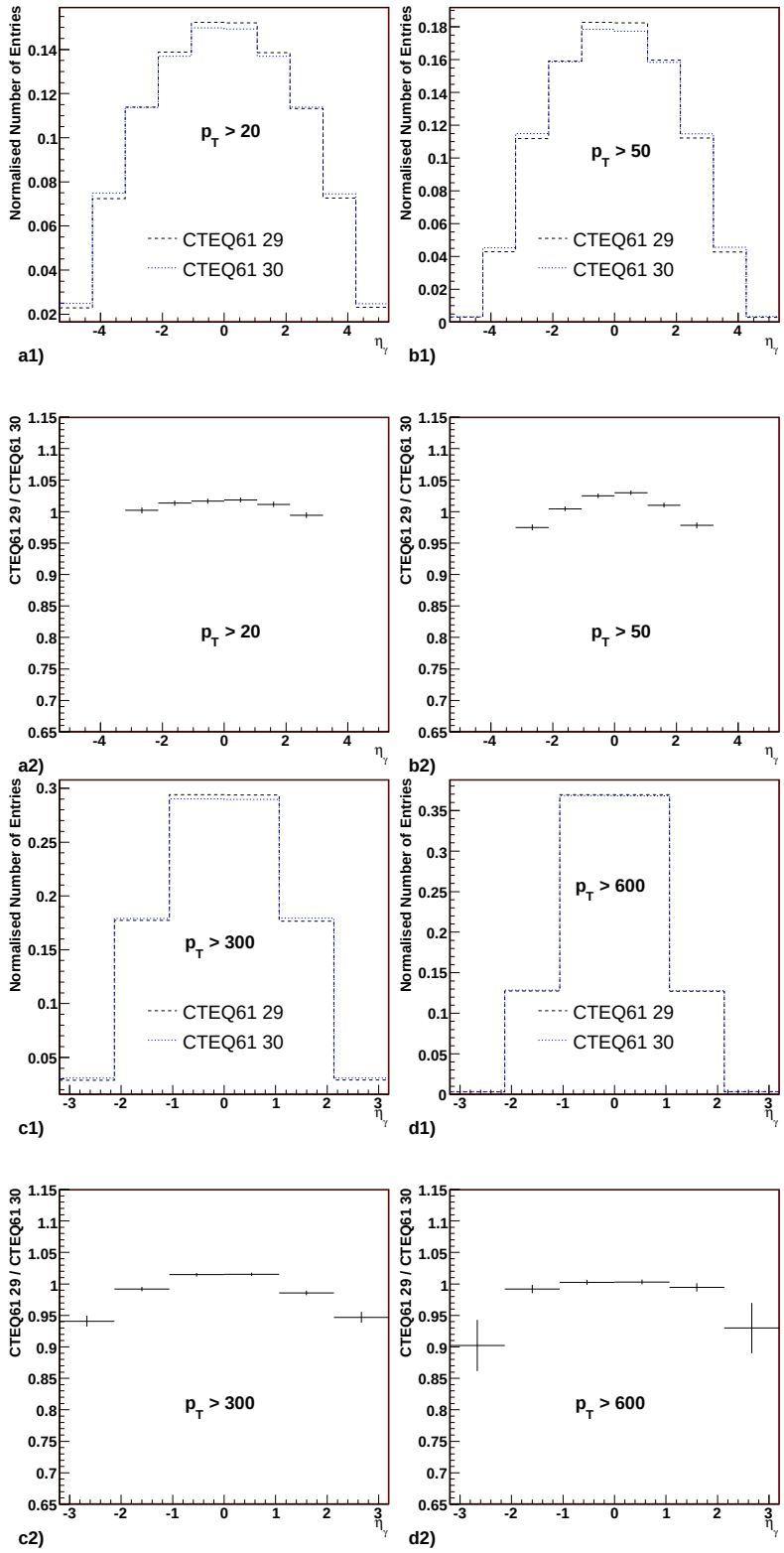

Figure 7.12: Direct photon distributions as generated by Pythia using CTEQ 6l sets 29 and 30. η_γ is shown for both PDFs, together with the ratio CTEQ 29 / CTEQ 30.

in the scatter. Although the sets 29 and 30 have a large uncertainty in the gluon, differences are also present in the distributions of other partons. Figure 7.13 shows the associated error bands of CTEQ 6M for the gluon and up quark, the most probable partons in direct photon events. As in figure 7.10, sets 29 and 30 used to obtain the distributions shown in figures 7.11 and 7.12 are given in addition.

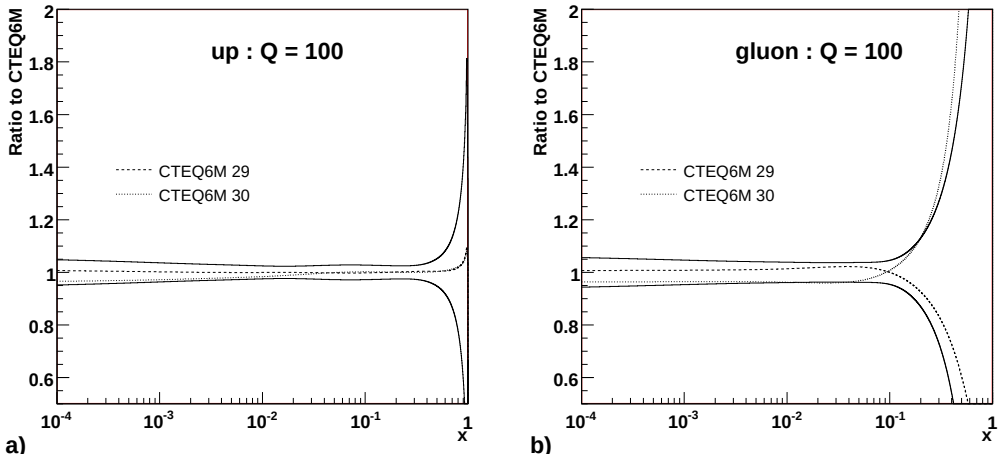

Figure 7.13: Uncertainty present in the CTEQ 6M PDF fits. The solid lines are the maximum and minimum variation for the proton, as calculated from equation 7.3. The dashed and dotted lines represent two possible PDF fits, CTEQ 6M error sets 29 and 30.

Figure 7.13 provides a valuable insight into the variation of the quark and gluon PDF in different x ranges. The uncertainty of the up quark present in set 29 and 30 can be seen to be small at high x. Figure 7.13 (a) shows these two distributions are almost identical at $Q = 100$ GeV and a similar picture is also present at other values of Q. The differences in the low-x up quark given by 29 and 30 is larger, but is still smaller than that of the high-x gluon, as shown in figure 7.13 (b).

As has been seen in section 7.5.1 when producing a direct photon the most probable x used in the interaction involves a high and low x parton, one from the quark and one from the gluon. The interaction therefore probes the high-x quark

and low-x gluon or the low-x quark and high-x gluon. By considering the associated uncertainty in these regions, shown in figure 7.13, it can be seen that in both cases it is the gluon that is least well constrained. Therefore, in both scenarios direct photons can play a role in constraining the gluon PDF. At low p_T information can be obtained on the low-x gluon and at high p_T the high-x content.

Furthermore at $p_T > 300$ GeV events involve one parton (quark or gluon) from the range $10^{-2} - 10^{-1}$ and the other from the range $10^{-1} - 10^{0}$. As p_T increases, the number of events probing the high x gluon also increases, until at $Q = 600$ GeV approximately 1/3 of events involve gluons with $x > 0.1$. Since the corresponding uncertainty in the up quark of sets 29 and 30 is small in this region, as shown in figure 7.13 (a), it can be concluded that the sensitivity shown in the η_γ distributions of figure 7.12 is primarily due to the large uncertainty present in the high x gluon. As a result events in this very high p_T range should provide a constraint on the gluon content at high x.

7.6 Areas of Further Study and Experimental Consideration

7.6.1 NLO Effects

In order to extract competitive information from direct photons, an accurate theoretical description of this process is required. Sensitivity to the different parametrisations of PDFs have been demonstrated at the LO, however, these will also need to be extended to NLO calculations that accurately describe data. These NLO calculations have been discussed in section 4.4. As stated there, there is still a degree of controversy over the agreement between theory and data, especially at low energies. Since sensitivity to the high-x gluon is mainly in the high p_T region these

contentious k_T effects should be insignificant [37]. In such a case, good agreement between NLO MC and data may be expected, and if the sensitivity to the different parametrisations are obtainable, this would allow information on the gluon to be extracted.

7.6.2 PDF Fitting

PDF fitting involves the repeated generation of Monte Carlo data using hypothesised PDF forms. These are then compared to experimental data and the PDF appropriately adjusted. Repeating this process multiple times to obtain the best fit to data can be exceptionally time consuming, since current NLO calculations can take $\sim$ days to perform. Possible methods to speed up this process have been recently published [86] and show that by splitting the cross-section into two pieces, the parton level cross section can be calculated independently of the PDF. Work is currently under way to apply this technique to inclusive jets at ATLAS [87] and could be extended to include direct photons. Such a method would have clear practical advantages, allowing for efficient repeated fits and the extraction of the gluon content of the proton.

7.6.3 Experimental Considerations

Sensitivities shown have been produced using Monte Carlo truth information but include no corrections for detector effects or efficiencies. These will need to be studied in greater detail to establish the true sensitivity of ATLAS to the different PDFs. Photon identification has been discussed in sections 5.8 and 6.3 and shows that good signal to background can be obtained for direct photons, especially at high p_T. The principal source of background is the fragmentation of a quark or gluon into a π^0. It is expected that the η dependence of this background will follow that of the dijet spectrum. It will be vital to confirm this dependence and that of

the other sources of background. This will avoid artificially including these events in η_γ and distorting the spectrum.

Since different PDF parametrisations primarily manifest themselves in η_γ, the uniformity of the detector response across η will be of particular importance. The electromagnetic end-caps cover the region $2.5 < |\eta| \leq 3.2$ and although not considered in sections 5.8 and 6.3, will play a role in determining the full η distribution. As detailed in section 2.4.2, the granularity of this sampling is much reduced, especially in the first sampling where it decreases from a maximum granularity of $\Delta\eta \times \Delta\phi = 0.003 \times 0.1$ to $\Delta\eta \times \Delta\phi = 0.1 \times 0.1$. As a result both the background contamination and the efficiency are likely to be worse than in the region $|\eta| \leq 2.5$, considered in the above sections. However, whilst the performance of the end-caps is clearly of importance, none of the sensitivities discussed above are confined solely to the region $2.5 < |\eta| \leq 3.2$. It will nevertheless be advantageous to extend detection into this high η region and a further detailed detector study will be required to confirm this feasibility.

Key to any competitive measurement will be a large data sample with which to make comparisons with theory. The advantage of the η distribution is its sensitivity across the range of η and hence its relative stability to luminosity uncertainties. As shown in table 6.1, numerous low p_T events will be produced in the LHC. For these events to be usable they will be required to pass a series of trigger selection criteria and will almost certainly result in a significant loss below ≈ 60 GeV. In particular prescaled triggers are expected to be used in this region, to avoid saturating the limited bandwidth of the read out system. Above this ≈ 60 GeV threshold the single photon trigger should ensure that the majority of events seen by the detector are recorded. Trigger settings are expected to vary as running conditions evolve and this will particularly impact on the number of low p_T events obtained. Despite these factors, systematics are likely to be the biggest sources of experimental uncertainty and understanding these will be vital to extract competitive information. Since

variations in η_γ are around $5-10\%$, this sets the limit of the bin to bin systematics needed to extract information on the gluon. Such a degree of accuracy will take a substantial effort over a period of time to achieve, but subject to the considerations above, should allow information on both the high-x and low-x gluon to be obtained.

7.7 Conclusion

Scattering kinematics of direct photons have been investigated and shown to be sensitive to the various parametrisations of PDFs. These differences are propagated into the LO Monte Carlo Pythia, which shows variations of $4\% - 10\%$ in η_γ across the p_T and η ranges accessible by ATLAS. The majority of direct photons produced originate from high-x quarks and low-x gluons. However, at high p_T, significant numbers of events are expected to contain gluons in the $x \gtrsim 10^{-1}$ range. An analysis of the CTEQ 6M error sets show that the least well constrained PDF involved in direct photon production is the gluon. As a result, sensitivities shown at low p_T, will yield information on the low-x behaviour of the gluon and those obtained at high p_T, will provide valuable information on the high-x behaviour.

A brief overview of some experimental issues has also been presented. These include the need to confirm sensitivity to the gluon PDF exists for NLO direct photons and that these Monte Carlos accurately describe the LHC data. Understanding systematic effects in the ATLAS detector will provide the bulk of the challenge in obtaining competitive information on the gluon. The degree to which these events will be able to further constrain the gluon PDF will depend on the precise PDF fitting procedure used, the other experimental data sets fed into the fit and on the statistical and systematic uncertainties of the above. Further work in this area is currently needed. However, should all these factors be addressed, direct photons should provide useful information to further constrain the gluon PDF.

Bibliography

[1] R. Feynman, Phys. Rev. Lett **23**, 1415 (1969)

[2] R. K. Ellis *et. al.*, Phys. Lett. **B 78**, 281 (1978)

[3] J. F. Owens, Rev. Mod. Phys. **59**, 465 (1987)

[4] D. J. Gross and F. Wilczek, Phys. Rev. Lett **30**, 1343 (1973)

[5] Y. L. Dokshitzer, Sov. Phys. JETP **46**, 641 (1977); Zh. Eksp. Teor. Fiz. **73**, 1216 (1977)
V. N. Gribov and L. N. Lipatov, Yad. Fiz. **15**, 1218 (1972); Sov. J. Nucl. Phys. **15**, 438 and 675 (1972)
G. Altarelli and G. Parisi, **B 126**, 298 (1977)
G. Curci, W. Furmanski and R. Petronzio, Nucl. Phys. **B 175**, 27 (1980)
W. Furmanski and R. Petronzio, Phys. Lett. **B 97**, 437 (1980)

[6] J. Pumplin *et. al.*, JHEP **0207**, 012 (2002)

[7] A. C. Benvenuti *et. al.*, Phys. Lett. **B 223**, 485 (1989)

[8] A. C. Benvenuti *et. al.*, Phys. Lett. **B 237**, 592 (1990)

[9] C. Adloff *et. al.*, Eur. Phys.J. **C 13**, 609-639 (2000)

[10] C. Adloff *et. al.*, Eur. Phys. J. **C 21**, 33-61 (2001)

[11] S. Chekanov *et. al.*, Eur. Phys. J. **C 21**, 443-471 (2001)

[12] M. Arneodo *et. al.*, Nucl. Phys. **B 487**, 3-26 (1997)

[13] U. K. Yang *et. al.*, Phys. Rev. Lett. **86**, 27422745 (2001)

[14] G. Moreno *et. al.*, Phys. Rev. **D 43**, 28152835 (1991)

[15] R.S. Towell *et. al.*, Phys. Rev. **D 64**, 052002 (2001)

[16] T. Affolder *et. al.*, Phys. Rev. **D 64**, 032001 (2001)

[17] B. Abbott *et. al.*, Phys. Rev. Lett. **86**, 1707-1712 (2001)

[18] B. Abbott *et. al.*, Phys. Rev. **D 64**, 032003 (2001)

[19] F. Abe *et. al.*, Phys. Rev. Lett. **81**, 5754 (1998)

[20] M. Kobayashi and T. Maskawa, *CP - Violation in the Renormalizable Theory of Weak Intectation*, Prog. Theor. Phys. 49, pp 652-657, Frebuary 1973

[21] *Atlas Detector and Physics Perfermance Technical Design Report*, CERN/LHCC/99-14, ATLAS TDR 14, May 1999

[22] *Atlas Inner Detector Technical Design Report*, CERN/LHCC/97-16, ATLAS TDR 4, April 1997

[23] *Liquid Argon Calorimeter Technical Design Report*, CERN/LHCC/96-41, Dec 1996

[24] M. Dobbs and J. B. Hansen, ATL-SOFT-2000-001 (2001)

[25] S. Agostinelli *et. al.*, Nucl. Instrum. Methods Phys. Res. **A 506**, 250 (2003)

[26] J. Alison *et. al.*, IEEE Transactions on Nuclear Science **53**, 270 (2006)

[27] E. Richter-Was, D. Froidevaux, and L. Poggioli, ATLAS Internal Communication ATL-PHYS-98-131 (1998)

[28] P. Allport *et. al.*, Nucl. Instr. and Meth. **A 435**, 74-79 (1999)

[29] D. Robinson *et. al.*, Nucl. Instr. and Meth. **A 485**, 84-88 (2002)

[30] *Review of Particle Physics*, Eur. Phys. J. **C3**, 144 (1988)

[31] T. Kondo *et. al.*, Nucl. Instr. and Meth. **A 466**, 390 (2001)

[32] *ABCD3T ASIC Project Specification*, V1.2, chipinfo.web.cern.ch/chipinfo /docs/ABCD3T_Spec_v1_1.pdf

[33] W. Dabrowski *et. al.*, IEEE Trans. Nucl. Sci. **47**, 1843-1850 (2000)

[34] T. Kondo *et. al.*, Nucl. Instr. and Meth. **A 485**, 27-42 (2002)

[35] *Electrical Tests of SCT Hybrids and Modules*, http://hepwww.rl.ac.uk/atlas-sct/documents/Electrical_Tests.htm

[36] A. Kumar *et. al.*, Physical Review **D 67**, 014016 (2003)

[37] J. Huston, ATL-PHYS-99-008

[38] P. Aurenche *et. al.*, Phys. Rev. **D 73**, 094007 (2006)

[39] http://wwwlapp.in2p3.fr/lapth/PHOX_FAMILY/main.html

[40] J. P. Guillet, Private Communication

[41] L. Bourhis *et. al*, Eur. Phys. J. **C 2**, 529-537 (1998)

[42] E. Poulsen *Diploma Thesis* Institute for Theoretical Physics, University of Zurich, (2006)

[43] E. W. N. Glover and A.G. Morgan, Z Phys. **C 62**, 311 (1994)

[44] P. Aurenche *et. al.*, Phys. Rev. **D 42**, 1440 (1990)

[45] P. Aurenche *et. al.*, Nucl. Phys **B 399**, 34 (1993)

[46] Catani *et. al.*, J. High Energy Phys. **05**, 028 (2002)

[47] A. D. Martin *et al.*, Eur. Phys. J. **C4**, 463 (1998)

[48] H. L. Lai *et. al.*, Phys. Rev. **D 55**, 1280 (1997)

[49] U. Baur *et. al.*, HEP-PH 0005226 (2000)

[50] L. Apanasevich *et. al.*, Phys. Rev **D59**, 074007 (1999)

[51] J. Huston *et. al.*, Phys. Rev. **D 51**, 6139 (1995)

[52] P. Aurenche *et. al.*, Eur. Phys. J. **C9**, 107 (1999)

[53] L. Apanasevich *et. al.*, Phys. Rev. **D 59**, 074007 (1999)

[54] E. Annassontzis *et. al.*, Z. Phys. **C 13**, 277 (1982)

[55] M. Bonesini *et. al.*, Z. Phys. **C 38**, 371 (1988)

[56] C. Albajar *et. al.*, Phys. Lett. **B 209**, 385 (1988)

[57] A. L. S. Angelis *et. al.*, Nuc. Phys. **B 327**, 541 (1989)

[58] E. Annassontzis *et. al.*, Sov. J. Phys. **51**, 5 (1990)

[59] J. Alliti *et. al.*, Phys. Lett. **B 263**, 544 (1991)

[60] G. Ballocchi *et. al.*, Phys. Lett. **B 436**, 222 (1998)

[61] L. Apanasevich *et. al.*, Phys. Rev. Lett. **81**, 2642 (1998)

[62] B. Abbott *et. al.*, Phys. Rev. Lett. **84**, 2786 (2000)

[63] V. M. Abazov *et. al.*, Phys. Lett. **B 639**, 151 (2006)

[64] V. M. Abazov *et. al.*, Phys. Rev. Lett. **87**, 251805 (2001)

[65] D. Acosta *et. al.*, Phys. Rev. **D 70**, 074008 (2004)

[66] D. Acosta *et. al.*, Phys. Rev. **D 65**, 112003 (2002)

[67] C. R. Hall, PhD Thesis (2002)

[68] https://twiki.cern.ch/twiki/bin/view/Atlas/WorkBook

[69] https://twiki.cern.ch/twiki/bin/view/Atlas/AtlasGeomDBTags

[70] T. Sjstrand, P. Edn, C. Friberg, L. Lnnblad, G. Miu, S. Mrenna and E. Norrbin, Computer Phys. Commun. **135**, 238 (2001)

[71] https://twiki.cern.ch/twiki/bin/view/Atlas/LJSF

[72] *ATLAS First-Level Trigger Technical Design Report*, CERN-LHCC-98-14

[73] *ATLAS High-Level Trigger Data Acquisition and Controls Technical Design Report*, CERN-LHCC-2003-022

[74] M. Wielers, ATL-PHYS-99-016 (1999)

[75] M. Wielers, ATL-PHYS-2002-004 (2002)

[76] M. Escalier *et. al.*, ATL-PHYS-PUB-2005-018 (2005)

[77] F. Derue and C. Serfon, ATL-COM-PHYS-2004-074 (2004)

[78] S. Simon, ATL-COM-SOFT-99-001 (1999)

[79] B. A. Kniehl *et. al.*, Nuclear Physics **B 582**, 514 (2000)

[80] H. Baer, J. Ohnemus, and J.F. Owens, Phys. Lett. **B 234**, 127 (1990)

[81] *ATLAS Calorimeter Performance*, CERN/LHCC/96-40, Dec 1996

[82] *Review of Particle Physics*, Physical Review **D66**, 010001 (2002)

[83] J. Huston *et. al.*, Phys. Rev. **D 58**, 114034 (1998)

[84] *Les Houches Accord PDF (LHAPDF)* http://hepforge.cedar.ac.uk/lhapdf/

[85] J. Pumplin *et. al.*, Phys. Rev. **D 65**, 014013 (2001)

[86] T. Carli, HEP-PH 0510324 (2005)

[87] D. Clements, http://indico.cern.ch/materialDisplay.py?contribId=s2t5&sessionId=s2&materialId=0&confId=a06707